Kinetic-Hydrodynamic Modelling of Short-Pulse Doppler-Shift Spectroscopy Experiments, and Resistive Filamentation of Fast-Electron Transport

David Rhys Blackman BSc PGCE MSc

Doctor of Philosophy

University of York

Physics

September 2017

Abstract

Three pump-3ω-probe Doppler-shift spectroscopy experiments are presented along with both 1D radiation-hydrodynamics modelling (HYADES) and 1D three-stage modelling process involving: HYADES radiation-hydrodynamics pre-pulse calculations; EPOCH kinetic particle-in-cell main-pulse calculation initialised from HYADES result; followed by hydrodynamic calculations, initialised from EPOCH result, of the evolution after the main-pulse.

These investigations are aimed at exploring the formation of shocks at the front surface of targets after interaction with an ultra-short (30 fs), ultra-intense (10^{18} Wcm^{-2}) laser pulse. To this end a 3ω-probe is delayed then reflected from a 3ω critical surface on the front surface to obtain a temporal profile of the velocity of this surface.

Two investigations use identical polished crown glass targets, but are performed with lasers systems with different contrast ratios (10^5 and 10^7). HYADES simulations match experimental results for the high contrast experiments except at early times. HYADES simulations of low contrast experiments do not agree. The three-step modelling process shows good agreement with experimental results in both cases, though with some adjustment to the pre-plasma scale-length for the low contrast case.

The third Doppler-spectroscopy experiment uses a low density (over-dense) foam target with identical setup to high-contrast case described. Experimental results show a similar magnitude Doppler-shift evolution as in low-contrast case. HYADES simulations show similarities to experimental results but not overall trend. The three-step modelling process shows that the experimental response may be due to post-soliton formation as a result of SRS or photon acceleration plasma instabilities. This is supported by an additional 2D EPOCH simulation.

A fourth theoretical investigation is presented into the transport of fast electrons produced 10^{19-20} Wcm^{-2} laser pulses using the hybrid code ZEPHYROS. A low resistivity (< 5 $\mu\omega$m) at low temperatures (1 eV) is found to be of critical importance to suppressing filamentation of electron beams through low-Z targets.

Contents

List of Figures

Acknowledgements

The working environment and training provided at the York Plasma Institute has been incredible, notable thanks go to Dr Chris Ridgers for streams of ideas and help, Dr Kate Lancaster and Dr Chris Murphy for advice and help. Most importantly Dr John Pasley for being a patient mentor throughout and providing me with a host of opportunities for me to grow.

The team at the Ultra-Short Pulse High-Intensity Laser Laboratory in the Tata Institute for Fundamental Research have been both incredibly welcoming and I feel very privileged to have worked with such a productive and professional team. Particular thanks go to Dr Amit D. Lad, Dr Amitava Adak, and to the ever gracious Prof. G. Ravindra Kumar, without whose invitation the majority of the work done in this thesis could not have happened.

Dr Raoul Trines and Dr Alex Robinson and the rest of the large team at the Central Laser Facility of the Rutherford Appleton Laboratory have provided both excellent training, experience, and advice as well as providing a brilliant and extremely patient mentor in Dr Alex Robinson.

Thanks also go to: The Engineering and Physical Science Research Council's grant EP/K504178/1 has me over the last few year; The Seedcorn fund provided by the University of York International Relations Department provided the funding for visits to Mumbai; The use of computing resources provided by Science and Technology Facilities Council's e-Science facility. Thanks also go to Mrs Donna Cook, and all of the YPI Admin team, for helping me out so frequently with everything else.

Declaration

I declare that the work presented in this thesis is based on my own research and has not previously been submitted for a degree at this or at this, or any other, university. The work was supervised by Dr John Pasley (Univ. of York) and partly by Dr Alex Robinson (RAL). The experimental work presented in chapters 4, 5 & 6 was carried out by the research group headed by Prof. G. Ravindra Kumar at the Department of Nuclear and Atomic Physics at the Tata Institute for Fundamental Research in Mumbai India.

Where an external source has been used that source has been clearly cited. The HYADES software used in chapters 4, 5 & 6 is a commercial product of Cascade Applied Sciences.[1] The EPOCH software used through chapters 4, 5 & 6 was developed at the Univ. of Warwick.[2] Both the Zephyros software and the initial version of the Lagrangian hydrodynamics simulation were developed by Dr Alex Robinson (RAL).

Work contained in chapters 4, 5 and 7 has been published in peer reviewed journals as stated in the section titled 'Journal Articles' and presented in several conferences as stated in the section titled 'Conference Proceedings'.

Journal Articles

There are several publications based on work presented in this thesis. Chapters 4 and 5 are based on analysis published in publications 1 and 2 respectively. Chapter 7 has been published as 3 and is presented here with some additions.

[1] Amitava Adak, David R. Blackman, Gourab Chatterjee, Prashant Kumar Singh, Amit D. Lad, P. Brijesh, A. P L Robinson, John Pasley, and G. Ravindra Kumar. Ultrafast dynamics of a near-solid-density layer in an intense femtosecond laser-excited plasma. *Physics of Plasmas*, 21(6):062704, jun 2014.

[2] Amitava Adak, Prashant Kumar Singh, David R. Blackman, Amit D. Lad, Gourab Chatterjee, John Pasley, A. P. L. Robinson, and G. Ravindra Kumar. Controlling femtosecond-laser-driven shock-waves in hot, dense plasma. *Physics of Plasmas*, 24(7):072702, jul 2017.

[3] David R. Blackman, A. P. L. Robinson, and John Pasley. Role of low temperature resistivity on fast electron transport in disordered aluminium and copper. *Physics of Plasmas*, 22(8):083108, aug 2015.

[4] Gourab Chatterjee, Prashant Kumar Singh, A P L Robinson, D R Blackman, N Booth, O Culfa, R J Dance, L A Gizzi, R J Gray, J S Green, P Koester, G Ravindra Kumar, L Labate, Amit D Lad, K L Lancaster, J Pasley, N C Woolsey, and P P Rajeev. Micron-scale mapping of megagauss magnetic fields using optical polarimetry to probe hot electron transport in petawatt-class laser-solid interactions. *Scientific Reports*, 7(1):8347, 2017.

Conference Proceedings

In addition to article published, work described in Chapter 4 and 5 has been presented in conference proceedings 3 and 1.

[1] Amitava Adak, David R Blackman, Gourab Chatterjee, Prashant Kumar Singh, Amit D. Lad, P. Brijesh, A. P. L. Robinson, John Pasley, and G. Ravindra Kumar. Probing ultrafast dynamics in a solid-density plasma created by an intense femtosecond laser. 688, 2016. 8th International Conference on Inertial Fusion Sciences and Applications (IFSA), Nara, JAPAN, SEP 08-13, 2013.

[2] Dario Del Sorbo, David R. Blackman, Remi Capdessus, Kristina Small, Cody Slade-Lowther, Wen Luo, Matthew J. Duff, Alexander P. L. Robinson, Paul McKenna, Zheng-Ming Sheng, John Pasley, and Christopher P. Ridgers. Ion acceleration with radiation pressure in quantum electrodynamic regimes. *Proc. SPIE 10241, Research Using Extreme Light: Entering New Frontiers with Petawatt-Class Lasers III*, 10241:10241 – 10241 – 8, May 2017.

[3] John Pasley, David Blackman, and Alex Robinson. Modelling The Hydrodynamics Induced By The Interaction Of High-Power Short-Pulse Lasers With Dense Targets. 1824, Nov 2017. 9th International Conference on Plasma Science and Applications (ICPSA), Univ Teknologi Malaysia, MALAYSIA, Nov 28-30, 2016.

Chapter 1

Introduction

The main focus of this thesis is the modelling of shock-like phenomena produced by ultra-short (30 fs) and ultra-intense (10^{18} Wcm^{-2}) laser radiation interacting with dense targets.

High-intensity short-pulse lasers, when interacting with a dense target can generate extremely violent phenomena. However the relatively limited energy of such interactions renders these events amenable to investigate in a university laboratory, even though the temperatures produced may sometimes exceed those in the core of the Sun.[3] Using mode-locked laser systems[4–6] and chirped-pulse-amplification (CPA)[7–9] pulses as short as a few tens of femtoseconds can be amplified to petawatt powers.[10–13] With pulses focused to intensities[14] of 10^{15-20} Wcm^{-2}, these laser systems can generate pressures into the GBar regime,[14,15] and temperatures in the keV range,[3,14] in volumes on the micron scale, leading to extremely large temperature and pressure gradients. The extreme conditions in this region lead to a number of interesting phenomena including: the acceleration of electrons and ions to MeV energies[16–19] forming MegaAmpere electron currents penetrating deep into the target;[20,21] Gbar strong shock-waves,[15] which can in their own right generate interesting phenomena;[22,23] and exotic plasma instabilities.[24–26]

The conditions that occur in this type interaction make them relevant to a

range of astrophysical phenomena. Jets similar to those seen emitted from stellar objects have been studied using sophisticated target designs.[27–29] The study of the large magnetic fields generated by laser plasma interactions[30] and the turbulence generated as a result of a variety of instabilities[31–33] has led to significant discoveries such as possible mechanisms for the generation of magnetic fields in the early universe.[34] The physics of radiative blast waves similar to those occuring in supernova[35,36] and collisionless shock waves[37,38] have also been studied. Hydro-dynamic instabilities generating terahertz acoustic waves arising from non-local heating[23] with links to supernova shocks,[39] have also been discovered.

In addition to astrophysical phenomena, several more terrestrial applications have been in development for some decades now. Protons and other heavier nuclei can be accelerated, via mechanisms like Target Normal Sheath Acceleration,[40–45] to energies relevant for applications such as hadron therapy using significantly smaller and less expensive devices than those which are currently employed for this purpose.[46–51] Novel imaging techniques, such as phase contrast imaging, using the extremely short duration hard x-ray[52,53] pulses generated at the rear of the target have been investigated. Coherent terahertz radiation generated from the passage of a shock through a crystal lattice[54] has been observed[22,55] with the view to possible imaging applications.[56] The transport of accelerated electrons through a solid target is also of importance to fast-ignition fusion,[57–60] as is the hydrodynamic evolution of extremely high pressure shocks.[61,62]

1.1 Modelling the Hydrodynamics of Short Pulse Laser Interactions

In this thesis a number of studies are presented on the production and evolution of shock-like phenomena in short-pulse laser-plasma interactions. The first two

experiments described in chapter 4 and 5 in part explore the issue of laser contrast in the performance of such experiments.

The process of CPA requires that a laser pulse is chirped before amplification using one or more gratings, once amplified the pulse is then temporally compressed using a similar set of gratings. A laser pulse will consist of stimulated and spontaneous emission, whilst both emission types are amplified by the CPA set up, the spontaneous emission is not chirped in the same fashion as the stimulated emission.[63] This leads to a pre-pulse leading the main amplified and temporally compressed pulse. The contrast of a laser system is defined as the ratio of the main pulse intensity to the pre-pulse intensity, typical values are in the range $10^5 - 10^8$. This pre-pulse can contain a significant fraction of the output energy of a low-contrast laser system. Lower contrast systems (with large pre-pulse intensities) can ablate a target prior to the arrival of the main pulse, significantly altering the physics of the main-pulse interaction with the target.

Modelling the longer term hydrodynamic behaviour of materials subjected to short-pulse ultra-intense lasers is challenging. There are three distinct phases, with widely varying timescales to consider: the pre-pulse interaction (around 500 ps to 1 nanosecond); the main-pulse interaction (around 100-200 fs); and the evolution of the excited plasma after the main-pulse interaction. By using a series of calculations for each phase respectively; radiation-hydrodynamics, followed by particle-in-cell, followed again by a simple hydrodynamics calculation, the hydrodynamic evolution of the plasma around the laser deposition region can be explored in the immediate aftermath of the interaction with the main pulse.

The interaction of lower intensity ($\sim 10^{12} - 10^{14}$ Wcm^{-2}) laser pulses is often modelled using radiation-hydrodynamic codes.[64] This type of simulation combines a hydrodynamic fluid model with radiative transport calculations based on atomic data.[64] These codes use a variety of methods to account for laser-plasma interactions such as: ray tracing, where the laser pulse is treated as a ray (or rays) which lose

energy according to various scalings,[63–65] e.g. inverse bremsstrahlung; Helmholtz solvers, which use the plasma dielectric to calculate the electrostatic reflectivity of each section of plasma, up until the point where the dielectric takes an imaginary value.[65]

The assumptions required for the laser absorption models to be accurate are violated in the case of extremely short ultra-intense laser pulses. With laser intensities greater than 10^{17} Wcm^{-2}, electrons can gain kinetic energy that is comparable to their rest mass, and so can be accelerated to velocities close to c.[65] Inverse bremsstrahlung absorption is highly dependent on collisions,[63,64] the collision frequency drops at high temperatures and so this mechanism ceases to be dominant at very high intensities. Helmholtz solvers also make an assumption that the plasma does not move on the same timescale as the laser pulse, which is violated in the case of relativistic electron motion.[65]

The transport of thermal energy in radiation-hydrodynamics simulations is usually calculated using a flux-limited diffusion model.[64] At high intensities large quantities of electrons can be liberated from the interaction region causing large currents to flow through the target. These currents cannot be simulated in a diffusion model.[66]

Whilst these codes are not suitable for modelling the interaction of ultra-short ultra-intense pulse, they can offer a reasonable model for the initial ablation of the target front surface due to the pre-pulse. The interaction in the main pulse clearly requires an alternative modelling framework. The framework used for modelling such interactions in this thesis is the Particle-in-cell (PIC) simulation.

PIC simulations employ a cloud of charged particles which interact with a discrete electromagnetic field, the laser pulse being emulated as an oscillation in an EM field resolved onto the grid.[67] So long as the mesh is fine enough that both the laser wavelength and, more demandingly with dense targets, the Debye length are resolved then reasonably accurate modelling of the laser-plasma interaction can be

expected.[67]

However, these codes require very small time-steps (a $dx \sim 1$ nm requires $dt \sim 10^{-19}$ seconds or smaller), and very large numbers of particles to achieve numerical stability (10^8 or more),[67] so large computational resources are required. Due to the large computational resources required and the build up of numerical errors only dynamics around the picosecond timescale can realistically be simulated for denser targets.[68]

Shorter term hydrodynamic-like behaviour has been simulated previously using PIC codes, for example hole boring[69] and the cone tip evolution in cone guided fast ignition.[61,62] It is not currently feasible however to study the progression of shocks through solid density plasmas in a PIC framework without access to extremely large-scale computational power and so an alternative method has been used in this thesis.

Longer-term, several picoseconds, hydrodynamic expansion of a target, after the interaction with a 30 fs pulse, has been explored previously[70,71] using Doppler spectroscopy. The progression of a strong shock from a picosecond length pulse has also been observed[72] using an x-ray diagnostic. Shocks formed from ultra-short ultra-intense pulses are less well studied. In this thesis the later time hydrodynamics is calculated using a simple Lagrangian hydrodynamics code. This code is initialised with the output from a PIC code (for the main-pulse interaction), which has itself been initialised from a radiation-hydrodynamics code (for the pre-pulse).

Chapters 4,5 & 6 present results from several pump-3ω-probe Doppler spectroscopy experiments. All of these experiments were performed on the two short-pulse (30 fs) laser systems present in the UpHill facility at the Tata Institute for Fundamental Research. Chapters 4 and 5 focus on experiments with similar intensity laser pulses but with very different levels of contrast, both show the formation of shocks with varying properties. Chapter 6 focuses on an experiment using a low density foam, several possible explanations for the experimental results obtained

are explored. These include the occurrence of solitons formed as a result of photon-acceleration or stimulated Raman scattering type plasma instabilities.

1.2 Fast Electron Transport

The transport of electrons, accelerated to higher than MeV levels, from the laser interaction region through a solid target, dubbed fast electron transport, is of critical importance to a number of research areas. These areas include the previously mentioned TNSA and fast ignition fusion scenarios. Resistively generated magnetic fields have been shown to have a critical impact on the behaviour of fast electron beams.[73,74] The link between the growth of magnetic fields and the self-collimation of electron beams through solid materials has been previously demonstrated using a rigid beam model.[75]

There are several instabilities that can affect the progress of the electron-beam causing it to filament, spreading the energy the beam delivers over a much wider area. This filamentation of fast electron currents has been observed in several previous experiments.[76,77] Several studies suggest that the formation of filaments is due to a beam-Weibel instability[78,79] caused by differing conditions in the target including both density modulations and target resistivity.[80] The effect of changing the crystal structure of the target material has also been studied.[77,81] Crystalline allotropes of carbon were found to suppress filament growth whilst isotropic disordered allotropes did not.

Chapter 7 describes an analysis of the effect of changing the cold electrical-resistivity on the filamentation of an electron beam, in particular the growth of large-scale restively generated magnetic fields. The growth of large-scale magnetic fields at early times is of critical importance in suppressing the filamentation instability where it would otherwise grow. This implies that the low-temperature resistivity of the material which the fast-electron beam is travelling through is of critical importance

in target design.

1.3 Thesis Outline

Chapter 2 covers some key physical phenomena relevant to the studies conducted for this thesis, as well as describing the theoretical outline for the modelling performed.

Chapter 3 provides a description for the experimental and modeling techniques used throughout this thesis.

Chapter 4 describes experimental and modeling results for a high-contrast 3ω Doppler spectroscopy experiment. This high-contrast laser system produces a shorter length-scale pre-plasma. This chapter is based on work published in ref. 82.

Chapter 5 describes experimental and modeling results for a low-contrast 3ω Doppler spectroscopy experiment. The lower contrast, and therefore larger pre-pulse, produces a longer scale-length pre-plasma which dramatically changes the later time hydro-dynamics. This chapter is based on work published in ref. 83.

Chapter 6 describes experimental and modeling results for a similar experiment to that performed in Chapter 4, however this time using a low density foam target to produce an extended pre-plasma. This extended pre-plasma results in a radically different absorption mechanism and requires significant extension to the methodology used in modeling the previous experiments.

Chapter 7 details a study on the effect of the cold electrical-resistivity on the filamentation of laser-driven fast-electron currents in solid targets. This chapter is based on work published in ref. 84.

Chapter 2

Laser-Plasma Interactions and Plasma Physics

This chapter covers some of the key physical phenomena relevant to the studies described in this thesis. The chapter begins with the description of the key parameters in high-power laser interactions with plasmas, it follows on with a description of some of the phenomena associated with laser-pulse absorption, then a section on Lagrangian hydrodynamics, and finally a description of shock waves.

2.1 Parameters Relevant to High Intensity Laser-Plasma Interactions

2.1.1 The Normalised Vector Potential

The effect of an intense electromagnetic field on a single particle has been studied widely and even before the concept of the laser was first introduced. A parameter commonly used to describe a laser-electron interaction is the normalised vector potential[85] (or quiver velocity) of a laser with frequency ω_l, which is the velocity gained, v_q, by an electron in the laser electric field E_l over one laser cycle, normalised

to the speed of light, given by:

$$a_0 = \frac{v_q}{c} = \frac{q_e E_l}{m_E \omega_l c} = 0.73 I_{18} \lambda_{\mu\mathrm{m}}^2 \tag{2.1}$$

where I_{18} is the laser intensity in 10^{18} Wcm^{-2}, $\lambda_{\mu\mathrm{m}}$ is the wavelength in microns, and q_e denotes the charge of an electron and m_e denotes its mass (the subscript e denoting electrons, a convention continued later for ions and other species). Since v_q is the non-relativistic electron velocity a value of $a_0 \ll 1$ implies a non-relativistic interaction, whilst $a_0 \gtrapprox 1$ implies a relativistic interaction regime. There are two laser systems at the Tata Institute for Fundamental Research that are used in this study: a smaller system with a focused intensity of $I_l = 1 \times 10^{18}$ Wcm^{-2} and wavelength $\lambda = 800$ nm, which gives $a_0 = 0.46$; and a larger system with a focused intensity of $I_l = 2 \times 10^{18}$ Wcm^{-2} ($a_0 = 0.93$), with the same wavelength as the previous system. Normalised vector potentials of $a_0 = 0.46$ and $a_0 = 0.93$, are close enough to the boundary for relativistic behaviour that the importance of such effects must be examined.

2.1.2 The Plasma Frequency

If electrons in an equilibrium plasma are perturbed slightly from their original position a charge imbalance occurs; the electrons will then be pulled back through this position due to the electrostatic field set up by the charge imbalance but will overshoot the equilibrium position. This sets up an oscillation with a frequency dependant on the electron density n_e and permittivity of free space ϵ_0:

$$\omega_{pe} = \left(\frac{n_e e^2}{m_e \epsilon_0}\right)^{\frac{1}{2}} \tag{2.2}$$

This frequency is known as the electron plasma frequency. At finite temperatures electron plasma waves or Langmuir waves are supported at this frequency. A light

pulse with frequency $\omega_l = \omega_{pe}$ will be damped by a resonant electron plasma wave (Langmuir wave[86]). This leads to the idea of a critical density

$$n_{cr} = \frac{m_e \epsilon_0 \omega_l^2}{q_e^2} \tag{2.3}$$

corresponding to the highest density the pulse can be expected to traverse without significant damping.

2.1.3 The Debye Length

A fundamental plasma parameter, used throughout this document is the Debye length λ_D, which is a scale-length associated with the self-shielding behaviour of a plasma. If a charged object is placed into a plasma, the electrons act to shield the potential of the object from the rest of the plasma (i.e. the electrons surround a positive charge, or disperse from a negative charge, until the local charge balance is approximately maintained). Due to their much larger inertia the behaviour of the ions can be ignored when examining this effect. The scale-length of this shielding effect is given by:

$$\lambda_D = \sqrt{\frac{\epsilon_0 k_b T_e}{n_e q_e^2}} = \sqrt{\frac{k_b T_e}{m_e}} \frac{1}{\omega_{pe}} \tag{2.4}$$

2.1.4 The Ponderomotive Force

Electrons (and ions[1]) can also be directly accelerated by a laser pulse via the ponderomotive force associated with a changing electric field **E**:

$$\mathbf{F}_{pond} = -\frac{q_s^2}{4 m_s \omega_l} \nabla E^2 \tag{2.5}$$

[1]Whilst the action of the ponderomotive force on ions is a factor of $\frac{m_i}{m_e}$ smaller than on electrons it may still have an important role.

where q_s is the species charge, m_s is the species mass, and ω_l is the frequency of the oscillating electric field.

The energy spectrum of electrons accelerated ponderomotively has a characteristic temperature which can be calculated using the relativistic gamma factor $\gamma_l = \sqrt{a_0^2 + 1}$, given by:

$$T_f = \gamma_l m_e c^2 = \gamma_l \times 511\,[\mathrm{keV}] \tag{2.6}$$

This fast-electron temperature scaling is used in Chapter 7 to seed a simulated target with fast-electrons in the hybrid code Zephyros (described in chapter 3) to study their transport though the bulk of the target.

2.1.5 The Coulomb Logarithm

The collisionality of a plasma is of importance in determining many plasma properties in relation to instabilities and laser absorption phenomena. The basic quantities that relate to this are the Coulomb logarithm, and the inter-species, and intra-species collision frequencies. The Coulomb logarithm is:

$$ln\Lambda = \frac{b_{min}}{b_{max}} \tag{2.7}$$

where the b_{min} parameter can either be taken as the classical distance of closest approach or the de Broglie wavelength of the ion, and the b_{max} parameter is the range of the Coulomb force, which in the case of a plasma is limited by the Debye sheath and so takes the value of the Debye length. A small value of $ln\Lambda$ will describe a plasma which is strongly coupled by Coulomb interactions.[87,88] The electron-ion collision frequency is then given by:[85]

$$\nu_{ei} \simeq 2.91 \times 10^{-6} Z n_b \ln\Lambda T_b^{-3/2} [\mathrm{s}^{-1}] \tag{2.8}$$

where n_b is the background plasma density, and T_b is the background plasma temperature (in eV). The term scale-length is used throughout this document, it refers to a profile, usually in x, where some variable p decays as a function of x. A scale-length in an arbitrary profile $p(x)$ at a point x_i can be defined as $l = \left|\frac{p(x)}{dp/dx}\right|_{x_i}$.

2.2 Laser-Plasma Absorption and Instabilities

2.2.1 Inverse Bremsstrahlung

Free-free absorption, or inverse bremsstrahlung, is the absorption of a photon with energy $h\nu$ by excitation of a free-electron in the presence of an ion (Thomson scattering involves just an electron and a photon, and is more applicable to lower densities[64]). The absorption coefficient[89] is given by

$$\alpha = \frac{\nu_{ei}}{c} \frac{(n_e/n_{crit})^2}{\sqrt{1 - n_e/n_{crit}}} \tag{2.9}$$

where n_{crit} is the critical density, c is the speed of light, n_e is the electron density and ν_{ei} is the collision frequency previously described. The temperature dependence of α ($\alpha \propto \nu_{ei} \propto T_b^{-3/2}$) indicates that at high temperatures the absorption coefficient drops significantly, and so this phenomena is only important where the laser intensity is small enough that it does not heat the plasma to high temperatures. The dependence on ω_p leads α to be real only when $\omega_l < \omega_{pe}$, i.e. in under-dense plasma where $n_e < n_{crit}$. The dependence of α on n_e^2, and the expression in the denominator, leads to maximum absorption at densities close to the n_{crit}. As a result inverse bremsstrahlung is likely to be important at low intensities (ASE pedestal or pre-pulse intensities of 10^{11-14} Wcm^{-2}) and in cooler pre-plasmas with long scale-length density gradient leading up to the critical density.[63]

2.2.2 Resonance Absorption

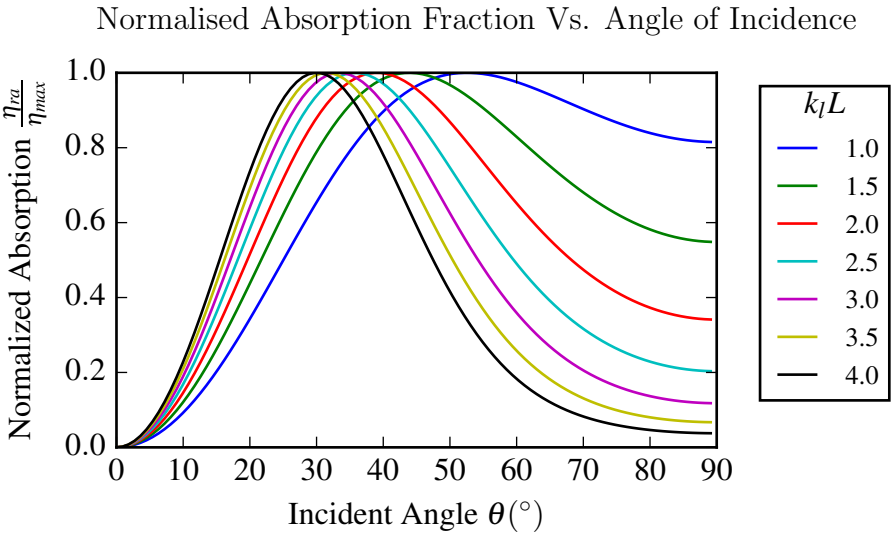

Figure 2.1: Plot of the normalised absorption fraction vs. the angle of incidence from eqn. 2.10 using $\varepsilon = (k_l l)^{1/3}\sin(\theta)$. A number of different values of $k_l l$ are used to calculate η, where $k_l l$ is the normalised plasma density scale-length. It should be noted that a normalised absorption fraction of 1.0 would mean maximum absorption, not 100% absorption.

At high laser intensities ($I \gg 10^{16}$) where electrons are subject to greater v_{osc}, collisional absorption becomes less dominant as the collision frequency decreases with temperature. Take the case where a plane p-polarised laser pulse is incident on a target with a density gradient (e.g. $n_e = n_o \exp(-x/L)$). If the laser pulse is incident onto the density gradient at an angle θ from the normal (the normal being along the x direction), then there will be an electrostatic component in the same direction $|E_x|$ as the density gradient $\frac{dn_e}{dx}$, and so the pulse can separate charges along the x direction. At the point where $\omega_l = \omega_{pe}$ ($x_0 = 0$) the oscillation of charges leads to the excitation of a Langmuir wave with a frequency ω_{pe}. Hot electrons[90–92] are then generated from collisional damping or wave-breaking of the resonantly excited Langmuir waves. A laser pulse travelling at an angle θ (through the same density gradient) will reach a turning point, due to refraction, at a point $x_t = -L\sin^2\theta$ and so the majority of the wave will reflect, though there will be quiescent transmission up to the critical layer where the resonance occurs. Resonance absorption is highly

dependant on the angle of incidence of the incoming laser pulse for a given value of $k_l l$[65] (k_l being the wavenumber of the incoming laser pulse). The absorption fraction for this mechanism is given by:[65]

$$\eta_{ra} \approx 1.15 \left(\epsilon \exp\left(-\frac{2}{3}\epsilon^2 \right) \right)^2 \tag{2.10}$$

where the value of $\varepsilon = (k_l l)^{1/3} \sin(\theta)$ can be used to obtain the angular dependence. A plot of the absorption against the incident angle is shown for a number of values of $k_l l$ in Fig. 2.1.

2.2.3 Short Scale-Length Absorption

At steeper gradients, i.e. where $k_l l \gg 1$, the laser might not be expected to penetrate much further than the skin depth $l_s = \frac{c}{\omega_{pe}}$ before the self-shielding of the background plasma takes over. However a process called vacuum or Brunel heating[65,93] can occur where a thermal electron travelling at speed v_{th} travels into the outer skin depth region, and is then removed by the laser field far beyond the Debye length of the bulk plasma, and out into the vacuum in front of the target. When the field reverses in the second half of the laser cycle the electron is then propelled back into the target. Given the far greater velocity that the electron now has it is much less likely to collide inside the Debye sheath at the front of the target and so instead it will deposit its energy further into the target. A further development of this phenomena occurs in the relativistic regime where the skin depth increases somewhat due to a decreased collision rate in the skin depth (making it deeper) and non-local transport of the higher energy electrons allows them to be propelled further into the target.[65,94]

This is not an exhaustive list of absorption processes (relativistic $\mathbf{J} \times \mathbf{B}$ for example, though this peaks at target normal[65]) however these are likely to be the most relevant collisionless processes at the a_0 values being dealt with here.

2.2.4 Parametric Instabilities

Stimulated Raman scattering is an instability where a large amplitude laser pulse is resonantly coupled with a scattered light wave and a Langmuir wave. If a light wave is travelling through a plasma where there is a ripple in the density ∂n_e along the axis of propagation, i.e. a Langmuir wave with amplitude ∂n_e, then there will be a transverse current associated with the density perturbation and the oscillation of the electrons (see eqn. 2.1) in the laser field, so that $\partial \mathbf{J} = -e\mathbf{v_q}\partial n_e$. If the wavenumbers of the Langmuir wave and the laser pulse are matched properly then the transverse current generated in the Langmuir wave scatters a light wave with amplitude $\partial \mathbf{E}$ which then interferes with the laser pulse so that it modulates it such that $\nabla E^2 \propto \nabla(\mathbf{E_L} \cdot \partial \mathbf{E})$.[95] This modulation of the light pulse ponderomotively pushes electrons out of high field regions into low field regions enhancing the density perturbations in the Langmuir wave. The wave matching criteria for this are that:

$$\begin{aligned} \omega_l &= \omega_s + \omega_{pe} \\ k_l &= k_s + k_{pe} \end{aligned} \tag{2.11}$$

where the subscript l represents a property of the laser pulse, s is a property of a scattered light wave, and pe is a property of a stimulated Langmuir wave. This instability is inherently a kinetic phenomena and so is not widely modelled in hydrodynamic codes, but it can be dealt with in particle-in-cell models. The growth-rate of forward Raman scattering[65,95] is given by:

$$\Gamma_{FRS} = \frac{\omega_{pe}^2 a_0}{2\sqrt{2}\omega_l(1 + a_0^2/2)} \tag{2.12}$$

This growth rate has a non-linear dependence on laser intensity with a peak in a_0 at $a_0 = \sqrt{2}$. The growth rate for backwards Raman scattering[65] is given by:

$$\Gamma_{BRS} = \omega_{pe}\frac{\sqrt{3}}{2}\left(\frac{\omega_l}{2\omega_{pe}}\right)^{\frac{1}{3}}\frac{a_0^{\frac{2}{3}}}{\sqrt{1+\frac{1}{2}a_0^2}} \tag{2.13}$$

Whilst Γ_{BRS} peaks at a slightly higher $a_0 = 2$ it is generally larger than Γ_{FRS}[96] for a given value of a_0. As the laser systems used in this study have a normalised intensity of $a_0 \sim 1$ this instability may occur. The maximum growth rate as a function of ω_{pe} occurs at $\omega_{pe} = \omega_l/2$, or in terms of the laser critical density $n_e = n_{crit}/4$. At the point of maximum growth rate the two-plasmon instability[95] can occur. Both of these instabilities can be linked into a single family of instabilities.[97] For the SRS mechanism to have a significant effect on the absorption of laser light at low densities a long scale length plasma around $n < n_{crit}/4$ must be present.[95] However the damping rate, either of collisional damping to electron plasma waves or damping of the scattered light waves, will also limit the formation of SRS instabilities. Both of these rates are dependant on the electron collision frequency.[95]

A similar instability to SRS, though this time involving light scattering from an ion acoustic wave rather than an electron plasma wave is described by stimulated Brillouin scattering (SBS).[95] This instability occurs when an incident laser pulse resonantly couples with an ion acoustic density perturbation in a similar way to that discussed for electrons above. The ponderomotive force set up by the incident and scattered electromagnetic waves enhances the original density perturbation providing a similar feedback mechanism to that described for SRS. However, given that the typical pulse length of the laser systems used in this study are around $30fs$ it is not thought that this mechanism can play a significant role due to the insufficient timescale for ion motion.

For particularly long length scale plasmas another laser-plasma instability that can occur is the filamentation instability.[95,98,99] This instability occurs in a simi-

lar fashion to the SRS and SBS instabilities except that it occurs in a transverse rather than longitudinal fashion. A small perturbation in the radial intensity profile can generate a perturbation in the plasma electron density, either via a ponderomotive push[98] or the heating of the plasma. Refraction of the incident laser pulse through this density perturbation further enhances the intensity perturbation and so a feedback process leads to the occurrence of an instability.

A related phenomena to the filamentation instability is that of laser-pulse self-focusing,[100,101,101–103] which can also occur not just as as a result of thermal[104] and ponderomotive,[105] but also relativistic effects.[101] Thermal self-focusing arises as a result of collisional heating which can cause local hydrodynamic expansion altering the dielectric of the plasma the pulse is passing through, increasing it at the edges, and decreasing it centrally.[104] Ponderomotive self-focusing[106] occurs in a similar manner, however, the alteration of the electron density occurs as a result of electrons being ponderomotively pushed out of the central high field region of the EM pulse. An additional effect to take into account is the relativistic effect due to electrons being accelerated close to the speed of light.[106,107] The refractive index η of a plasma can be calculated by;

$$\eta = \sqrt{1 - \frac{\omega_{pe}^2}{\omega_l^2}} \tag{2.14}$$

where, for a relativistic plasma $\omega_{pe} = \left(\frac{n_e e^2}{\gamma m_e \epsilon_0}\right)^{\frac{1}{2}}$. For large γ the increase in refractive index can be significant. There is a critical threshold over which ponderomotive self-focusing can occur:[102]

$$P = \frac{m_e^2 c^5 \omega^2}{e^2 \omega_{pe}^2} \approx 17\left(\frac{\omega^2}{\omega_{pe}^2}\right)[\mathrm{GW}] \tag{2.15}$$

For the laser systems used in this thesis, a 20 TW and a 100 TW system as described in section 3.1, and with $\omega_{pe} \sim \omega_l$, the power threshold is marginally achieved by the

20 TW laser system, and certainly achieved by the 100 TW laser system at full power.

2.2.5 Channeling and Hole-Boring

At high irradiances $I\lambda^2 > 10^{18}$ Wcm$^{-2}\mu$m^2, and small focal regions of around $2-10$ μm in diameter, a process called hole-boring or channel formation can occur. This regime was initially studied[14] using 2D PIC codes which show a hole bored several wavelengths deep by a tightly focused normally-incident laser-pulse with a sub-ps duration. This process is essentially a multi-dimensional process with ions at the centre of the laser focus being preferentially accelerated compared to those at the edge of the focal spot. This preference creates a deep crater-like depression in the target surface. The hole boring mechanism can be shown to be essentially due to a pressure imbalance set-up between the laser and the target electron population[14] so that $P_L/P_e \gg 1$. A characteristic velocity associated with hole-boring can be calculated using:[65]

$$\frac{u}{c} = \left(\frac{Z m_e}{m_i} \frac{n_{crit}}{n_e} \frac{(2-\eta)\cos\theta}{4} \frac{I_{18}\lambda_{\mu m}^2}{1.37} \right)^{\frac{1}{2}} \tag{2.16}$$

Using values from the experiments described in chapters 4 and 5, a typical hole-boring velocity can be obtained. The target parameters required are, using a crown glass target, an electron density of 7.5×10^{23} cm^{-3} (assuming full ionisation), an average Z = 20.7, and A = 10.3. The laser parameters can be taken from the Ti:Sapphire laser system, an intensity of 10^{18} Wcm^{-2}, a wavelength of 800 nm, and an angle of incidence of 40°. Finally if an absorption fraction of 0.3 can be assumed, a hole-boring velocity of 8.7×10^6 cms^{-1} is reached. Over the duration of the laser pulse (30 fs) this implies a movement of 2.6 nm. If the region being pushed is not significantly over-critical, say closer to $\frac{n_c}{n_e} \sim 1$, then the hole-boring speed approaches $2x10^8$ cms^{-1} meaning several tens of nanometres of movement during the laser-pulse.

2.3 Hydrodynamics and Shockwave Physics

2.3.1 Lagrangian Hydrodynamics

A system of particles can be described using a distribution function $\hat{f}(\mathbf{v}, \mathbf{x})$, the evolution of such a system in time is given by the Vlasov equation:

$$\frac{\partial \hat{f}}{\partial t} + \frac{\partial \mathbf{x}}{\partial t}\frac{\partial \hat{f}}{\partial \mathbf{x}} + \frac{\partial \mathbf{v}}{\partial t}\frac{\partial \hat{f}}{\partial \mathbf{v}} = C(\hat{f}) \tag{2.17}$$

where $C(\hat{f})$ is the collision operator. Using the assumption that $\hat{f}(\mathbf{v}, \mathbf{x})$ is well described using Maxwell-Boltzmann statistics[108] a set of fluid equations can be derived to give the evolution of this same system in terms of the macroscopic properties: pressure $\mathbf{P}$, density ρ, fluid velocity $\mathbf{u}$, and internal energy e (or temperature T). It is worth noting that the assumption of a Maxwellian distribution for $\hat{f}$ assumes that at small scales collisional behaviour dominates at the microscopic scale, so that any deviation of a fluid element in a volume dV from Maxwell-Boltzmann statistics is small and short lived. This assumption is broken in cases where collective particle motion occurs (i.e. plasma instabilities) or where particle species are subject to fewer collisions (e.g. at high temperatures or very low pressures) and so maintain a non-Maxwellian distribution for an extended time. Rather than presenting the full derivation using moments of the distribution function a simpler explanation based on phenomenological arguments[64] is given here. Considering mass conservation inside a volume dV, the amount of mass inside the volume must be equivalent of the mass flowing across the surface of the volume element, which gives an equation of mass conservation (sometimes referred to as a continuity equation):

$$\frac{d}{dt}\int_V \rho dV = -\int_S \rho \mathbf{u}.d\mathbf{A} \tag{2.18}$$

The differential form of this equation is:

$$\frac{\partial \rho}{\partial t} + \nabla.(\rho \mathbf{u}) = 0 \tag{2.19}$$

A useful quantity is the Lagrangian or convective derivative, where the convective derivative of a quantity g is defined as:

$$\frac{Dg}{Dt} = \frac{\partial g}{\partial t} + \mathbf{u}.\nabla g \tag{2.20}$$

The Lagrangian viewpoint considers an element of fixed mass rather than fixed volume, effectively fixing a spatial grid to the fluid. By constraining the grid cells to have a fixed mass rather than being fixed in space, the continuity equation is dramatically simplified to:

$$\frac{D\rho}{Dt} = 0 \tag{2.21}$$

The convective derivative version of the continuity equation takes into account mass flow by allowing the fluid element to expand and move with the fixed mass in the element. To obtain momentum conservation the continuity equation can be multiplied by $\mathbf{u}$, which equates the momentum of the volume element with the momentum of the material exiting the surface of the element. To complete the equation the pressure gradient ∇P across the boundary of the material, which will act to increase momentum transfer, and any other forces ($\mathbf{F}$) that act on the fluid (e.g. gravity) also need to be considered:

$$\frac{D(\rho \mathbf{u})}{Dt} + \nabla P = \mathbf{F} \tag{2.22}$$

Energy inside a fluid element and transferred across its border can be thought of in two parts: firstly thermodynamic (the internal energy e of random particle movement) and secondly mechanical ($\frac{1}{2}\mathbf{u}^2$, the average kinetic or drift motion of the

particles). The thermodynamic contribution will include the internal energy ρe of the element, the heat flux across the surface of the element $\rho \mathbf{u} e$, and the work done associated with the pressure inside the element $p\nabla.\mathbf{u}$, and any external heat source q. The mechanical energy includes the overall kinetic energy of the element $\frac{1}{2}\rho u^2$, the KE flux across the surface ($\frac{1}{2}\rho u^2 \mathbf{u}$) and convective effects over the pressure gradient across the surface $\mathbf{u}.\nabla P$, which does assume a scalar pressure P (i.e. isotropic pressure and so ignores viscosity) and any external force term $\mathbf{F}$. The Lagrangian conservation of energy is now:

$$\frac{D}{Dt}\left(\rho e + \frac{1}{2}\rho u^2\right) + \nabla.(P\mathbf{u}) = \rho q + \mathbf{u}.\mathbf{F} \tag{2.23}$$

Which equates the evolution of the energy contained within the fluid (internal energy, kinetic energy, and pressure) on the L.H.S. with the external energy sources on the R.H.S. There still needs to be closure in P and so an equation of state is used. This equation of state could be from an ideal gas (as used in the Lagrangian code employed in this study and described in the next chapter). In fields such as astro-physics quite often some form of adiabatic (sometimes referred to as polytropic) equation of state is used, or the EOS can be taken from pre-calculated and tabulated values (as can be used in HYADES). For example an ideal gas adiabatic equation of state might look like:

$$PV^{\gamma} = const \tag{2.24}$$

where γ is the adiabatic index of the fluid, and $V \equiv \frac{1}{\rho}$ is the specific volume. In most laser plasma simulations the ρq term is supplied from some energy deposition model for laser plasma interactions, which are talked about later in this chapter, and the last force term due to gravity is ignored on short timescales.

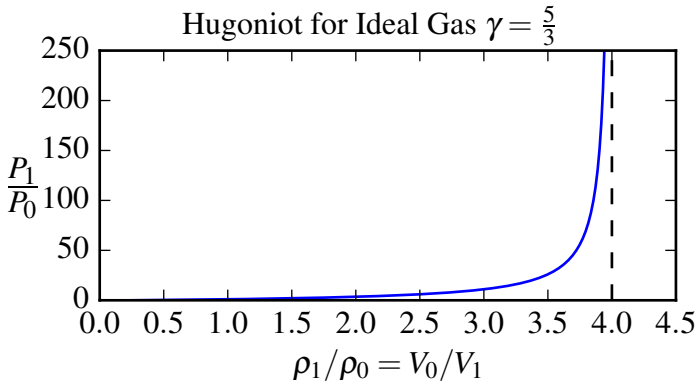

Figure 2.2: Hugoniot curve for an ideal gas with $\gamma = \frac{5}{3}$, calculated with eqn. 2.32.

2.3.2 Shock Waves

Shock waves are, at a basic level, discontinuities in the hydrodynamic variables that travel through a material faster than the local sound speed in the material ahead of them. They can occur when a driver, in this case energy deposited by a laser pulse, launches a compression wave by heating a volume of material. A shock front is a discontinuity though which mass flows from one side with a low sound speed to the other with a higher sound speed.

In a real fluid the shock front would not be exactly discontinuous, but at relatively low pressures would have an extremely sharp gradient. The size of the length-scale associated with the sharp gradient depends on the mean-free path of particles and energy transport phenomena in the material.

The properties of a collisional shock (collisionless shocks do occur in astrophysical plasmas and some laboratory plasmas[108]) are defined by the Rankine-Hugoniot equations. The Rankine-Hugoniot equations can be derived from the Lagrangian conservation equations described above, however only a brief overview will be given. By integrating each conservation equation over the thin layer of the shock front (between say x_0 and x_1, $(x_1 - x_0) = \Delta x$), and taking the limit as $\Delta x \to 0$ of each result, the relationships between the conditions behind the shock (the shocked material)

and in front of the shock (un-shocked material) can be arrived at:

$$\rho_0 \mathbf{u_0} = \rho_1 \mathbf{u_1} \tag{2.25}$$

$$P_1 + \rho_0 u_0^2 = P_0 + \rho_1 u_1^2 \tag{2.26}$$

$$h_1 + {}^{u_1^2}\!/_2 = h_0 + {}^{u_0^2}\!/_2 \tag{2.27}$$

where h denotes the specific enthalpy (sum of internal energy and energy due to pressure), P is pressure, $\mathbf{u}$ is the fluid velocity and the subscripts 1 and 0 relating to shocked and un-shocked material, respectively. From these equations the following conditions can be obtained:

$$\Delta(\rho \mathbf{u_x}) = 0 \tag{2.28}$$

$$\Delta(P + \rho u_x^2) = 0 \tag{2.29}$$

$$\Delta(h + \frac{u_x^2}{2}) = 0 \tag{2.30}$$

these conditions, including conditions that $\Delta \mathbf{u}_z$ and $\Delta \mathbf{u}_z$, comprise the Rankine-Hugoniot Jump conditions. With some substitution and combination of the above equations[89] the following equations can be obtained:

$$\begin{aligned} h_1 - h_0 &= \frac{1}{2}(P_1 - P_0)(V_0 + V_1) \\ \frac{1}{2}(u_1^2 - u_0^2) &= \frac{1}{2}(P_1 - P_0)(V_0 + V_1) \end{aligned} \tag{2.31}$$

where $V \equiv {}^1\!/_\rho$. With an equation of state, for example eqn. 2.24, a Hugoniot curve for an ideal gas can be obtained:[89]

$$\frac{P_1}{P_0} = \frac{(\gamma+1)V_0 - (\gamma-1)V_1}{(\gamma+1)V_1 - (\gamma-1)V_0} \tag{2.32}$$

There is a limiting condition for the compression a shock can impart on shocked

materials (the asymptote visible in Fig. 2.2), this can be found by rearranging the above equation for the ratio of densities and taking the limit as $P_1 >> P_0$:

$$\frac{\rho_1}{\rho_0} = \frac{\gamma + 1}{\gamma - 1} \tag{2.33}$$

The maximum compression of the material by the shock is defined by the adiabatic index, and so an ideal gas with $\gamma = 5/3$ would give a compression ratio of $\rho_1/\rho_0 = 4$. There are several phenomena ignored by this treatment, most of which relate to transport of energy and/or particles across the shock boundary, some of which can be treated using additional modelling with varying degrees of success. The HYADES code used in this study has limited models for both radiation transport and electron thermal transport.

Chapter 3

Experimental and Modelling Techniques

The focus of this chapter is on describing the key physics used in the simulation codes employed in the studies described in this thesis, as well as the key features of the experimental techniques used in obtaining data. This chapter starts with a description of Doppler spectroscopy and its use in measuring velocities. This diagnostic is used to obtain the results that are shown in chapters 4 through 6. The second half of this chapter describes the modelling techniques that have been employed. This starts with particle-in-cell codes, continues with a description of the fluid model and transport models used in the HYADES code, and finishes with an overview of a hybrid fast electron transport code, Zephyros, which is used in Chapter 7.

3.1 The UpHill Laser Facility

The experiments described in this thesis were performed at the UpHill facility located at the Tata Institute for Fundamental Research in Mumbai, India. The experiments described in chapter 4 and 6 were performed on the same 100 TW laser

system, with the experiment described in 5 being performed on the slightly smaller 20 TW system at the facility. Both systems employ Ti:Sapphire oscillators with a central wavelength of ~ 800 nm and are amplified with a chirped-pulse amplification set-up, however the 100 TW system uses several additional amplifiers and a contrast booster.

The smaller 20 TW system uses a Kerr-lens mode-locked oscillator pumped with a 528 nm (2ω) Nd:YVO4 laser, with the resulting 800 nm pulses have a bandwidth of approximately 60 nm. The pulses from the oscillator are then chirped using a grating to stretch them temporally to 200 ps, which allows the pulses to be amplified without damage to amplifiers. The stretched pulses are shaped using an acousto-optics programmable dispersive-filter (Dazzler), this is done to prevent gain-narrowing during amplification and so ensure the efficient compression of the pulse. The pulses are then fed into a regenerative amplifier, via a Pockel cell, where the pulses are amplified to 45 mJ. The pulses then make seven trips through a Ti:Sapphire crystal which is pumped by two 532 nm (2ω) Nd:YAG lasers, amplifying them to an energy of ~ 500 mJ per pulse. The amplified pulses are then fed into a vacuum chamber where they are compressed using an identical pair of gratings, though placed in the opposite configuration, to those used at the stretching stage to a final pulse length of 35 fs.

The larger 100 TW laser system consists of a similar set-up with a Kerr-lens mode-locked oscillator this time pumped using a 532 nm (2ω) Nd:YAG laser, resulting in an 800 nm pulse with a similar bandwidth to the previous laser system of 60 nm. A diagram of the basic set up is seen in Fig. 3.1. The pulses are then fed into a contrast booster consisting of a Ti:Sapphire amplifier (fed with a Nd:YAG laser) which amplifies a pulse to μJ energies which is then fed into a pulse selector, and on into a solid-state saturable absorber to improve the contrast of the seed pulse. At this stage the pulse is $10 - 20$ fs in length and has $1 - 10$ μJ of energy per pulse. The pulse is then stretched to 200 ps using a pair of gratings, similar

to those in the 20 TW system, and then amplified to 1 mJ before being sent to a second pulse selector. After selection the pulse is expanded to a radius of 1 mm, and sent through a Pockel cell, before being amplified to 20-30 mJ by a regenerative pre-amplifier, sent through a second Pockel cell and expanded to 5 mm, and then amplified through 4-passes through a Ti:Sapphire amplifier to 600 mJ. At this point the pulse is expanded to 250 mm and sent for 4 passes through a cryogenically cooled amplifier to amplify the final pulse to an energy of 3.5 J. The pulse is then compressed via a set of gratings identical to, but with the opposite configuration, the pulse stretching stage. The final pulse has a spectral width of 60 nm, a central wavelength of 800 nm, an energy of 2.5 J, and a pulse length of 30 fs, which can be

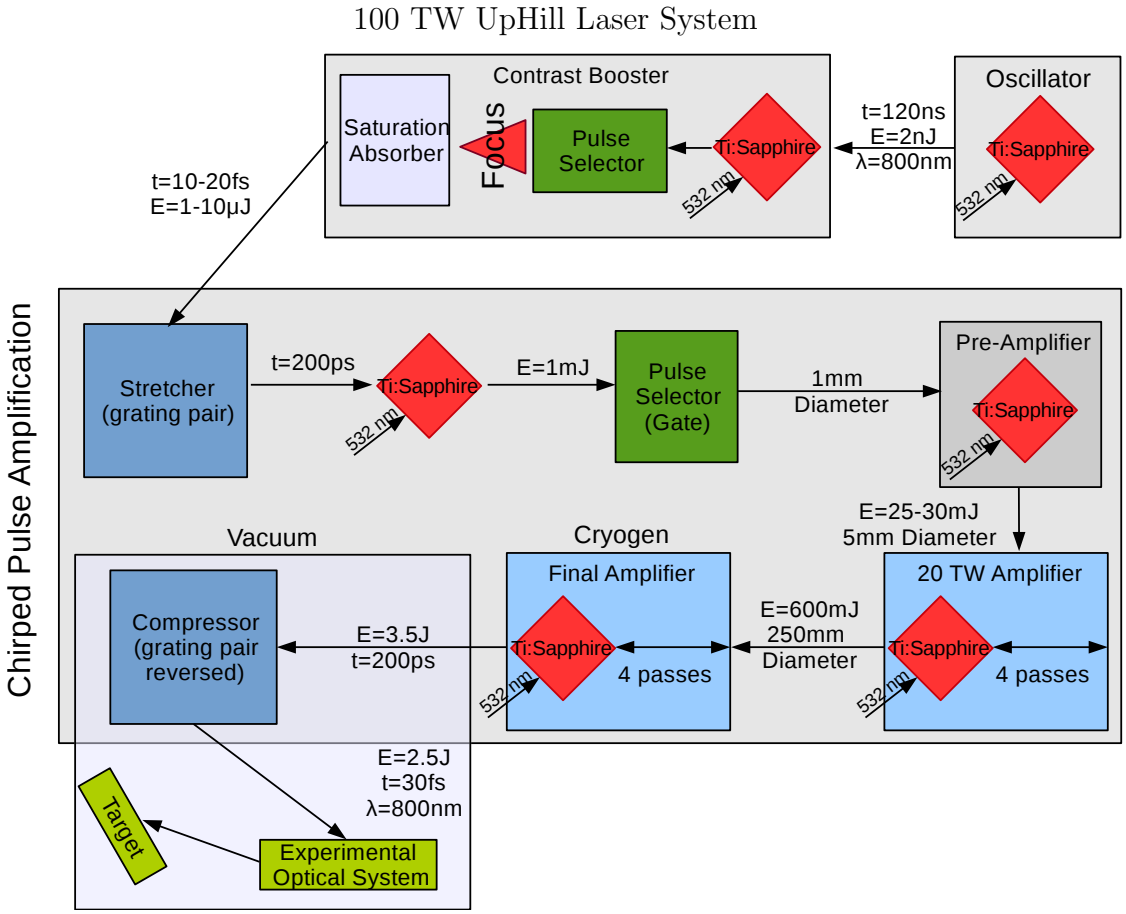

Figure 3.1: Schematic overview of the 100 TW laser system at the UpHill facility located at the Tata Institute for Fundamental Research. This setup produces a pulse with properties; λ = 800 nm, bandwidth 60 nm, t_l = 30 fs, energy 2.5 J, and a focussed intensity of 10^{19-20} Wcm^{-2}.

focused up to 10^{19-20} Wcm^{-2}.

The main pulse of the laser in all of the experiments is plane polarised and the beam axis is angled at 40° to the target front-surface normal to ensure optimum absorption (see fig. 2.1). The spot size (FWHM) of the pump pulse is measured to be 14 μm on the target, resulting in a peak intensity of $I_l \sim 9.5\times10^{17}$ Wcm^{-2} for the smaller laser system and $I_l \sim 2\times10^{18}$ Wcm^{-2} for the larger system. The pump-pulse is preceded by a pre-pulse, and has been measured to have a nanosecond intensity contrast of 10^5 (see the contrast profile in Fig. 5.1) for the smaller system and 5×10^6 for the larger (see the contrast profile in Fig. 4.1).

3.2 Doppler Spectroscopy

Doppler Spectroscopy, in the context it is discussed here, is a technique for using the reflected spectrum of a low intensity probe-pulse to calculate the velocity of a critical surface. The fact that a pulse of light will reflect at its critical density, which is a function of its frequency, allows the probing of different points in a density gradient using probes of different frequencies. The velocity of the critical surface that the probe reflects from is calculated from the measured Doppler shift of the reflected signal, $\delta\lambda$, using the formula:[83]

$$u_{cr} = -0.5c\frac{\delta\lambda}{\lambda} \tag{3.1}$$

The probe pulse is required to be of a low enough intensity that it does not perturb the plasma. It should also be short enough that the temporal evolution of the critical surface velocity can be obtained with sufficient resolution that any features of interest can be resolved. At the intensities used in the experiments in this thesis a sub-ps resolution is required and so the probe-pulse is obtained from a small amount of diverted main pulse (which has a duration of 30 fs) using a beam splitting system.

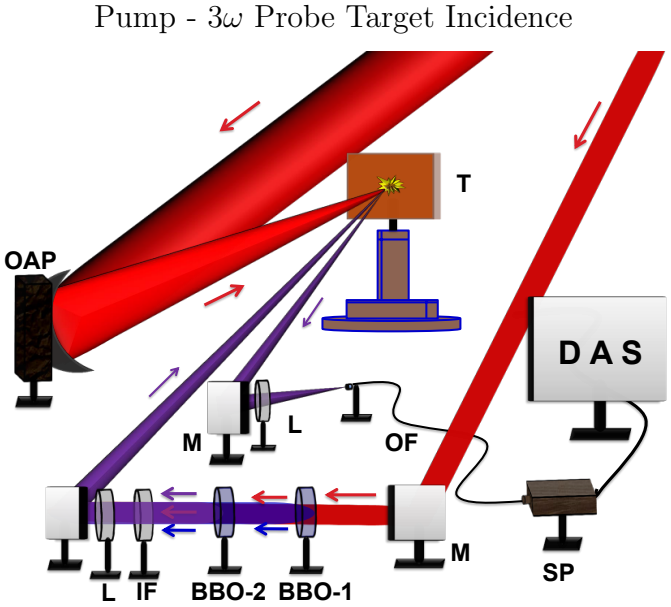

Figure 3.2: Diagram originally published in Ref. 83 showing the basic experimental setup. The 800nm pump laser (red cone) is incident at 40° onto the target front surface, whilst the frequency tripled 266nm pulse (purple cone) is reflected off at an angle near to normal (around 5°) off the surface of the target. Labelled Components: Off axis parabola (OAP), mirror (M), lens (L), interference filter for 266 nm (IF), β-barium borate crystal (BBO), spectrometer (SP), target (T), optical fibre (OF), data acquisition system (DAS).

The output of the beam splitting system is converted to a higher harmonic (e.g. 2ω or 3ω). The higher the frequency of the probe pulse the higher the density of plasma that can be diagnosed. Here a 3ω probe is employed enabling a probe-critical surface of $n_{3\omega,Crit} = 1.6 \times 10^{22}$ to be resolved. To up-shift the probe to 3ω a pair of β-barium borate crystals are used followed by a 266 nm interference filter to reduce the spectral width of the probe-pulse to a FWHM of < 3 nm.

A spectrometer is used to measure the reflected probe pulse spectra which is then used to calculate the instantaneous velocity of the probe-critical surface. Spectral measurements are taken with the Avaspec-3648-USB2 spectrometer which has a spectral resolution of 0.02 nm and a peak sensitivity of 260 nm. This measurement requires that the probe pulse (see Fig.3.2) is as close to normal to the front surface of the target as possible (around 5° due to space limitations inside the target chamber). The probe pulse is sent through a delay stage to add a variable delay so

that the time evolution of the probe-critical-surface velocity can be obtained.

3.3 Modelling Techniques

There are a variety of methods for simulating plasma dynamics, however there is no one-size-fits-all computational technique. For modelling large length and time scales, i.e. length-scales much longer than the electron mean-free-path $\lambda_{e,MFP}$, and timescales significantly greater than the mean collision time $\tau_{coll} = \frac{1}{\nu_{coll}}$ (for electrons or ions), fluid models describing local averages can be used. These techniques accurately model phenomena like acoustic waves, shock like disturbances, and flow. At shorter lengths, and more importantly for this study, time-scales, kinetic models are more appropriate, though these models do come at a significant computational cost.

3.3.1 Kinetic Modelling: The EPOCH Particle-in-Cell Code

PIC simulations allow a continuous phase-space (barring numerical precision) for particles whilst having a discrete electromagnetic field. Such simulations are, in the present context, used to calculate the dynamics of a system on a very short length and/or times-scale.[67] No particle distribution beyond the initial conditions is assumed and so they can be very useful when describing problems where Maxwellian velocity distributions, or local thermal equilibrium, cannot be assumed. However there is still a simplification from an actual plasma system, in so far as that it is not at all practical to simulate $10^{22}/cc$ particles, and so 10^{6-9} *macro-particles* are used to represent clouds of particles.[67] The run-time framework of a PIC code is shown in Fig. 3.3. Particles are firstly assigned a field value (e.g. electric-field) based on their position in the grid and their *shape* which is an alternative way of describing the interpolation regime between points in the discretized EM field grid.[67] There are three shape functions implemented in EPOCH:[2] a third order spline, a linear

(top hat) shape that is discontinuous in space, and a second order (triangular) shape that is discontinuous in velocity. The third order spline is usually the best option for accurate interpolation and is the shape function used throughout this study.

The dielectric function of the PIC code only coincides with the physical one if the cell length $\Delta x < \lambda_d$, so $\Delta x \sim\propto T_e^{1/2}$, i.e. when the Debye length is well resolved by the grid.[109,110] When the Debye length is not properly resolved the aliasing of low frequency modes with higher frequencies can result in self-heating and nonphysical coupling of low frequency EM oscillations.[111,112] However, in practice, maintaining $\Delta x < \lambda_d$ is very challenging, particularly in cold dense plasma. Using the 3rd-order spline interpolation and the current smoothing algorithm implemented in EPOCH can help to mitigate this problem when this condition cannot be met.[68]

After the interpolation of the fields to the particle position, the equations of motion for each individual particle must be integrated. Fields and therefore forces are numerically integrated which makes them subject to counting error. This implies that the error in the calculation is a slow function of the number of particles (a scaling of $N^{-1/2}$), which also implies a heavy computational cost if the counting error is to be minimised.

3.3.1.1 Explicit vs. Implicit Time Integration

There are a variety of methods that can be used for time integration. These methods can be split into two broad categories; explicit solvers which update the location and velocity of a particle using the existing force acting on it, and implicit solvers

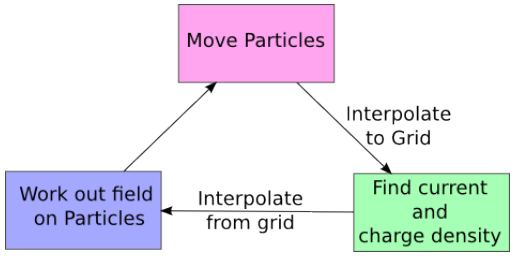

Figure 3.3: The basic framework of a particle/cloud-in-cell code.

which find a solution using the existing state and the later one. Explicit time-integration methods like the forward Euler, the leapfrog, and explicit Runge-Kutta require simpler implementation and, at least for a given time-step, are faster to run than implicit time-integration methods. Examples of PIC codes implemented using explicit time integration are the EPOCH code[2] and the OSIRIS code.[113,114]

Implicit time-integration in PIC codes either use complex algebra, or iterative methods, to calculate the new field (and thus the force on the particle) and use both the old and new field to calculate the new velocity and position of the particle in the next time step. The LSP PIC-Hybrid code[115,116] uses an implicit method in it's kinetic solver to calculate the particle momentum from the time-step n to $n+1$ using half the the electric field at the old position at n, and half at the new position at $n+1$. The velocity of the particles is calculated so that the effect of the magnetic field on the particle is also applied in two pushes, taking the new electric field into account in the second push only. The current density δJ is calculated using $\delta J =< S > \cdot \delta E$ with the susceptibility scattered to the discrete grid in the first push. The current density can be calculated so that the local charge density is conserved. An additional advantage of this method is that if the particle remains in the same cell after the second push, the energy is also conserved to first order.[115] A full description of the algorithm used in LSP is available in Ref 115.

Only when $\omega_{pe}\Delta t < 1$ are explicit simulations numerically stable.[117] However, this still compares well when considering the stronger criteria in an explicit code that $\Delta t < \frac{\Delta x}{c}$, given the extremely small grid resolution required $\Delta x < \lambda_D$. The relaxation from an extremely small Δt in an explicit code to one comparable with $1/\omega_{pe}$ in implicit codes can result in a significant gain in speed, particularly for denser plasmas where λ_D is very small. In addition to this the electromagnetic fluctuations are reduced in an explicit algorithm[115] by roughly $1 + (\omega_{pe}\Delta t)^2$ but reduces to the explicit formulation for regions in which $\omega_{pe}\Delta t \ll 1$. However when the timestep is set to such a large value frequencies such that $\omega > \omega_{pe}$ are not resolved.

3.3.1.2 Initial Conditions and Boundary Conditions

The initial conditions for a PIC code consist of two parts. The first set of initial conditions concern the macro-particle sizes, positions and velocities, which can distributed continuously in phase space according to some physical parameters (e.g. a density/temperature gradient). The second set includes the electromagnetic field grid, possibly initialised with a laser pulse in an empty region of the simulation cell (alternatively using a laser solver attached to a boundary in the case of EPOCH).

A problem can occur when simulating systems with large density gradients, if the macro-particle size is fixed on a per-species basis, then low density regions may be statistically under represented. To maintain reasonable statistics across the entire simulation domain a variable macro-particle size is implemented in EPOCH. Thus the density can be represented by varying the macro-particle size and so maintain the maximum number of particles-per-cell. It is worth noting that while variable-sized macro-particles can help resolve large density gradients on initialisation, the problem of poor statistics in a given cell can still occur at later times in the simulation.

EPOCH allows for several different boundary conditions which can apply to either fields, particles, or both. The basic boundary conditions available include: periodic, reflecting (clamping fields to zero) and outflow. There is also a laser outflow boundary, which lets particles and fields leave through the boundary as well as attaching a laser solver. While support exists for convolution perfectly-matched layer boundary-conditions,[118] these were found not to have a significant impact on the results of the simulations performed, and so only the outflow and laser outflow boundaries are used here.

3.3.1.3 Ionisation Modelling

There are a number of ionisation models in EPOCH. The field-ionisation flag uses a model which includes multi-photon ionisation and tunnelling ionisation with a

barrier suppression correction. Through an additional flag collisional ionisation is also available. A single macro-particle ionisation event in EPOCH results in the creation of a new particle and a change in the charge of the old particle. As a result the initial number of particles-per-cell can increase up to an amount $N_s Z_{s,max}$, where N_s is the initial number of particles in the simulation, and $Z_{s,max}$ is the maximum ionisation level of that species and for this reason a large amount of computational power is required to run simulations involving ionisation.

3.3.1.4 Particle Collisions

EPOCH implements a sophisticated collision model which is outlined in Ref. 68. There are several ways to alter the collisionality of the plasma in the simulation, the Coulomb logarithm can either be input manually so that it has a fixed value throughout the simulation, or it can be calculated automatically on a cell-by-cell basis from the local temperature in a simulation cell; both of these approaches are tested in parts of this study. There is also scope for changing the collision frequency by a scaling factor, though this feature was not used in this study. By discretizing the EM field the computational time required to run a code with N particles goes from scaling with N^2, in the case with a continuous field, to scaling with $N \log N$ with discretized fields. Adding collisions to a PIC code has a major impact on its performance, increasing the time taken to perform a single step by a factor close to n, the number of particles per cell. In addition to this problem it was found, whilst performing the simulations in this study, that using collisions significantly increases the noise in the simulations and in such cases up to a factor of 10 increase in the number of particles per cell is required to achieve convergent behaviour.

3.3.1.5 VFP vs. PIC

There are two popular approaches to simulating kinetic problems: Vlasov-Fokker-Planck (VFP), and the Particle-in-Cell (PIC) described above. VFP codes solve a

kinetic equation based on a distribution function $\hat{f}(\mathbf{x}, \mathbf{v})$ (eqn. 3.2) using an initial distribution and then using either implicit or explicit time-integration.

$$\frac{\partial \hat{f}}{\partial t} + \frac{\partial \mathbf{x}}{\partial t}\frac{\partial \hat{f}}{\partial \mathbf{x}} + \frac{\partial \mathbf{v}}{\partial t}\frac{\partial \hat{f}}{\partial \mathbf{v}} = C(\hat{f}) \tag{3.2}$$

The function $C(\hat{f})$ contains the effects of collisions on $\hat{f}$. VFP codes are often discrete in both velocity and configuration space, with the ions usually assumed to be a cold fluid. A good review of current VFP codes is available in Ref. 119. Most VFP codes assume a quasi-neutral plasma, though some do utilise models capable of supporting plasma currents, which enable the addition of some types of laser model. The same can be said for ionisation, whilst most codes employ a fixed ionisation, some are available that support dynamic ionisation. Given the importance of the laser-plasma interaction in the experiments described in chapters 4-6 a PIC code is employed rather than a VFP code.

3.3.2 Fluid Calculations

There are three main types of hydrodynamics codes: Lagrangian (described here), where the grid is fixed to the fluid flow; Eulerian (POLLUX[120] is an example of a Eulerian 2D Rad-Hydro code), where a fluid flows through a fixed spatial grid; and the Arbitrary Lagrangian/Eulerian (ALE) formalism, where the grid can be moved in relation to the fluid and a fixed background as required.

HYADES[1] is a Lagrangian radiation-hydrodynamics code used extensively in the studies described in this thesis to model the low intensity laser-plasma interactions that happen throughout the pre-pulse interaction with the plasma. Another code that is used in these studies is a simple 1-D Lagrangian hydrodynamics code, using an ideal-gas adiabatic equation of state. This latter code is used to study plasma evolution at later times using the initial conditions generated by HYADES and EPOCH. As opposed to PIC and VFP formalisms, at length-scales much larger

than λ_D or λ_{MFP}, and timescales much larger than $\tau_{collision}$, a local average or fluid approximation is appropriate. These codes typical run significantly faster than PIC or VFP based simulations. These fluid models are based on local parameters of; density ρ, pressure P, fluid velocity $\mathbf{u}$, and internal energy (either through enthalpy h or temperature T). Both HYADES and the basic fluid code used in this study use the Lagrangian formalism described in section 2.3.1. The formulae of particular importance to the implementation of this type of hydrodynamic simulation are: momentum conservation, (eqn. 2.22); energy conservation, (eqn. 2.23); and the equation of state, which can be either a table of values or calculated by an adiabatic equation such as eqn. 2.24. The mass conservation equation (eqn. 2.21) is taken care of by fixing the mass (or number density) in each cell, and so each cell expands/contracts in space depending on the calculated density. In the case of HYADES rather than fixing the fluid mass, there are two fluids: ion and electron. The ion fluid has a fixed n_i and the electron fluid has a fixed initial n_e which is then only modified by local ionisation.

The initial conditions for a hydrodynamics code include a grid with cells containing values for ρ, $\rho\mathbf{u}$ and $\rho e + \frac{1}{2}\rho u^2$. The grid of cells are usually 1 or 2D in nature, though there are 3D codes in use. A time-step consists firstly of solving cell conditions for ρ, $\mathbf{u}$ and e; then, given ρ, $\mathbf{u}$ and e, an equation of state is used to find P; next time derivatives are calculated ($\frac{\partial \rho}{\partial t}$, $\frac{\partial \rho \mathbf{u}}{\partial t}$ and $\frac{\partial(\rho e + \frac{1}{2}\rho u^2)}{\partial t}$). Finally the values of ρ, $\rho\mathbf{u}$ and $\rho e + \frac{1}{2}\rho u^2$ are calculated for the next time step using a time integration scheme (e.g. leap-frog), see Fig. 3.4. Care must be taken to maintain numerical stability by ensuring neighbouring cells have similar masses.

The price that is paid for the simplification of the Lagrangian is in the eventual distortion of the grid. After some time the spatial resolution in the lower density parts of the simulation is greatly reduced and so the grid has to be set up carefully so that there is sufficient resolution to properly resolve external influences on the fluid. The front surface of a solid target, and the region around the critical density, are

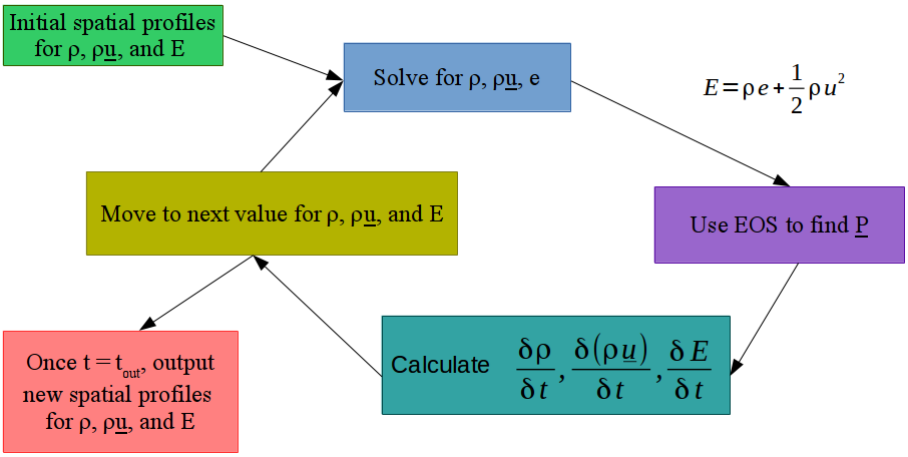

Figure 3.4: Basic operational scheme for a hydrodynamics simulation.

both subject to considerable expansion and so a large number of cells around these regions is required to maintain adequate resolution. The fluid can be re-gridded before the grid becomes too sparse, however this interpolation is subject to intrinsic error. The main advantage of a Lagrangian perspective over an Eulerian one, where the grid is fixed in space, is that vacuum expansion can be modelled and interfaces between materials can be properly resolved.

Discontinuities, like shocks, present a problem when using a finite grid cell size, however a form of artificial viscosity[121,122] can be used to stabilise shocks in this situation. This method effectively smears shocks out somewhat so that the shock front has a thickness comparable to the cell size of the system to enable the code to cope with the nearly discontinuous nature of these phenomena. It also prevents the collapse of a cell if the velocity gradient across it is in the wrong direction.

3.3.2.1 Deviation from Perfect Fluid Assumption

HYADES comes with models for thermal conduction and radiation transport, as well as models dealing with deviations from a Maxwellian distribution. To include thermal transfer Fourier's law can be used, where the heat flux density is given by:

$$\mathbf{Q} = -K\nabla T \tag{3.3}$$

The thermal conductivity K can be calculated in various ways. This can be added to the energy equation as a volumetric energy source term e.g. $-\nabla.Q$, which gives an energy equation of the form:

$$\frac{D}{Dt}\left(\rho e + \frac{1}{2}\rho u^2\right) + \nabla.\left(p\mathbf{u} + K\nabla T\right) = 0 \tag{3.4}$$

Though there has been significant work in developing alternative models, by far the most common model for thermal transport in a plasma is a flux-limited Spitzer-Harm (SH) model.[65] The SH thermal conductivity is dependant on electrons to carry thermal energy. As this model is only intended to work at higher temperatures, mechanisms like lattice-phonon transfer are ignored, and so the conductivity is dependant on the density of electrons n_e through the Coulomb logarithm $\ln\Lambda$, and the electron temperature T_e. The classical Spitzer-Harm transport equation[123] is given by:

$$K = \frac{32}{e^4\sqrt{2m_e^3\pi^3}}\frac{T_e^{5/2}}{Z\ln\Lambda} = 2\times10^{-4}\frac{T_e^{5/2}}{Z\ln\Lambda} \tag{3.5}$$

There are two assumptions that this implies, firstly that there is no significant deviation of electron velocities from the Maxwell distribution, and secondly that the electron mean free path is much shorter than the temperature scale-length. These assumptions break down in extremely short scale-length plasmas and around large thermal gradients. At this point the Spitzer-Harm model over-predicts transport[124] and so some form of flux limiting is needed to restrict the heat flux to physically meaningful levels. The simplest form of limiting[64] is a fixed cap f:

$$Q_{fl} = f n_e k_b T_e v_{th} \tag{3.6}$$

where $v_{th} = \sqrt{k_b T_e / m_e}$. There are a range of possible choices for a value of f; these are discussed in later chapters.

3.3.2.2 Radiation Transport and Atomic Physics Parameters

Radiative transport is very important in the pre-plasma and around the critical density of the laser-target interaction and so must be considered. HYADES comes with a diffusion model for emulating radiation-transport and this also allows for the inclusion of ionisation and various means of calculating, or reading, opacity data. In a hot material the radiation field can have significant effects on the energy transport, e.g. radiative pre-heat in front of a shockwave. The spectral intensity I_ν is defined as the energy crossing a unit area A per unit time t, per unit frequency ν, per unit solid angle Ω in a particular direction, so that:

$$I_\nu = \frac{\Delta E}{A\,\delta\nu\,\delta t\,\delta\Omega} \tag{3.7}$$

Considering a cut-off cone of unit length and angular divergence $\delta\Omega$ co-moving with radiation travelling through a hot medium (see fig. 3.5), in the direction of a unit vector $\mathbf{n}$, with initial aperture A. The spectral intensity I_ν of radiation within the cone at a time $t+\delta t$ will be the same unless some radiation is lost or gained from the intervening medium. Spectral intensity gain j_ν is through emission of radiation from the hot material the cone is travelling through, and is not normally dependent on I_ν. The spectral intensity loss term is dependant on the incident spectral intensity and so is denoted $-k_\nu I_\nu$, where k_ν is the spectral absorption coefficient. This gives us the radiation continuity equation:[64,125]

$$\frac{1}{c}\frac{dI_\nu}{dt} + \mathbf{n}\cdot\nabla I_\nu = j_\nu - k_\nu I_\nu \tag{3.8}$$

The emission and absorption of radiation can be coupled with the Euler equations by addition of the energy g^0 and momentum exchange rates $\mathbf{g}$ to the relevant con-

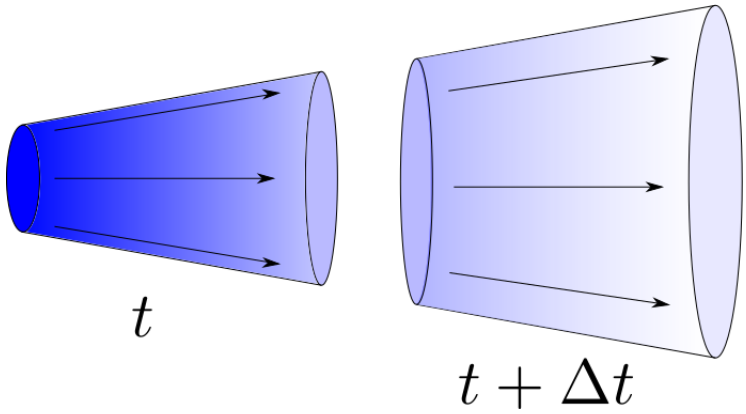

Figure 3.5: Diagram representing the cutoff cone of radiation, cone is of unit length, angular divergence is conserved, the spectral intensity I_ν within the cone is conserved unless the material it is travelling through emits or absorbs some radiation.

servation equations:

$$g^0 = \int d\nu \int_{4\pi} d\Omega (j_\nu - k_\nu I_\nu) \tag{3.9}$$

$$\mathbf{g} = \frac{1}{c} \int d\nu \int_{4\pi} d\Omega \mathbf{n} (j_\nu - k_\nu I_\nu) \tag{3.10}$$

The form of the emissivity j_ν and absorptivity $-k_\nu I_\nu$ in a perfect black body would be that of a Planck spectrum. This is not an accurate picture of what happens at high temperatures, particularly when considering atomic excitation and de-excitation in the material and so a frequency resolved opacity is required. HYADES uses a multi-group diffusion model,[1] consisting of discrete energy bands of photons which are affected by the medium they are travelling through by an opacity calculated from the relative abundance of elements in the plasma and their ionisation states.

3.3.2.3 Laser-Plasma Interactions

Inverse bremsstrahlung radiation is thought to be the dominant absorption mechanism for shorter wavelength ($\lambda < \mu m$) laser absorption for longer pulse lasers (ns to several hundred ps).[95] In a high-contrast short-pulse laser scenario, where there is very little ASE pre-pulse incident on the target, this is unlikely to be the dominant

method of absorption.[65] However, with most short-pulse lasers having a significant pre-pulse, and so a large pre-plasma into which the laser can deposit its energy, the significance of the absorption process can vary widely.[65] HYADES implements several energy source models for describing an incident laser beam or other driver. The two relevant models for this study are the ray-tracing inverse-bremsstrahlung model and the Helmholtz wave solver. The first model uses a ray-tracing method where energy is deposited using an inverse bremsstrahlung model until the ray reaches the critical density or turning point for non-normal incidence where it is deposited using a resonance absorption model[1] (as described in section 2.2.2). The absorption coefficient, α, used by HYADES in this method is as follows:

$$\alpha = \mathrm{X}\frac{256\pi^{5/2}e^6}{3ch^3}\frac{\left\langle n_i(Z^*)^2\right\rangle}{\omega_l^2\sqrt{1-\frac{\omega_{pe}^2}{\omega_l^2}}}F_{1/2}\left(\frac{\mu}{kT_e}\right)\ln\Lambda_{ei}[\mathrm{cm}^{-1}] \tag{3.11}$$

where X is a user defined multiplier (the default being X=1, which is used here), $F_{1/2}$ is a Fermi-Dirac integral of order 1/2, ω_l is the laser frequency, ω_{pe} is the plasma frequency, Λ_{ei} is the electron-ion collision frequency, and μ is the chemical potential. Which is similar to the free-free absorption coefficient found in other literature[85,126] with the addition of degeneracy being taken into account via the Fermi-Dirac integral which in the non-degenerate limit simplifies $F_{1/2} \to \frac{\sqrt{\pi}n_e}{4}\left(\frac{h^2}{2\pi m_e kT_e}\right)^{3/2}$. Hyades also takes into account stimulated emission in dense plasmas via an extra term in the absorption coefficient:[127]

$$\alpha' = \alpha\left(1-e^{-\frac{\hbar\omega_l}{kT_e}}\right) \tag{3.12}$$

There is an additional factor to take into account, that HYADES does not calculate, which is the blocking factor.[128] At high densities the occupation of free states can have an effect on radiative absorption and emission for both free-free processes and free-bound processes. If the absorption of a photon by an electron were to promote

it to an already fully occupied state this absorption cannot occur due to Fermi-exclusion, the same can be said for the emission of a photon by an electron. The ratio of the absorption coefficient with the blocking factor taken into account to that without it ($\alpha_{BF}/\alpha = R_{BF}$) is given by:

$$R_{BF} = \exp\left(-\frac{\mu}{kT_e}\right)\exp\left(\frac{\hbar\omega}{kT_e}\right)I_{int} \tag{3.13}$$

where

$$I_{int} = \int_{\frac{\hbar\omega}{kT_e}}^{\infty}\left(\frac{1}{\exp\left(-\frac{\mu-E}{kT}\right)+1}\right)\left(1-\frac{1}{\exp\left(-\frac{\mu-(E-\hbar\omega)}{kT_e}\right)+1}\right)d\left(\frac{E}{kT_e}\right) \tag{3.14}$$

For situations where there are steep gradients around the critical density or no under-dense plasma then the reflectivity of the plasma with respect to the laser radiation can be modelled with the use of a Helmholtz solver.[65] The Helmholtz equations for the electric and magnetic fields are respectively:

$$\frac{\partial^2 E_z}{\partial x^2} + k_0^2(\epsilon - sin^2\theta)E_z = 0 \tag{3.15}$$

$$\frac{\partial^2 B_z}{\partial x^2} - \frac{1}{\epsilon}\frac{\partial \epsilon}{\partial x}\frac{\partial B_z}{\partial x} + k_0^2(\epsilon - \sin^2\theta)B_z = 0 \tag{3.16}$$

where ϵ is the dielectric of the medium, k_0 is the wave number of the incoming laser pulse, $\mathbf{E}$ and $\mathbf{B}$ are the electric and magnetic fields respectively and the angle θ is the angle of the incident laser pulse to the density gradient. The dielectric value is calculated as:

$$\epsilon(x) = 1 - \frac{n_e(x)}{n_{crit}}\left(\frac{1}{1+i\frac{\nu_{ei}}{\omega}}\right) \tag{3.17}$$

with $n_e()$ being the electron density; n_{crit} is the critical density of the incoming laser pulse; with ω being the laser wavelength; and ν_{ei} is the electron-ion collision frequency which is a function of the electron density and the local electron temperature. While Helmholtz solvers can be used on steep gradient pre-plasmas they

also calculate a deeper penetration of a laser pulse into shallower gradients when compared to the inverse bremsstrahlung model.

3.3.2.4 Ionisation

HYADES supports several ionisation models. The ionisation model used in this study is the average atom model,[129] which considers a single average atom which may have fractional electrons bound to each ionisation level. A local thermodynamic equilibrium (LTE) model is not unreasonable given that the initial state of the target is optically thick, i.e. it is opaque to its own emission.[65]

3.3.2.5 Geometry

HYADES can use symmetries to emulate a particular 3D geometry. It can use slab geometry, which just simulates a line out of a planar slab of material; spherical geometries can also be used for capsule compression simulations and simulate a line-out along the radial direction; likewise cylindrical geometries use the radial direction and assume symmetry along the axis, see Fig.3.6. While 1D codes cannot account for 2 or 3D effects like the Richtmeyer-Meshkov or Rayleigh-Taylor instabilities, they tend to include more detailed physical modelling than 2D or 3D codes.

3.3.3 Hybrid Modelling

PIC codes are very computationally intensive to run when large systems of particles are required. In addition to this, over large numbers of timesteps the can become numerically unstable. In systems where there is a population of very hot (MeV) particles traversing a region of cold plasma a hybrid model can be employed. This type of model works in a similar way to a PIC code, a system of particles with a continuous phase-space is evolved alongside electric and magnetic fields on a grid. The values at the grid positions however, are also evolved (after a set number of

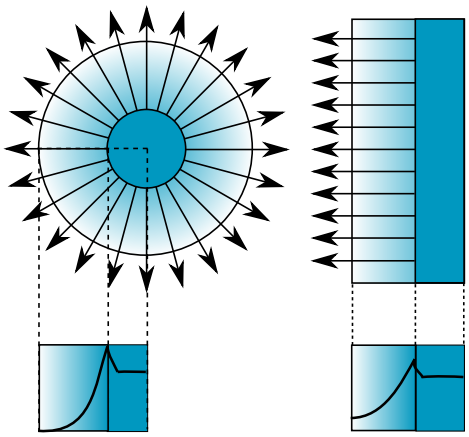

Figure 3.6: 1D fluid codes like HYADES can approximate 3D solutions using symmetry arguments, planar geometries are used for simulations in Chapter 3 and both planar and spherical are used for comparison in Chapter 4, although a cylindrical geometry is also available.

timesteps) according to a fluid calculation. So that in addition to a fast-moving particle based foreground, a slower moving fluid based background is used. This type of calculation can be used for a number of situations including the transport of fast-electrons through a solid target. The fast-electrons, with energies in the MeV range and so will have a large Debye length, can be modelled with a PIC calculation with the added advantage that the use of a thermal fluid background electron population eliminates the possibility of finite-grid instability. The background fluid can be calculated either using a VFP code (as in ref 130) or using a fixed background fluid.[131]

As described earlier (see equation 2.6), electrons at the critical density of a laser-plasma interaction can be accelerated to large velocities: hundreds of keV to MeV energies with high laser intensities. The heating of the bulk of the target is not likely to be nearly so immediate and so a situation occurs where there is a non-Maxwellian distribution of electrons within the bulk of the target.

The hybrid model splits the bulk electron population into two: a cold background population, with a temperature T_{back}, and density n_{back}; and a hot (or fast as

their velocity is highly directional) population, with a temperature T_f and density n_f. Noting that $T_{back} << T_f$ and $n_{back} >> n_f$, a fluid model can be used to evolve the background population while the hot population dynamics are simulated using a kinetic model.

An example of a hybrid code is ANTHEM.[132] This code consists of two components a particle component and a fluid component. Whilst the fluid component can be used to model the highly collisional denser plasma regions where a classical hydrodynamic model might normally be used, the particle component can model the less dense, lower collisionality, regions of the target, e.g. a coronal region. In this simulation the Courant condition, where the time-step $\Delta t \leq {}^{\Delta x}/_{v_h}$ and v_h is the speed of the fastest electrons in the thermal background fluid, is of particular importance in correctly calculating the thermal conduction of the background fluid.

In the hot-particle mode, two to ten particles are emitted per source cell per time step into an emission distribution which can be set by the user. These particles are then evolved according to an implicit PIC formalism coupled with the fluid background at the grid points. The time-step constraint of this simulation is governed either by the Courant condition described above or the implicit PIC condition $\omega_{pe}\Delta t < 1$, dependant on the smallest of these values. A drag force on the particles is simulated using a constant coefficient proportional to $1/v^2$, where v is the speed of the particle. The emitted electrons then deposit their energy into the background electron fluid as they are slowed. If the energy of the emitted particle drops below the local thermal energy the particle is reabsorbed. Kinetic electrons are scattered by ions, e-e scattering is taken into account by increasing the ion scattering by a factor of $\frac{1+Z}{Z}$, the scattering events are either calculated using an implicit[133] or explicit[134] scattering model.

The LSP PIC-Hybrid code,[115,116] described earlier, permits charged particles to be modelled using either a kinetic or fluid description; employing a nonrelativistic inertial fluid model for the lower energy particles. This type of simulation allows for

the simulation of large lengthscales (hundreds of microns) and tens of pico-second time scales. The equation of motion for a high energy particles switches to a fluid-like equation of motion if its kinetic energy is less than the thermal energy of the ambient dense fluid and $\omega_{pe}\Delta t > 1$. The equation of motion of the fluid particles is identical to the kinetic equation except for the scattering terms. The kinetic collisional scattering terms are replaced with a pressure gradient force term to model intra-species collisions, and a frictional force to model inter-species collisions. Terms for Ohmic heating and and thermal conductivity are also included.

Some considerable progress has been made in understanding a range of laser-target physics problems by coupling the LSP implicit PIC model with other codes. This has the effect of extending the range of phenomena that are possible to model, as longer term hydro-dynamic effects can be effectively modelled by the radiation-hydrodynamics codes, with LSP handling the somewhat shorter regimes including phenomena like fast-electron transport. For example the modelling of both the long and short timescale laser-target interaction events in a study of a cone-guided fast-ignition experiments has been performed using the radiation-hydrodynamics code FLASH,[135] followed by the LSP code.[136] The DRACO 2D axis-symmetric hydrodynamics code[137,138] has also been integrated with LSP in order to simulate the effect of the generation and deposition of fast-electrons in a fast-ignition scheme.[139]

Zephyros, uses the hybrid approximation with a PIC treatment of the fast electrons and a fixed background fluid for the cold electron background. The background fluid is subject to a similar treatment to the rigid beam model.[140] The rigid beam model requires two equations: Ohmic heating of a background electron fluid (with J_f substituted for J_{back}), which is given by:

$$\frac{dT_{back}}{dt} = \frac{J_f^2 \eta(T_{back})}{\frac{3}{2} n_e(T_{back}) e} \tag{3.18}$$

where J_f is the current density calculated from injected fast electrons; $n_e(T)$ is the

cold background electron density, which is usually calculated from an ionisation or electron equation of state model; and $\eta(T)$, which is a model for the resistivity of the background electron fluid. The magnetic field is calculated using Ampere's law ignoring the displacement current:

$$\frac{dB}{dt} = -\nabla \cdot (\eta(T_{back})\mathbf{J_f}(\mathbf{r})) \tag{3.19}$$

Whilst the rigid beam model uses an arbitrary fast electron current density profile $J_f(r)$, the PIC model allows electrons to be injected into a grid, while the background co-evolves, with J_f calculated from electron trajectories. It is important to note that the ion background is completely fixed in this case, and that the electron fluid is also fixed in space, therefore no simulation of shocks or any other fluid type behaviour is possible. The hybrid scheme utilised in Zephyros allows for extremely efficient simulation of fast electron dynamics within solid targets, which in turn allows for exploration of novel target designs for fast-electron transport through solid targets.

Chapter 4

Doppler-shift Spectroscopy and Shockwave-Velocity Measurements in a High-Contrast Laser System

4.1 Introduction

The emphasis of this chapter is on effective modelling of short-pulse laser-plasma interactions (t_{pulse} ~30 fs) using a radiation-hydrodynamics and particle-in-cell kinetic framework. Towards this end a pump and 3ω probe experiment using an ultra-intense (10^{18} Wcm^{-2}) laser pulse with a relatively high contrast of 10^7, is described briefly. This is followed with a more extensive description of the modelling process required to understand the possible phenomena occurring in and around the critical-density region of the target. The modelling process is split into several parts. There is an initial discussion of a radiation hydrodynamics approach, using HYADES, which, while providing some degree of qualitative agreement with the experiment, cannot adequately describe the absorption processes involved in a short-pulse laser-plasma interaction. This is followed by results from a PIC code, EPOCH, the input of EPOCH being initialised using the previously described HYADES code

just before the main pulse. This is so that the short-pulse interaction can be modelled using a kinetic approach. The kinetic simulation approach is concluded with a description of how another simple Lagrangian hydrodynamics code can be used to compare the coupled PIC/radiation-hydrodynamics approach to an experiment. To conclude this chapter some of the possible modifications that are required to improve the coupled PIC/radiation-hydrodynamics method in this regime, that would enable the production of a more physically accurate picture are discussed.

4.2 100 TW Pump-3ω-Probe Experiment

The 100TW laser system at TIFR is used to perform a pump-probe Doppler spectroscopy experiment, where a small amount of the main pump energy is split off into a probe. The p-polarised pump pulse is focused on to a polished thick BK7 crown glass target by an $f/3$ off-axis parabolic mirror at an angle of incidence of 40°, a discussion of the geometry and set-up of the experiment is found in section 3.2.

The probe is frequency-tripled, delayed via a delay stage, and reflected at near-normal incidence onto the front surface of the target. The spectrum of this probe is then measured and a Doppler shift calculated which can then be used to infer a velocity of the probe's critical surface. Prior to the experiments described in this thesis only frequency doubling has been used[71] to study behaviour at lower densities in this way.

4.2.1 Main Pump Parameters

The larger 100 TW laser system at TIFR can provide a pulse of temporal width t_{laser} = 30 fs, and λ_{pump} = 800 nm using a spectral width $\Delta\lambda_{pump}$ = 34 nm. The 100 TW laser is reduced to approximately 20% of maximum, for comparison with the 20 TW experiment presented later, and focused to a spot size with a FWHM of 14 μm, and with a peak intensity of $I_{pump} \sim 9.5 \times 10^{17}$ Wcm^{-2}. The temporal

intensity profile of the laser pulse is characterised with a 3rd-order cross-correlator (SEQUOIA) the results of which are shown in Fig. 4.1. If the contrast is estimated as a constant 10^7 for the 500 ps duration the amount of energy deposited by the pedestal works out to approximately 0.17% of that delivered by the main high intensity pulse. At the 20% reduced level the laser system provides an energy of ~ 600 mJ per shot, with a shot-to-shot fluctuation of ~ 6%.

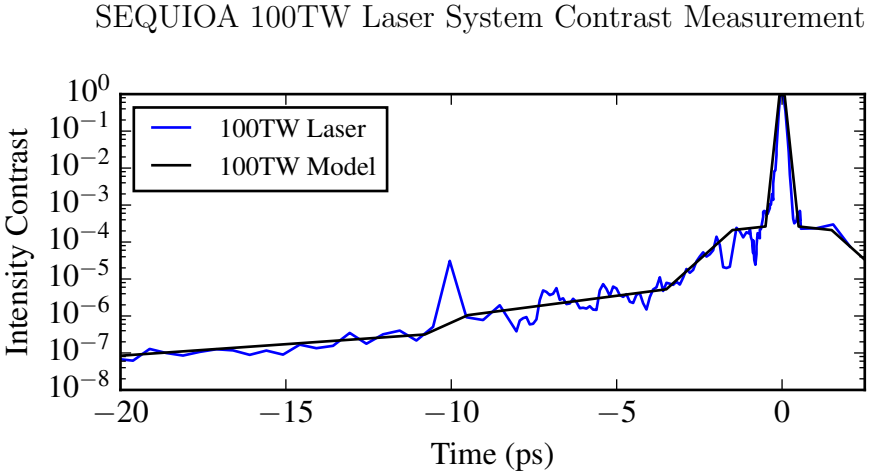

Figure 4.1: Plot of the laser contrast measurements from 3rd order cross correlator (blue), and piece-wise linear envelope used in HYADES input to remove high frequency noise (black) between t = −20 ps to t = 2 ps. The peak at t=-10 ps is ignored as this is due to a reflection in the SEQUOIA cross-correletor. The full pre-pulse is ~ 500 ps long, with the intensity (measured again with the cross-correlator) during this time $I_p \sim 10^{-13}$ Wcm^{-2}.

4.2.2 Frequency Tripled Probe Set-up

To obtain a probe-pulse that can be accurately delayed with respect to the main pulse, a small amount of energy is diverted with a beam splitter and then converted to the third harmonic ($\lambda_{pump}/3 = \lambda_{probe} \simeq 266$ nm) using a pair of Barium Borate crystals. The probe-pulse has a much narrower bandwidth on leaving the crystal than the pump with a $\Delta\lambda = 0.76 \pm 0.02$ nm, $\Delta\lambda$ being defined here as the σ of a Gaussian curve fitted to the probe pulse spectrum measurement. The probe wavelength, λ_{probe}, has an associated critical density of $n_{pcrit} = 1.6 \times 10^{22}\ cm^{-3}$. It is worth

noting that $n_{p,crit} \sim 9n_{crit}$. The probe-pulse is focused to a diameter of 50 μm at a near normal $3-5^{\circ}$ angle of incidence. The large focal diameter results in a probe intensity of $\sim 10^{10}$ Wcm^{-2}. Spectral measurements are taken with a spectrometer (Avaspec-3648-USB2) which has a spectral resolution of 0.02 nm and a peak sensitivity of 260 nm. The spectrometer was set to data acquisition mode in which 20 spectra at the same temporal delay are averaged to obtain a single spectrum.

4.2.3 Results

The averaged Doppler shift of the probe vs. probe delay time is plotted in Fig.4.2a, and the conversion to a velocity using $v = 0.5c\frac{\delta\lambda}{\lambda}$is plotted in Fig.4.2b. The error-bars on the results are statistical error bars of $\pm\sigma$, where σ is the fitting error from fitting a guassian envelope to the measured spectra. Whilst the error-bars are significant the results show a clear trend.

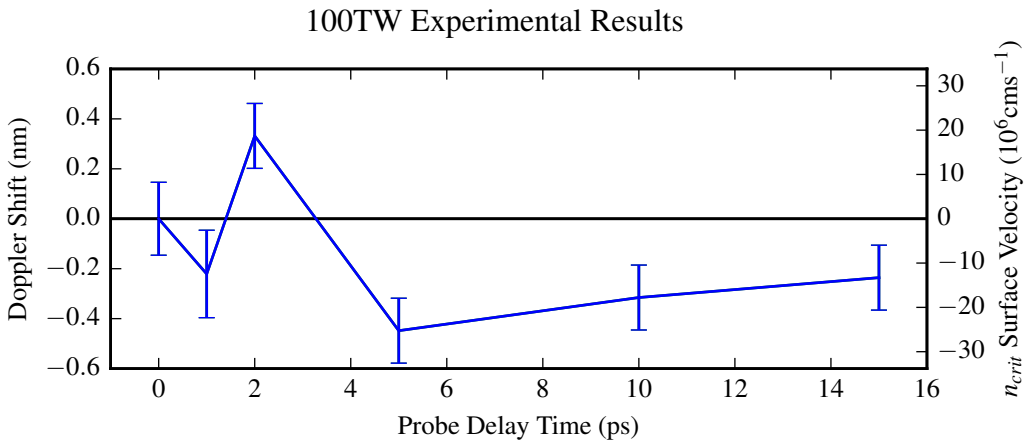

Figure 4.2: Plot of the shot averaged Doppler shift, a blue shift would indicate an object travelling towards the spectrometer (a reduction in λ). The calculated critical surface velocity (right hand axis), here the positive velocity direction was chosen so that it represents material flowing towards the target surface and away from the spectrometer, while material ablating away from the target surface would have a negative velocity. The fitting error on the resulting measured spectrum is quoted as the error on an individual reading.

The motion of the critical surface shown in Fig.4.2b shows an initial outward expansion from the target front surface (up to $t = 1$ ps), followed by an inward motion

(at $t = 2$ ps) and then an expansion away from the front surface again ($t > 2$ ps). The first section (up to $t = 1$ ps) can be interpreted as an initial thermal expansion of the target from pre-pulse heating. This is followed (at $t = 2$ ps) by the motion of a compressive shock-like perturbation travelling through the critical surface. Which is then finally followed ($t > 2$ ps) by thermal expansion after the shock front has passed.

4.3 Radiation-Hydrodynamics Modelling

In order for the radiation-hydrodynamics models to be able to reproduce the results seen in the Doppler spectroscopy experiments a number of things have to be correctly calculated or described: the EOS of the material in the experiment; the energy deposition from the laser; and the transport of that energy through the target. Each of these aspects incorporates a substantial amount of physics. Whilst an equation of state for fused silica is included in the SESAME library, and this should suffice given the degree of accuracy required, the other aspects require attention.

Given a spot size of 14 μm and a measured velocity of $\sim 10^6$ cms^{-1} any shock like disturbance could travel around ~ 300nm in the measurement timescale (~ 30ps). These measurements were taken after the arrival of the main pulse and in a relatively dense region of the target/pre-plasma, the comparison of the size of the spot to the possible movement of the critical surface suggests that a 1-D slab like geometry may be a reasonable approximation to make, at least with regard to the dynamics of the plasma close to the critical surface. In the ablated under-dense region higher dimensional effects, such as lateral expansion, may be relevant, but as they are travelling away from the region of interest at supersonic velocities they are unlikely to be of importance to the dynamics of any disturbance or shock-like behaviour in the dense part of the target.

4.3.1 Initial Code Setup

To save computation time only the first 500μm depth of the target is simulated, which is expected to fully encompass the region in which the laser-plasma interaction dynamics occur. The mesh is set up so that there are more cells at the beginning of the simulation than at the end, so that the laser-interaction region is well modelled and cell expansion is mitigated to some extent by the initially small size of those cells. In order to make sure that there is sufficient resolution near the laser-interaction region a mesh with varied lengthed cells is constructed with each cell length l_i having a length of $l_i = r * l_{i-1}$, with r being a constant ratio, so that even though a large depth of the target is simulated, the initial spatial resolution of the grid is highest in the region where the grid will experience the greatest expansion (see Fig.4.3).

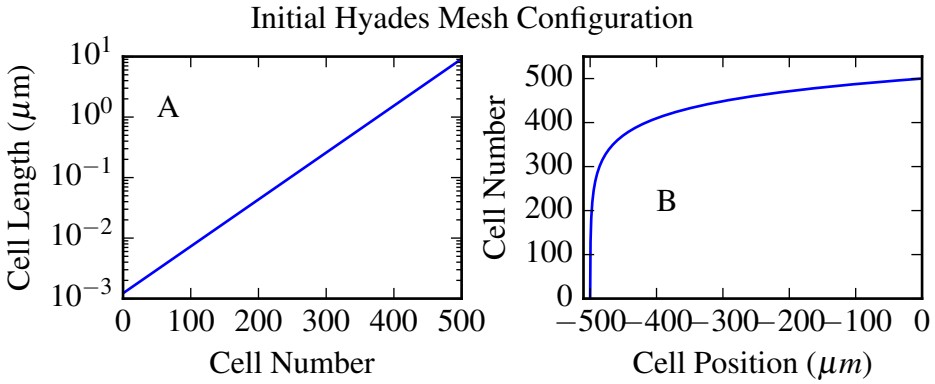

Figure 4.3: The mesh used for the HYADES simulations. The ratio r = 1.018 is sufficient to prevent the mesh around the critical density from evolving in such a way that the laser energy is deposited in only a few cells located around the critical density. Whilst the cells at the front surface of the target are small, they will expand the most later in time.

The material for the BK7 glass is modelled as a fluid with the properties $\hat{Z}$ = 10.00, $\hat{A}$ = 20.028, ρ = 2.65 gcm^{-3}. An equation of state from the SESAME library for fused Silica (record 7386, which has been compared to experimental measurements up to the MBar pressure range[141,142]) is also used. To model ionisation an LTE average atom model is used.

The energy transport through the target is of key importance. The multi-group radiation package is used with 100 photon groups with the initial lower energy box

edge set at 10^{-3} eV with higher energy box edges from 0.1 eV up-to 10^4 eV, as shown in Fig.4.4, whilst this does not give a high degree of resolution across such a large range of energies it provides a reasonable compromise between resolving the behaviour accurately and computational time. The results from a sample configuration were tested against an identical simulation with 150 photon groups, though with no significant difference in temperature or pre-plasma extent.

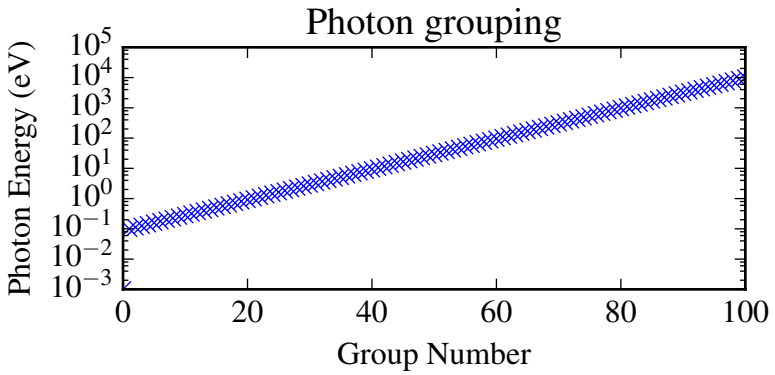

Figure 4.4: Photon energy groups used in HYADES simulations, plotted is the photon energy at each group edge, plotted by bin number (zero corresponding to the lower bound energy of the first box).

Thermal conduction is of critical importance to the formation of a shock in a narrow pre-plasma, and to work out whether a flux limited model is required the ratio of the electron-ion mean-free-path λ_{ei} can be compared to an assumed temperature scale length.[66] The value for λ_{ei} can be estimated by using the ratio of the electron-ion collision frequency (see eqn.2.8) to the electron thermal velocity, given as $v_{th} = (k_b T_e/m_e)^{1/2}$. Using an estimate for the temperature ($T_e \sim 100$ eV) and a range of plausible temperature length-scales ($L_T \sim 10$ μm) around the deposition region (with a density of $n_{crit} = 1.7 \times 10^{22}$ cm^{-3}) a ratio of:

$$\frac{\lambda_{ei}}{L_T} \sim 10^4 \tag{4.1}$$

is calculated. Given that the electron-ion mean-free-path is so much longer than the temperature scale length, even at relatively conservative values, the Spitzer-Harm

model breaks down and so the flux-limited model available in HYADES is required. Unfortunately such analysis does not give any insight as to what value flux limiter should be used, and so a range of values between 0.3 and 0.05 is used here. This range is based on a number of studies that support a range higher than 0.3 (as in refs. 143–145) and as low as or lower than 0.05 (as in refs. 146,147) and a significant range in between (as in ref. 148). Interestingly it has been suggested that a match to a lower value of the flux-limiter may be as a result of higher dimensional effects due to a tight focus,[149] or simply due to using a 1D hydrodynamic model as the later studies tended to use a match to 2D hydrodynamic modelling.[143–145]

Both the Helmholtz absorption package and the Fresnel/Inverse Bremsstrahlung packages are used for comparison, these models and their implementation are discussed in section 3.3.2.3. These packages are set up with laser parameters of λ = 800 nm, θ = 0.698 rad = 40° along with plane polarisation, which is consistent with the experimental setup.

4.3.2 HYADES Calculation Results

It is worth comparing two of the models used for laser absorption in HYADES: namely the Fresnel reflection model, which uses inverse bremsstrahlung absorption up to the critical density, where the Fresnel reflectivity is then calculated; and the Helmholtz solver, which uses the plasma dielectric to calculate the reflectivity/absorptivity of the plasma at each point up to the critical density. The results of simulations using flux-limiters of 0.3, 0.1 and 0.05 are shown in Fig.4.5 for both models. From these results it is clear that the flux-limiter of 0.05 for both models gives the closest match to the experimental results. The match to the lower flux-limiter value of 0.05 is in agreement with earlier studies,[146,147] though this may be a result of calculating in 1D. However when the results from the two models are compared at the same flux-limiter values (as shown in the bottom right of Fig.4.5)

it is clear that they are not in close agreement with each other.

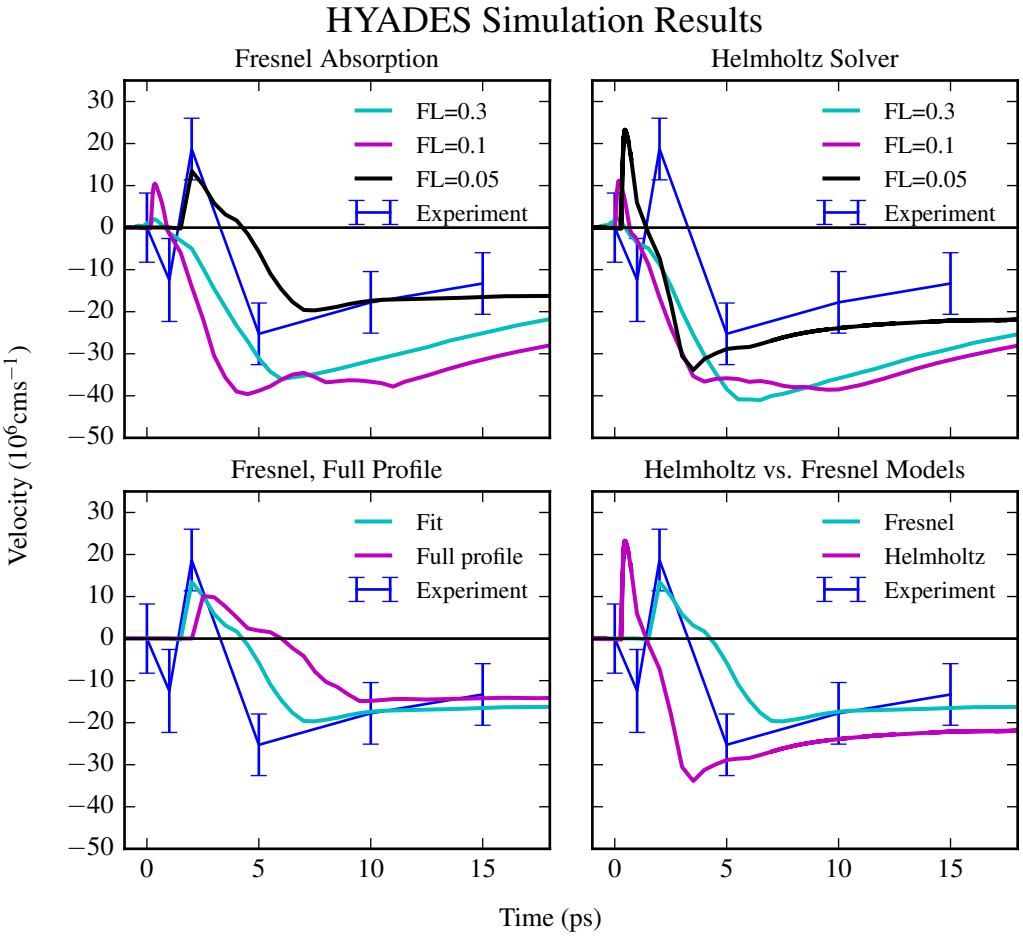

Figure 4.5: Top left: Fresnel reflectivity results for flux-limiter values of 0.3, 0.1 and 0.05. Top right: Results from the Helmholtz reflectivity solver using the same flux-limiter values. Bottom left: Results obtained using the Fresnel reflectivity model, a flux-limiter of 0.05 but testing the use of the piece-wise fit vs. the full intensity profile. Bottom right: Over plotting of Fresnel and Helmholtz models at a flux-limiter of 0.05 for comparison. Time t = 0ps corresponds to the time at which the main pulse reaches the target in the experimental setup, and the time at which the intensity reaches peak in the HYADES simulations.

Neither model shows the initial positive expansion towards the laser at t = 1ps, however in the simulations with smaller flux-limiter values there is some agreement with the experimental values displayed in Fig.4.5. The simulations with higher flux-limiters did not produce the shock-like perturbations from the main pulse, and so no inwards compression, or negative velocity, are observed. The timing of the arrival of the shock at the probe critical surface also appears to coincide with the experimental

results almost exactly in the case of the Fresnel reflectivity model.

The electron density outputs from HYADES (Fig.4.6) show two shocks, the first from the effect of the pre-pulse (shown in Fig.4.6a), and a second, later shock formed from the energy deposited by the main pulse (Fig.4.6b-d). The pre-pulse shock has a compression ratio of ~ 4, whilst the compression due to the main pulse appears to grow from ~ 2 at t = 0.1 ps, to nearer ~ 4 at t = 2.0 ps. At around t = 3 ps the two shocks coalesce into a larger shock with a much higher compression ratio, closer to ~ 10, (see Fig.4.6e-f).

Referring back to the experimental results in Fig.4.2 and to the electron density output in Fig.4.6, the hypothesis described earlier can be tested. To aid the description the critical density for the main pulse (λ_m = 800 nm, $n_{c,m} \simeq 1.7 \times 10^{21}\text{cm}^{-3}$) and the critical density of the probe pulse (λ_p = 266 nm,$n_{c,p} \simeq 1.6 \times 10^{22}\text{cm}^{-3}$) have been added to Fig.4.6. The Doppler shifting of the probe pulse is likely to be caused by the motion of the critical density-surface that the probe reflects off. The critical density of the probe is marked on Fig.4.6.

At $t < 2$ ps there is some disagreement between the two laser deposition models in HYADES, which both disagree with the experiment; the Doppler shift of the probe pulse likely coming from a region behind the shock produced from the pre-pulse, which is a region that is expanding towards the viewer. At $t \simeq 2$ ps the Doppler shift of the probe pulse comes from a region near the apex of the shock created by the main pulse and is seen travelling away from the viewer, though when using the Helmholtz absorption model the shock actually arrives slightly earlier at $t \sim 1$ ps. At $t > 2$ ps the Doppler shift of the probe pulse comes from a region of material behind the coalesced shock and is viewed as expanding towards the viewer.

4.4 Kinetic Modelling

The EPOCH particle-in-cell code is used here to check the deposition of the final high intensity laser pulse. HYADES is not designed to model short pulse interactions. In spite of this the HYADES simulation results show some agreement with the experimental values. However the absorption mechanism responsible for the experimental results is likely to be quite different to the inverse bremsstrahlung model

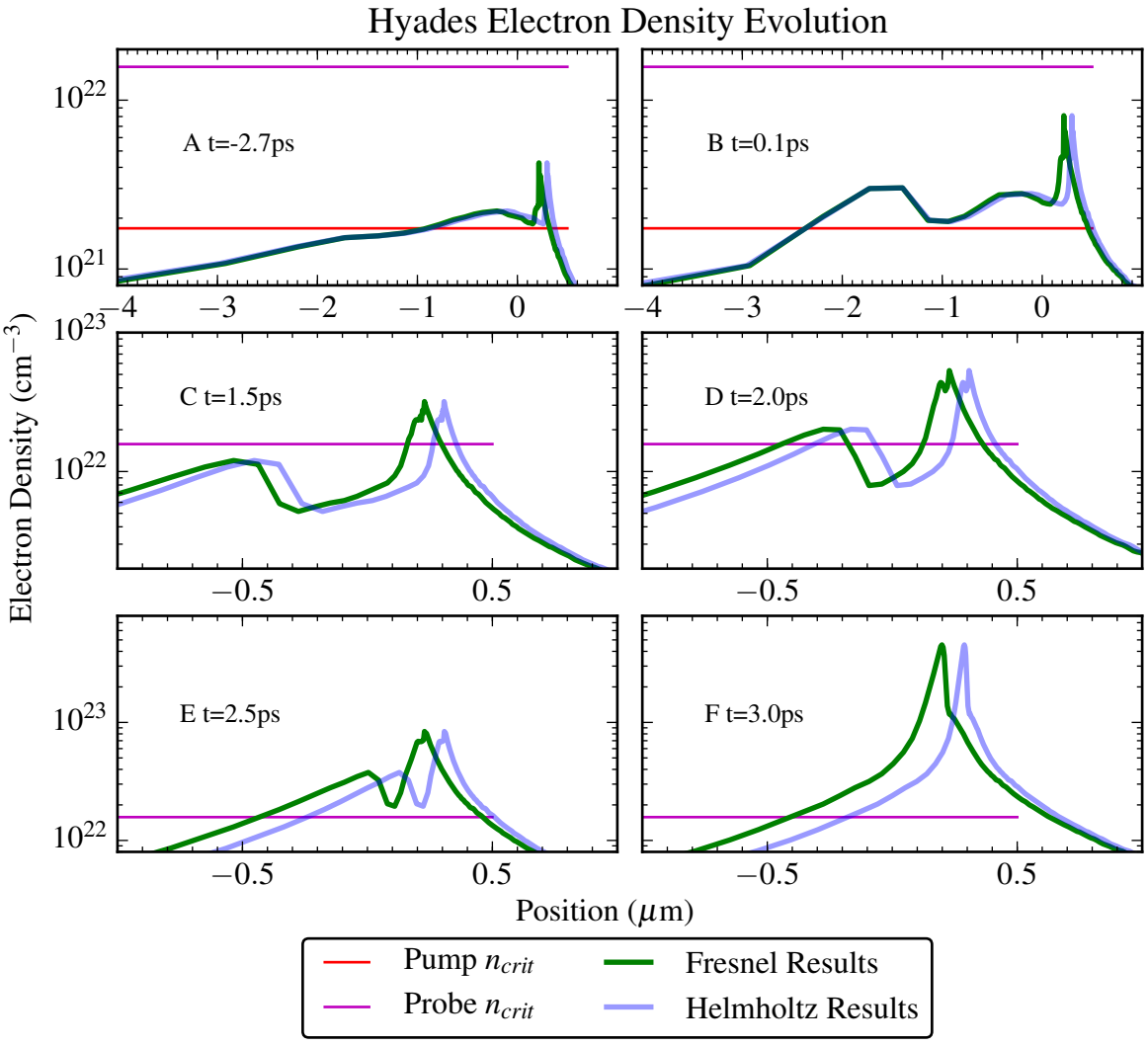

Figure 4.6: Snapshots of electron density at various times shortly after the arrival of the main pulse. Plots are from HYADES simulations using both Fresnel and Helmholtz results and a flux-limiter of 0.05. Time $t = 0$ ps is set to corresponds to mid-way through the main pulse (i.e. at peak intensity).

implemented in HYADES.

To initialise EPOCH a set of hydrodynamic variables are taken from a HYADES simulation run at a point in time ~ 30 fs before the onset of the main pulse. The shock formed by the main pulse interaction is located close to the critical density, however there may be other resonant processes that could occur at slightly lower densities and so a region of around 70 μm is chosen as the simulation box.

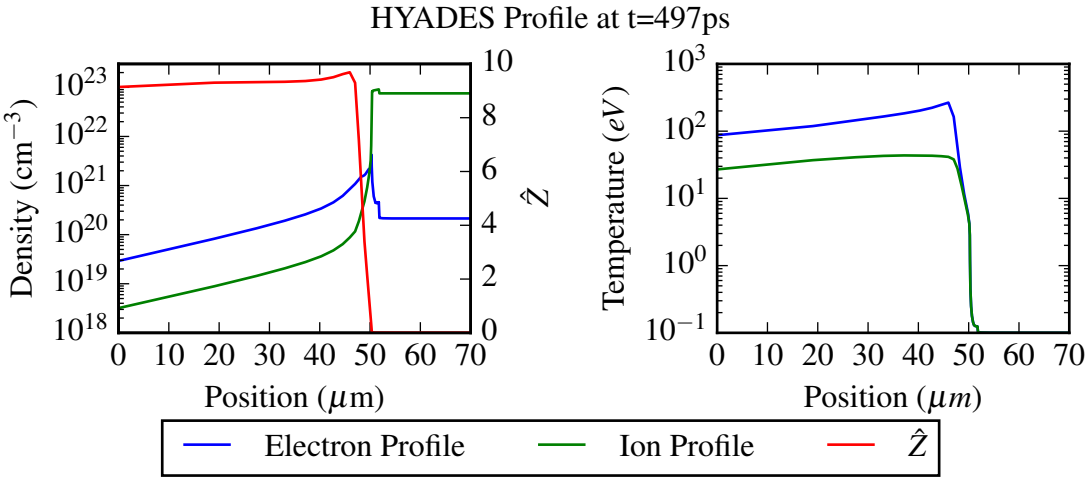

Figure 4.7: Plots of density n_e and n_i and ionisation $\hat{Z}$ on the left, and temperature (T_e and T_i) on the right. Profiles are taken from a HYADES run using a Fresnel laser solver and using a flux-limiter value of 0.05.

Fig.4.7 shows the profiles obtained from the HYADES simulation run using a Fresnel laser absorption model along with a flux-limiter value of 0.05. The choice of picking the Fresnel model over the Helmholtz solver profiles is not significant as the profiles are very similar except for a slight x-axis offset as can be seen in Fig. 4.6. The flux-limiter value however appears to bear some significance and so the simulation outputs obtained using a value of 0.05 is chosen as the earlier HYADES outputs appear to match experimental results far better than those obtained with a larger value. There are two input profiles described, which will be referred to as profile 1, which uses a HYADES electron density to initialise EPOCH, and profile 2 which uses a HYADES ion density to initialise EPOCH.

4.4.1 EPOCH Setup Profile 1; Ion Density Profile

To initialise EPOCH the output from HYADES, at a time just before the main pulse, is used to generate the electron and ion density, and temperature profiles. Several simplifications are needed in order to make this possible. The most important region is around the critical density where the gradients in T_e, $\hat{Z}$, and n_e are extremely steep. Creating a finite but steep gradient in $\hat{Z}$ in a PIC setting requires a large number of different ion species, each with different density (and possibly temperature) profile. Setting up such a set of density and temperature profiles from an ion averaged $\hat{Z}$ model (such as the average atom or Thomas-Fermi models described earlier) would be very challenging to match to the HYADES input. The initial profile set up uses a profile divided into two separate physical sections. The first part comprises of the expanded pre-plasma leading up to the critical density and the compressed shock front after the critical density (this region is coloured blue in Fig.4.8), the second part consists of cold bulk target material.

The first region is fully ionised and has an electron density that follows the original HYADES ion density, which is treated as fully ionised so that $n_{e,PIC} = n_i Z_i$, where i is the average ion species in HYADES. The ion density is then set so that $\sum_s Z_s n_s = n_e$. The BK7 glass target consists of a variety of materials, however the most common by quantity are oxygen ($\sim 60\%$) and silicon ($\sim 30\%$) ions, and so as an approximation just two ion species are set at $n_O = 65\%\hat{Z}n_e$ and $n_{Si} = 35\%\hat{Z}n_e$. This ensures that the overall $\hat{Z} = 10.1$ is consistent with the maximum average $\hat{Z}$ of the composite material.

The second region behind the fully ionised region will be set to a step density profile so that $n_{i,cold} = 10^{22}\text{cm}^{-3}$ and again with $n_{Si} = 0.65n_i$ and $n_O = 0.35n_i$, however here both species will be singly ionised giving a $\hat{Z} = 1$ and $n_e = n_{Si} + n_O$.

To attempt to limit the effects of self-heating and an inaccurate deposition profile, a grid is set up so that $dx = 5$ nm, the initial temperature is set to zero for

both ions and electrons. The grid set up above will resolve the Debye length of a plasma with an electron temperature of $T_e \sim 5 \times 10^3$ at a density of 10^{22}cm^{-3}. With the current smoothing routines enabled and with EPOCH compiled using the 3rd-order spline particle-shape, this should sufficient to minimise the chance of significant numerical self-heating. The number of particles per cell can then be set to $N = 10^4$ to ensure reasonable statistics throughout the domain without the simulation being overly expensive. The output of this code is then checked for converging results by comparing the output in T_e to a simulation with exactly half the number of particles per cell and double the cell length. Whilst the low-density region is convergent, (a difference of less than 10% in the temperature profile is observed), in the higher density region ($n_i > 5 \times 10^{23}$ cm^{-3}) the ion temperature profile rises to approximately 10^3 eV prior to the arrival of the laser pulse. This heating in the higher density region is likely due to the ion populations equilibriating with the electron population.

While EPOCH provides built-in collision routines, obtaining convergent results for high densities, whilst using these collision routines, turns out to be beyond reasonable computing requirements for this simulation. Specifically, with collisions turned on, the thermalising of the ion population observable in non-collisional codes drives a significant level of noise to the rest of the ion population making usable results unobtainable given the computing resources and time available.

The laser pulse is a plane-polarised pulse with a Gaussian envelope with of width $t_{2\sigma}$ = 18 fs (corresponding to a t_{FWHM} = 30 fs) and an intensity set to $I = 10^{18}\text{Wcm}^{-2}$. The envelope for the laser is set to $5t_\sigma$ with the peak intensity at $2.5t_\sigma$ so that the there is no sharp truncation to the pulse envelope or any high frequency noise as a result of truncation.

The ionisation profile for each ion species is taken from the NIST database, with collisional ionisation switched off. Collisional ionisation appears to impair the convergence of the code and for this reason only field ionisation is used, however this is only likely to be a problem in the cold singly-ionised dense region behind the

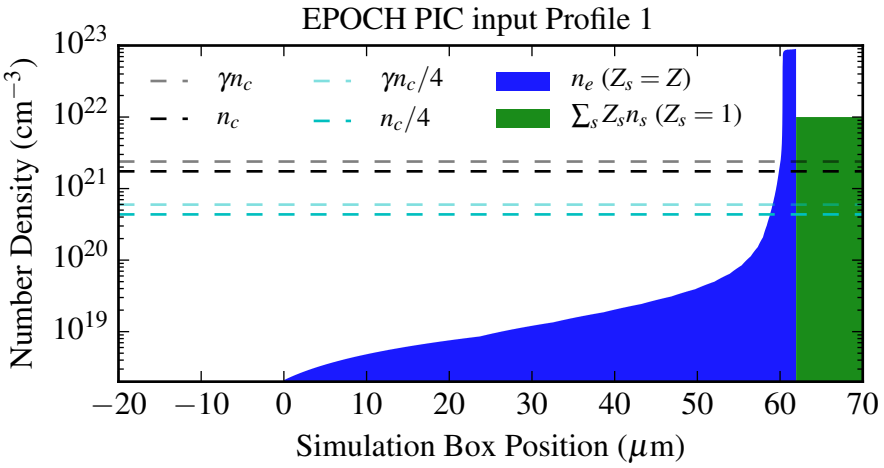

Figure 4.8: The input density profiles for the EPOCH PIC calculation consists of 5 separate profiles and can be separated into two regions. The first region is a fully ionised plasma, with an electron density (n_e) and a cold (T_i = 0 eV) ion density consisting of 65% O and 35% Si so that $\sum_s Z_s n_{i,s} = n_e$. This is calculated from a fit to the HYADES ion density output at 30fs before the main pulse. The second region consists of cold ionised plasma consisting of 65% O and 35% Si, and electrons with a density profile so that $n_e = \sum_s n_{i,s}$.

shock as it may underestimate levels of ionisation due to thermal transport.

4.4.2 EPOCH Profile 1 Results

Due to the build up of numerical errors inherent in PIC codes over long periods of time, which are unfortunately enhanced due to the use of the collision routines, and to constraints on computational time, the EPOCH code cannot be run for the 15-20ps required to produce a time series to match up with the experimental results. In order to calculate the long-term evolution of the system after the main pulse has been delivered a Lagrangian hydrodynamics code written in Python is used.

The details of the Lagrangian code are described in the previous chapter, for clarity here though a brief description is included. The code consists of a Lagrangian hydrodynamics solver using an ideal gas EOS. A density, temperature and velocity profile are used to initialise the code. No ionisation, radiation-transport, thermal conduction, or any other deviations from ideal hydrodynamics are calculated in this code. The lack of a thermal conduction model in the hydrodynamics code

used here is unlikely to present significant problems as the early time conductivity effects are expected to be dominated by hot-electron transport through the overdense material, and the thermal effect of the hot-electron heating is taken into account via the collisional heating seen in the PIC profiles. Ionisation is unlikely to contribute significantly to the hydrodynamic evolution of a shock-like perturbation at early times as the material the perturbation is travelling through is likely to be highly ionised by hot-electron heating, this hot-electron heating is also likely to dominate any radiation-transport effects, given the temperature and Z of the material.

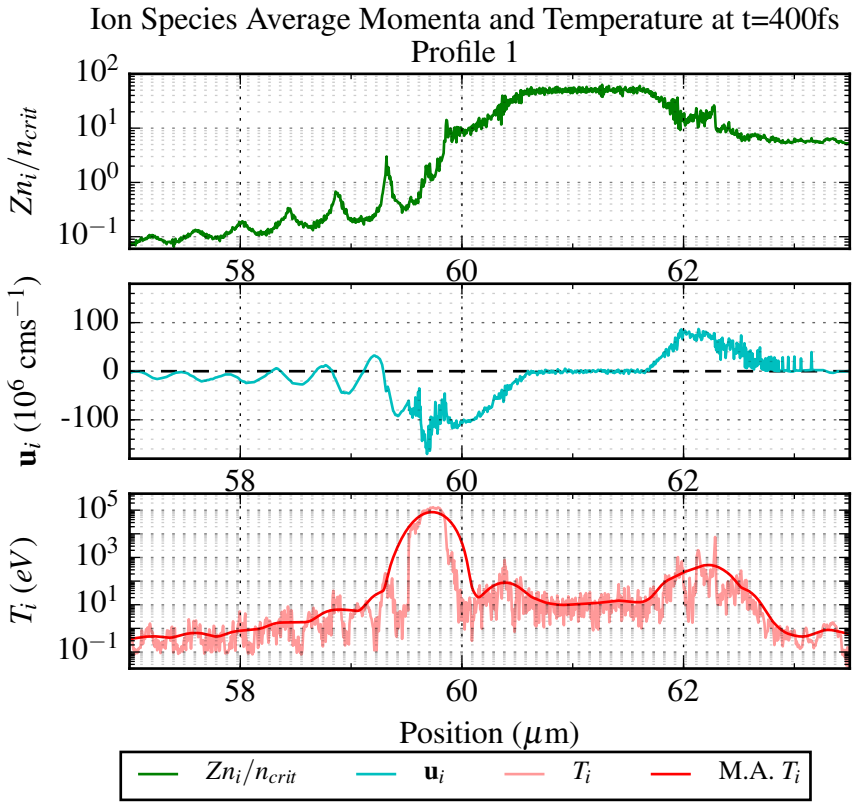

Figure 4.9: Results for ion density n_i, ion-species cell-average velocity $\mathbf{u}_i$ and ion temperature T_i. Taken ~ 40 ps after the laser pulse interacts with the critical surface, the majority of the pulse has now reflected. The ion temperature profile shows some noise and so a windowed moving average (denoted M.A. T_i) is also plotted. There is also some indication of a resonant process occurring in the lead up to the critical density, though the energy in this process is dwarfed by the collisional absorption past n_{crit}.

The ions are likely to carry the majority of the momentum in a collisional shockwave and so it makes sense to look first at the ion temperature, density and

velocity. The ion velocity is calculated by taking a centre-of-mass average velocity of all of the ion species on a cell-by-cell basis. By calculating a total ion thermal energy density per cell an average ion temperature profile can be generated so that $\sum_s n_s T_s = n_i T_i$. The average ion temperature and centre-of-mass velocity are plotted along with the ion density in Fig.4.9. There is a significant peak in the temperature, up to $\sim 10^5$eV, close to the critical density ($\sim 59 - 60$ μm in Fig.4.9), followed by a secondary peak around the region where the singly ionised material starts (> 62 μm). The temperature in the peak close to the critical density is likely to be unphysically high. This region is particularly dense, and so it is probably that the Debye length is not resolved at lower temperatures, and so mode-aliasing, or self-heating, make have contributed to the increase in temperature. However, it is entirely reasonable that a high temperature could be expected in a dense region, given the dependence of the electron-ion collision-frequency on density.

Interestingly the first peak around n_{crit} is followed by a very large negative peak in velocity at ~ 60.5 μm, indicating that there is significant outflow of material from the bulk towards the heated region. There is a forward spike in the ion momenta slightly before the critical region directed towards the bulk, at a velocity of around $2{\times}10^7$ cms^{-1}, which is close to the experimentally measured velocity, however without further calculation it is not clear whether a hydrodynamic shock can form that can match the experimental results.

To test whether a hydrodynamic shock can form, with similar properties, over the timescales required by the experimental results the Lagrangian hydrodynamics code described earlier is initialised using both the output from HYADES and the velocity and temperature profiles supplied by output from EPOCH. Since the EPOCH simulation was initialised so that $T_i = 0$, meaning that the T_i and $\mathbf{u}_i$ profiles can simply be added together. In order to avoid numerical instabilities, the density profile from HYADES used to initialise EPOCH will also be used to initialise the Lagrangian code (see Fig.4.14). To further avoid numerical instabilities and spuri-

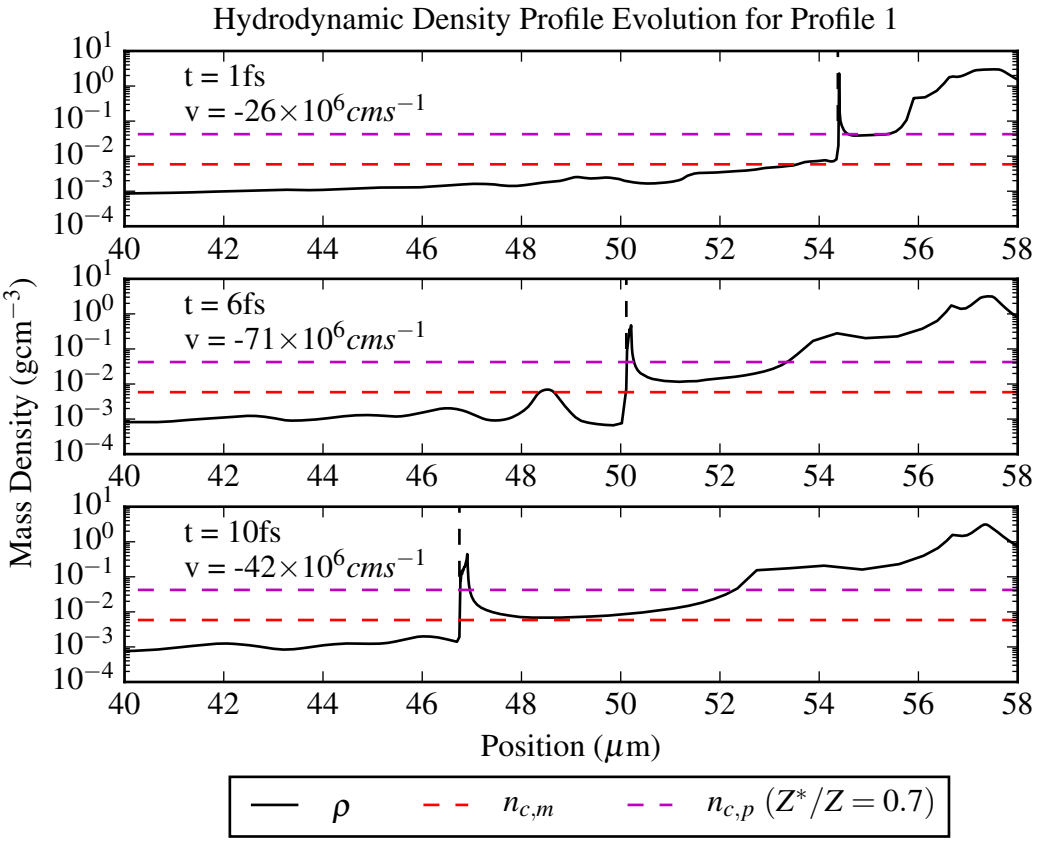

Figure 4.10: Density profiles from a Lagrangian hydrodynamics simulation initialised using output from EPOCH profile 1. A large shock is observable travelling away from the bulk plasma. The enhancement past a 4x compression in the initial formation of the shock appears to be as a result of passing through smaller disturbances around the initial shock front.

ous shocks formed by high frequency noise in the output from EPOCH a windowed average is used to smooth out, with a Hann window function[150,151] being described as:

$$w(x) = sin^2\Big(\frac{\pi x}{N-1}\Big) \tag{4.2}$$

where x is the position and N is the width of the window, which is set to 151 cells with a dx = 5 nm so that the windowed region is approximately 0.75 μm, with a FWHM of 0.376 μm. This particular scheme was chosen due to it's simplicity and the fact that the function matches gradients slightly better to the original signal and is not as distorted by extremely steep gradients as much as a flat window shape is.

The output from the Lagrangian code at several time-steps can be seen in Fig.4.10. The output from the code shows a large shock develop early on and then travel outwards at a velocity of around 6×10^7 cms^{-1}, this shock quickly sweeps up any other disturbances in front of it which effectively stops any smaller shocks or shock-like disturbances from forming in the low-density region.

4.4.3 EPOCH Setup Profile 2; Electron Density Profile

An alternative way of preparing initial density profiles for EPOCH is explored given the absence of any shock formed that could match the experimental results in the previous analysis. In order to obtain a more accurate fit to the electron density, particularly around the critical density at $n_{crit} = 1.7 \times 10^{21}$ cm^{-3} (or $\gamma n_{crit} = 2.2 \times 10^{21}$ cm^{-3}), the electron density from HYADES will be used instead of the previously used ion density. The laser pulse shape, ion species (65% O and 35% Si, with ionisation energies from NIST), electron temperature ($T_e = 10^4$ eV), are taken from the original EPOCH simulation without alteration. However the density profile for the fully ionised section of the simulation is calculated straight from n_e in the HYADES simulation. Again while $\hat{Z}$ has a steep gradient around the n_{crit} region this is ignored and the plasma is assumed to be fully ionised so that $Z_O n_O + Z_{Si} n_{Si} = n_e$. This treatment leaves a small relatively flat region at n_{crit}, the region after this shows a steep spike in n_e and this is chosen as the start of the singly ionised bulk section (see Fig.4.11).

To account for collisional behaviour, EPOCH's built-in collision routines can in this case be used, as convergent behaviour is obtainable (to within approximately 10%). The Coulomb logarithm Λ is set to a fixed value of 2.5 for the whole volume of the simulation, this value was chosen as despite most of the simulation input having a calculated value of $8 < \Lambda <\sim 10.5$ at $T_e = 10$ keV, the plasma in the HYADES simulation has a $T_e \sim 100$ eV which gives a calculated value of $\Lambda \sim 2.5$ for most of

the simulation domain. The automated routine for calculating Λ in EPOCH uses the cell averaged T_s (where s denotes an averaged ion/electron temperature), which is likely to become unreliable as the assumption of a Maxwellian distribution breaks down due to electron acceleration near the critical density.

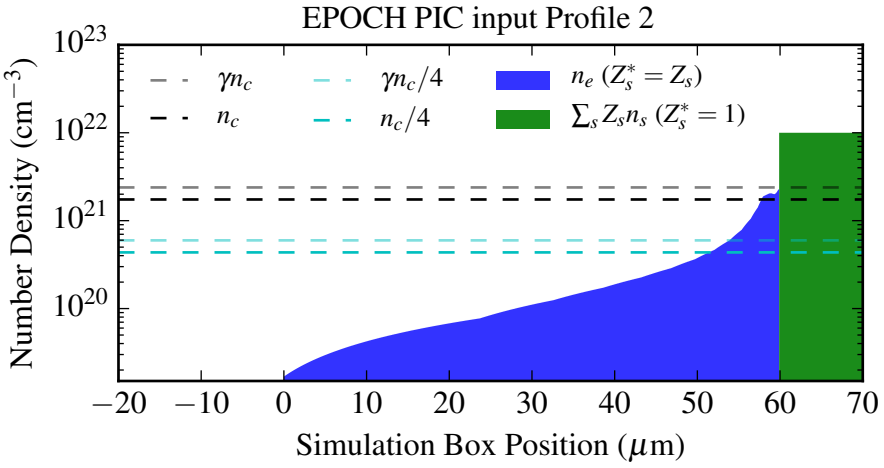

Figure 4.11: The second input density profile for EPOCH PIC, again consisting of five separate profiles which are separated into two regions. The first region is a fully-ionised plasma, an electron density (n_e) and a cold ($T_{i,e}$ = 0 eV) ion/electron density consisting of 65% O and 35% Si so that $\sum_s Z_s n_{i,s} = n_e$. In this profile however a fit to the HYADES *electron* density output at 30fs before the main pulse is used. The second region consists again of cold singly-ionised particles consisting of 65% O and 35% Si, and electrons with a density profile so that $n_e = \sum_s n_{i,s}$.

Whilst the ionisation profile around the ~ 2 μm pump critical density region is not accurately modelled in this simulation, the initial electron density is much closer to that of the HYADES output. There is also a slightly larger n_e leading up towards the critical density, and, in particular, an elongated region around $n_{crit}/10 < n_e < n_{crit}/4$. This elongated near-critical region could result in resonant instabilities like SRS[152,153] especially with the exaggerated electron temperature used here (to minimise PIC self-heating problems). Indeed a resonant instability may already be visible in Fig. 4.9, given that a highly collisional (e.g. lower temperature) plasma is more likely to damp this type of instability and this raises the possibility that T_e may need to be lowered, in which case a much higher resolution grid would be required to achieve convergent results.

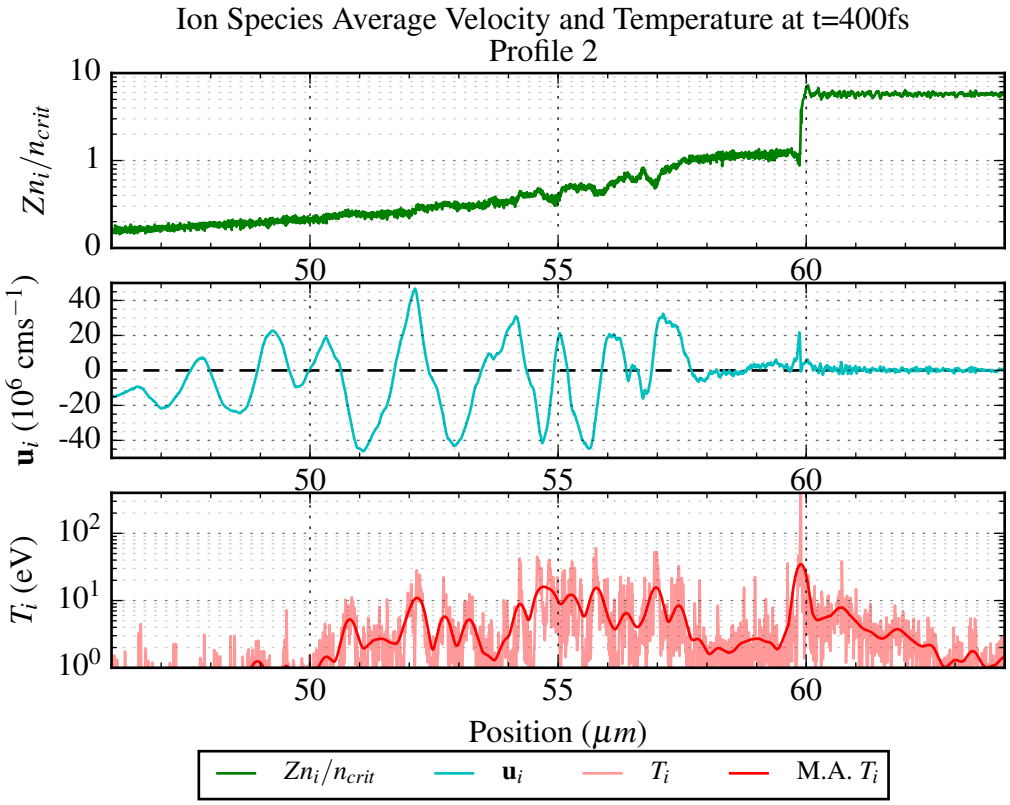

Figure 4.12: Results taken ~ 40 ps after the laser pulse interacts with the critical surface, the majority of the pulse has now reflected. The ion temperature profile shows some noise and so a windowed moving-average (denoted M.A. T_i) is also plotted. There is also some indication of further resonant processes occurring in the lead up to the critical density.

4.4.4 EPOCH Profile 2 Results

The results obtained from using the fit to the electron density rather than ion density, are shown in Fig.4.12, this profile clearly shows a significantly more disturbed low density region between 50 – 58 μm with an oscillating ion velocity profile. The ion temperature appears very chaotic, and though it does appear to be convergent when comparing the results with lower resolution inputs, there is still a significant amount of high frequency noise, despite starting the simulation with 5000 particles per cell. Interestingly the results obtained by using the collisional routines do not differ significantly from those obtained without using the collisional routines. The sharp transition to the over-dense region (at 60 μm) shows some heating to around 20–30 eV at the point that the laser reflects, however, the temperature in this region

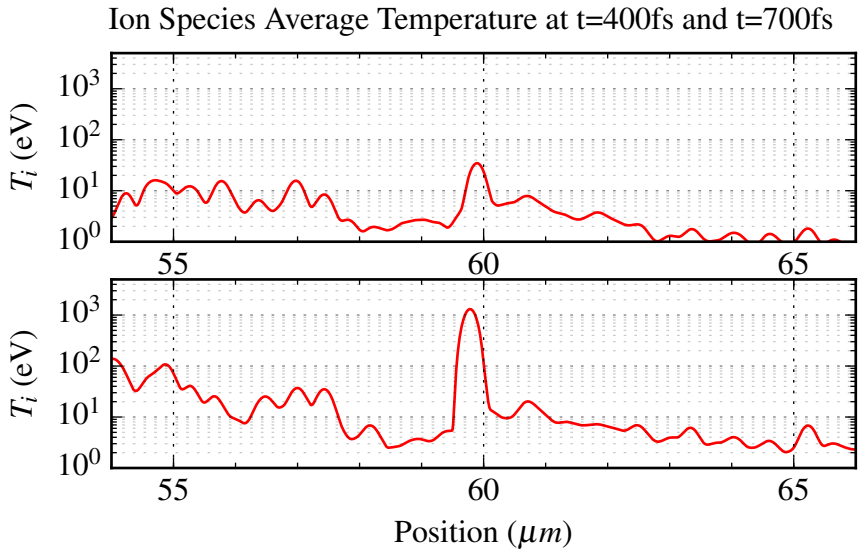

Figure 4.13: Plot showing the rise in temperature at the fully ionised/singly ionised boundary at ~100 fs after the laser pulse reflects (400fs after the simulation start) and ~400 fs after the laser pulse reflects (700fs after the simulation start point).

does increase significantly later in time to around 1000 eV at t = 700 fs (see Fig.4.13), some 300fs after the reflection of the main pulse. The timing of the formation of this peak in the ion temperature in this region indicates that some transport across this region, likely super-thermal electrons, is responsible for the heating. The shape and location of this peak in temperature is thus heavily dependant on the initial ionisation profile input into the simulation. Given that a simple step profile is used here, rather than a more sophisticated approach, the position, amplitude and envelope of the temperature peak seen at x = 60 μm and at t > 700 fs is unlikely to exactly match a profile with a finite gradient. The velocity profiles at this time were significantly more disturbed and suffered from a large amount of high frequency noise. The dynamics of this particular system, due to an under-estimate on electron-ion collisionality, are unlikely to be suitable for a hydrodynamic treatment at later times.

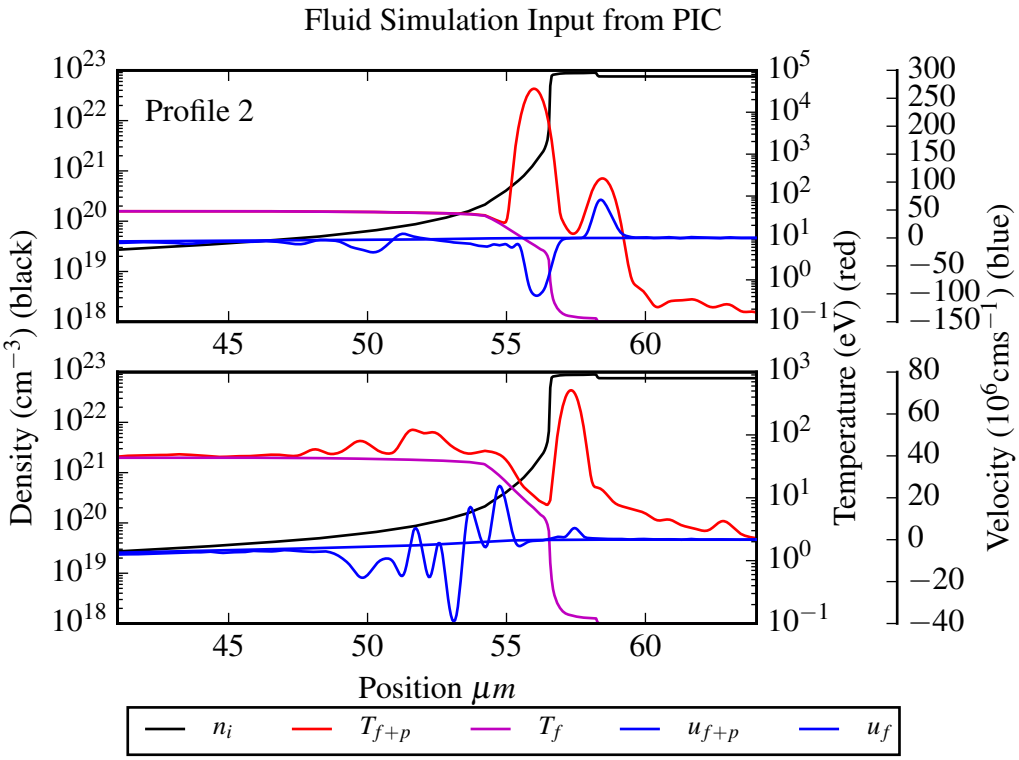

Figure 4.14: Average ion velocity and temperature profiles from EPOCH outputs are linearly added to the HYADES profiles used to initialise the EPOCH code, whilst just the original mass density profile from HYADES is used. The first plot shows the input from the first EPOCH profile where the ion density is used to initialise the code, the second plot shows the input from the second EPOCH profile where the electron density is used.

4.4.5 Hydrodynamic Simulation of EPOCH Outputs

To obtain results that are comparable to the experimental results the PIC output is again put into a simple Lagrangian hydrodynamics simulation. The ion-velocity profile from EPOCH at t = 400 fs and the ion-temperature profile at t = 700 fs are added to the HYADES profile used to initialise EPOCH and then put into a form suitable for the Lagrangian code, most notably by using the Hann-windowed moving average filter to remove high-frequency noise. The calculated input profiles for the Lagrangian code from both the first and second profiles are shown in Fig.4.14.

To compare the hydrodynamic simulation outputs to the experimental results the velocity of the critical surface that a 266nm probe pulse would reflect off needs to be calculated. This is done initially by finding the cell with a mass density $\rho_{p,crit}$

matching the critical density closest to the laser entrance side of the simulation box. This mass density is found, assuming $\hat{Z}n_i = n_e$, using the following calculation:

$$\rho_{p,crit} = \frac{n_{p,crit} A m_p}{\hat{Z}} \tag{4.3}$$

where A is the average ion mass number, m_p is the mass of a proton, and $\hat{z}$ is the average ionisation in that cell. Since the Lagrangian code does not include an ionisation model it is not able to provide an average ionisation and so several values between 0.8-1.0Z ionisation are calculated as an approximation. A higher ionisation range is chosen as this region has undergone significant heating from hot electron transport. The velocities at the calculated $\rho_{p,crit}$ surfaces are plotted as a function of time and compared to the experimental values in Fig.4.15. The first profile shows a critical surface which is coincidental with the shock front shown in Fig.4.12 and hence the continual velocity away from the bulk target. The oscillations in the velocity of that surface are likely to do with the surface passing through unstable low-density regions. The second profile shows an initially stationary surface followed by an inwards motion between $2 - 7$ ps at a similar velocity to the inwards motion recorded in the experiment at 2ps, followed by a rapid transition to an outwards motion at $t > 8$ ps again at a similar velocity to that recorded in the experiment between 4–16 ps. Several adjustments to the input in the Lagrangian hydrodynamics calculation are now required. The over-dense plasma (located at 53-60 μm) in the second EPOCH profile is not accurately modelled; comparing this input profile Fig. 4.11 to that of the first profile Fig. 4.8 it can be seen that there is a very large difference in density. The over-dense region, particularly around the compressed pre-plasma shock-front, is likely to undergo significant ionisation from fast-electron heating, and as a result using a fit to the initial electron density under-estimates the final electron density and so the absorption in this region significantly. Looking at the temperature profiles visible in Fig. 4.14 it can be seen that the large temperature

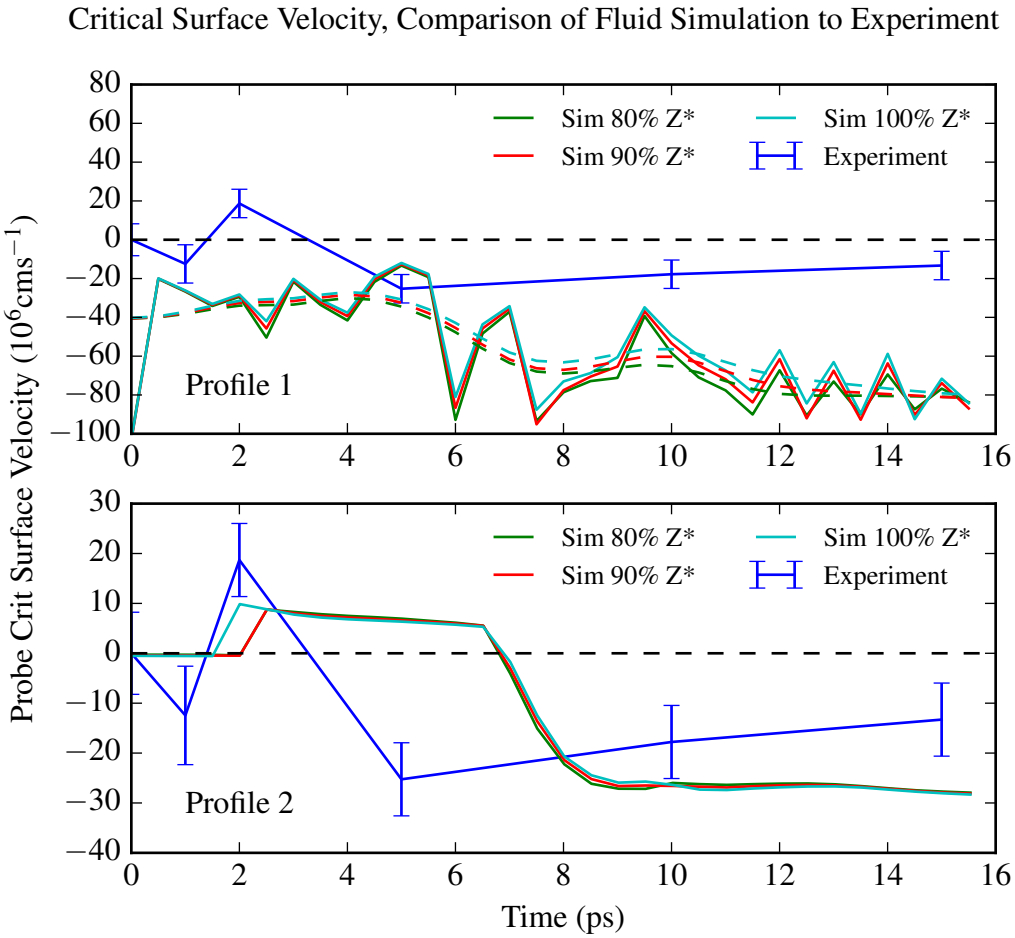

Figure 4.15: Plot of the temporal evolution of the probe critical surface velocity $n_{c,266nm}$, in blue for the experimentally measured results, and as other colours for the velocity of a calculated probe critical-surface for a variety of possible values of $\hat{Z}$. The first plot is calculated using the critical-surface velocities taken from the Lagrangian hydrodynamics simulation initialised using the profile 1 model, showing some indication that the expansion velocity of the target bulk is close to correct, but does not show an inwards travelling shock. The second plot is calculated in the same way but initialised using the profile 2 model, where an inwards travelling surface is visible for an extended period, followed by an outwards motion from the target bulk, similar to the experiment. However the timing of onset of outwards expansion after the inwards motion does not match experiment.

peak in the first profile (with a significantly higher n_e in the over-dense region) is slightly further forward than for the second profile with the under-estimated n_e in the over-dense region. To take into account the temperature peak at 60 μm (in profile 2) can be moved forward by approximately 1 μm, as seen in Fig.4.16. Whilst this does appear to be an arbitrary amount, it is broadly consistent with the fact that the HYADES ionisation profile has a finite gradient starting at fully ionised around the

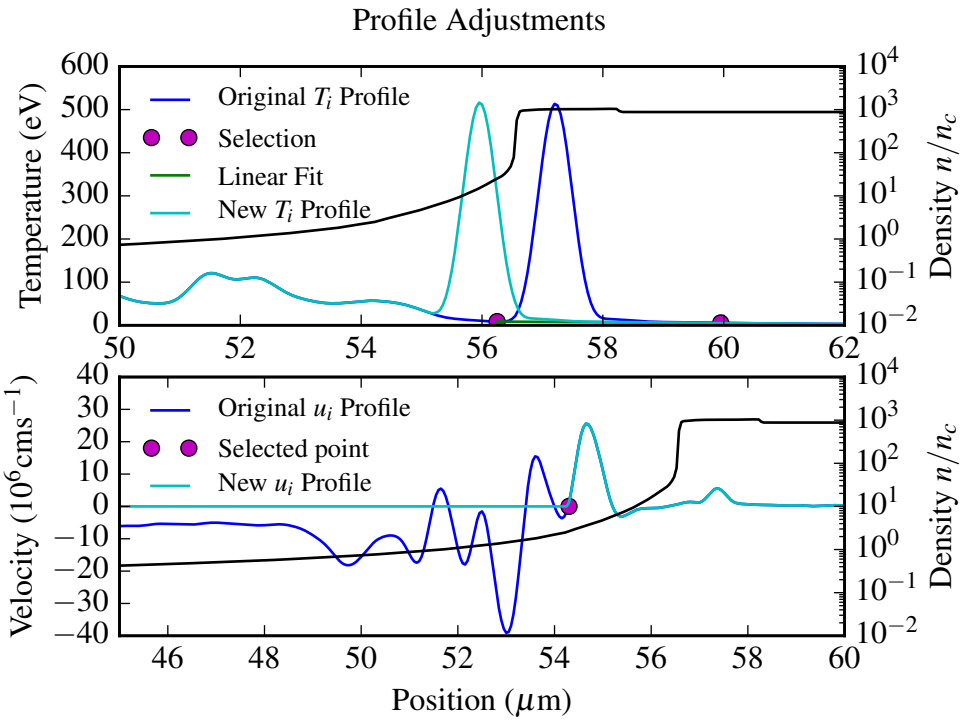

Figure 4.16: Plots displaying adjustments made to the input of the Lagrangian hydrodynamics code from Profile 2. The topmost plot shows the alteration of the position of the temperature peak, made by moving the peak forward by 1 μm. The bottom picture shows the removal of the velocity perturbations prior to the perturbation produced at the critical density.

critical density ~ 54.5 μm to singly ionised at 60 – 62 μm region (see Fig.4.7, noting that the x-axis in the Lagrangian profiles are offset by 2 μm). This adjustment is supported by the results from the first EPOCH profile, where a temperature peak is formed at a similar position (see Fig.4.14, where the peak sits at ~ 55 μm). Whilst the temperature peak in that simulation is significantly larger, it is possible that a significant amount of ionisation at this point will reduce the temperature of the peak, as energy is required to ionise the material at this point. The second alteration shown in Fig.4.16 that can be made is that of removing the motion of the excited plasma leading up to the critical density, whilst this does not improve the fit to the experiment in any significant way it does show an easy to understand picture of what is possibly happening at the surface that the probe pulse is reflecting from. The comparison of the experimental results to the Lagrangian hydrodynamics code are

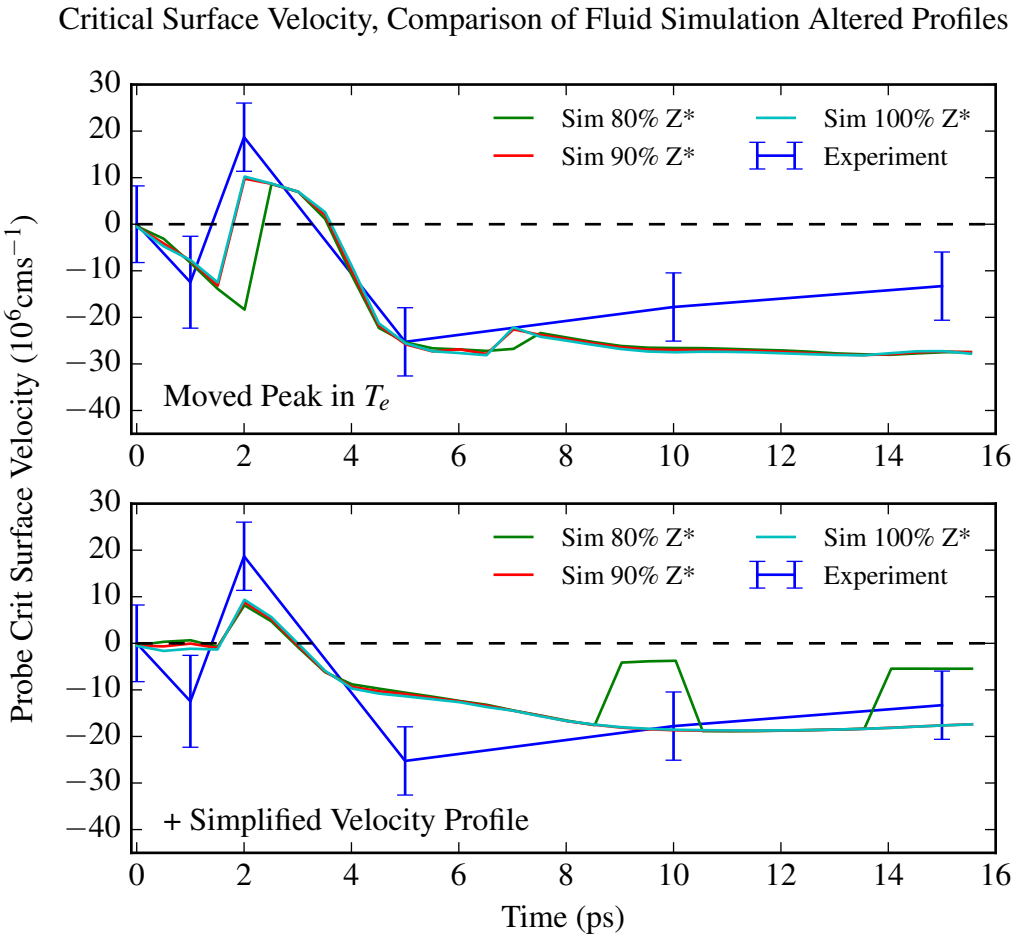

Figure 4.17: Plot of the temporal evolution of the probe critical surface velocity $n_{c,266nm}$, in blue for the experimentally measured results, and as other colours for the velocity of a calculated probe critical surface for a variety of possible values of $\hat{Z}$. The topmost plot is calculated by initialising the Lagrangian hydrodynamics code using just the adjustment to the temperature peak shown in the topmost plot of Fig.4.16. The bottom most plot shows results calculated using both the temperature peak adjustment and the velocity adjustments shown in Fig.4.16.

shown in 4.17. Both sets of results from the altered input profiles show a significantly improved match to the experimental results. The very early time results at $t < 2$ ps show a slightly negative velocity corresponding to an initial outwards motion from the expanding temperature peak consistent with the negative velocity measured at 1ps in the experimental results. Density plots from the Lagrangian simulation show a significant difference in the behaviour of the shock front formed around the critical density when compared to the HYADES simulation results. Both HYADES

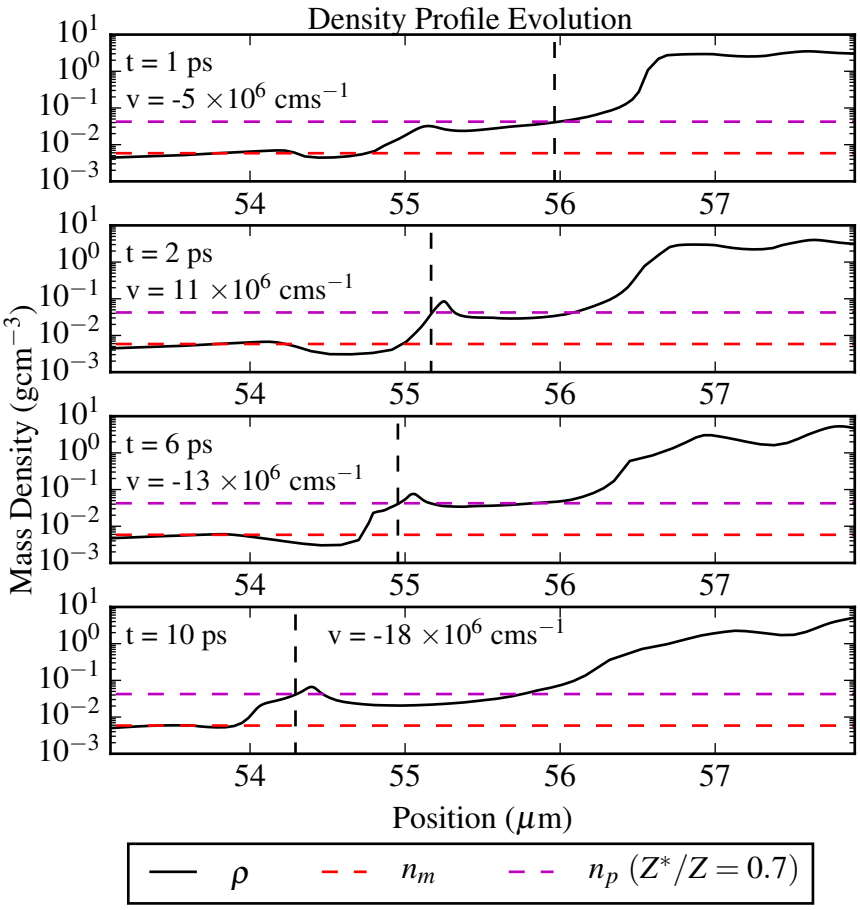

Figure 4.18: Density plots from a Lagrangian Hydrodynamics code initialised using profile 2 adjusted according to alterations shown in Fig.4.16. The critical densities for the main 800nm pulse is shown in red, whilst a critical density for the probe at 266nm with an assumed ionisation of 70% is shown in magenta.

simulations show a shock-like phenomenon developing around the critical region which then travels into the target bulk where it merges with the shock produced by the pre-pulse (see Fig.4.6) later in time. The results from the HYADES-EPOCH-Lagrangian hydrodynamics code approach presented in this section show a very different situation (see Fig.4.18). A shock-like perturbation is produced by the main pulse of the laser which is initially not seen by the 3ω probe (which reflects off the heated bulk of the target). The perturbation gains some mass whilst travelling towards the bulk and at $t \sim 2$ ps the peak in density is seen by the 3ω probe. At this point the description diverges from the previously described HYADES output as the perturbation does not then proceed towards the bulk of the target. Instead it is

swept up in the already expanding target front carrying the perturbation outwards away from the bulk. Given how sensitive the region between $0.25n_{crit}/4$ to $10n_{crit}$ is to minor changes in n_e, and the difficulty in calculating a suitable ionisation profile for use in a PIC calculation, it is unclear which situation is most likely to explain the experimental results.

4.5 Improvements in Modelling

4.5.1 Radiation-Hydrodynamics, HYADES Only Modelling

Whilst the HYADES simulations do agree reasonably well with the experimental results, where both the Helmholtz solver and the Fresnel simulations matched within more than 50% of the error-bars of the experiment, there are some improvements that can be made.

The simplest method to improve on the results from the HYADES radiation-hydrodynamics simulations described above is to use a higher resolution mesh around the critical density region. However improvements in resolution around the critical density region, which evolves significantly over time in a Lagrangian scheme, require very low mass cells at the front surface of the target. The extremely low-mass cells quickly fall out of the low density edge of the tabulated SESAME equations of state provided by HYADES. If there are enough low-mass cells then the laser energy deposition can be modelled as a series of smaller perturbations inside a large number of cells, and there the gradients are well resolved. If there are not enough low-mass cells then a significant amount of energy is dumped into a single cell and large unresolved gradients are set up (i.e $L_{T_e} = {T_e}/{\frac{dT_e}{dx}} > \Delta x$), at this point the hydrodynamic model begins to break down. This is partly due to the thermal conductivity model, a flux-limited model with a hard cut off, not correctly predicting the heat flow across these steep density gradients.[154–158] For the hydrodynamic

model to apply $N_{e,cell} >> 1$, as these cells come closer to an initial $dx \sim 1$ nm scale in length this assumption also breaks down. So there is clearly a balance to be struck between resolving the gradients in the system adequately, whilst staying within the hydrodynamic limit.

The initial target expansion at 0ps < t < 2ps shown in Fig.4.2 could be a result of a number of phenomena: the probe pulse reflecting off different areas of the main pulse interaction region; or super-thermal electron transport, or radiation transport through the shock front not being adequately modelled by the transport packages available in HYADES; being three of the possible reasons.

The first of these possible reasons for the initial expansion (at t = 0 ps) measured experimentally, is due to the target response being a 3D phenomena. The probe pulse, if focused over a the full extent of the interaction region, will have some of the reflected energy arriving from areas close to the center of the main pulse interaction and some from areas around the edge of the pulse.

The second reason for this initial expansion, that of hot-electron heating in front of the compression, is explored in this chapter using the EPOCH PIC model. Electrons accelerated in the near-critical region will travel through the over-dense region with a very low collisionality, depositing energy deeper into the target via collisions, past the critical region, around the compressive shock front produced by the pre-pulse. The outward expansion seen at later times in Fig. 4.18 is likely due to the amount of heating from the accelerated electrons being exaggerated in a 1D framework. In reality the electrons are likely to fan out away from the target normal and so the energy deposition is not likely to be as concentrated.

4.5.2 Radiation Hydrodynamics → PIC → Hydrodynamics

There are several improvements to this method that can be made for increased accuracy, the most notable being an accurate method for putting an ionisation profile into

the PIC code and a 2D radiation-hydrodynamics pre-pulse calculation. Inputting an accurate ionisation profile into EPOCH is extremely challenging. Several attempts were made using a step function density change in n_e, introducing a third region with $\hat{Z} \sim 50\%$ around the critical density. However these simulations could not be made to converge with any reasonable number of particles or grid size given the computing power available. The problem appears to lie with inputting a step-like change in n_e at the critical regions and particle creation (via ionisation) at this point, being subject to a significant level of numerical noise. Whilst turning the collisional routines off does improve the ability to obtain convergent results, this actively switches off some of the phenomena required to absorb the super-thermal electron energy to produce the expanding pre-plasma seen in the experimental results.

Nevertheless it is entirely conceivable that using an ionisation model that calculates relative ion-species densities, like those available in HELIOS, a suitable gradient in $\hat{Z}$ could be input into a code like EPOCH. Care must be taken to match n_e precisely with the calculated ion-densities, as small fitting errors in interpolation routines that allow for a deviation in charge balance from $n_e = \sum_s \hat{Z}_s n_s$ will result in incorrect results and possibly erroneous shock-like phenomena occurring in the PIC code.

Another improvement that could extend the use of this technique temporally, is substituting the Lagrangian hydrodynamics code for a more complete radiation-hydrodynamics code that includes a model for ionisation and possibly radiation transport. Initialising a code such as HELIOS or HYADES from the output of a PIC code would be possible to some extent using profiles in n_e, T_e, and $\hat{Z}_i$,n_i ,T_i, and $\mathbf{u}_i$ for each ion species, though any radiation transport or electron dynamics would still be lost using this method.

Chapter 5

Doppler Spectroscopy and Shock-Velocity Measurements for Low Contrast Laser Systems

5.1 Introduction

The previous chapter focused on the hydrodynamic evolution of a relatively high contrast 10^7 laser-target interaction. Here we explore the effect of using a lower contrast laser pulse (10^5) with a peak intensity of $I_l = 2 \times 10^{18}$ Wcm^{-2}, compared to the $I_l = 10^{28}$ Wcm^{-2} pulse described in chapter 4.

The first section of this chapter is devoted to a description of a pump-probe experiment using an ultra-intense laser pulse of intensity $I_l = 2 \times 10^{18}$ Wcm^{-2} with a 500 ps pedestal with a contrast of 10^5 incident on a polished fused silica target identical to the target used in chapter 4. The second section describes radiation-hydrodynamics calculations, using HYADES, of the ablation of material from the front surface of the target during the pre-pulse. The HYADES calculations are also used as an initial point of reference for understanding several possible hypotheses

for explaining the results from the pump-probe experiment. In the third section kinetic calculations using EPOCH are used to further explore the deposition of energy from the main pulse into the target pre-plasma. The final section of this chapter is devoted to an exploration of the longer term hydrodynamic evolution of the perturbations found in the kinetic calculations in an effort to find a hydrodynamic process to explain the experimental results.

5.2 20TW Pump-3ω-Probe Experiment

5.2.1 Pump Parameters and Probe Setup

The 20TW laser system at TIFR is used to perform a Doppler spectroscopy experiment, where a small amount of the main pump energy is split off into a frequency-tripled probe. The 3ω probe is delayed through a delay stage and reflected at near-normal incidence onto the front surface of the target. The spectrum of the reflected probe is measured, and the Doppler shift in the spectrum can then be used to infer the velocity of the density surface at 3ω critical.

The 20TW laser system at TIFR can provide a pulse of temporal width t_{laser} = 30 fs, and λ_{pump} = 800 nm with a spectral width of $\Delta\lambda_{pump} \sim 30$ nm. The laser is focused to a spot size with a FWHM of 14 μm, and a peak intensity of $I_{pump} \sim 2.0 \times 10^{18}\mathrm{Wcm}^{-2}$. Unlike the 100 TW laser system described in the previous chapter, there is a significant amount of energy in the unamplified ASE pedestal. An amount of energy equal to approximately 15% of the energy incident during the main pulse remains in this unamplified pre-pulse. This can be seen in the temporal intensity profile, which, as in previous experiments, is characterised with a 3rd-order cross-correlator (SEQUOIA). The results from the cross-correlator measurements are shown in Fig. 5.1. The laser system provides an energy of ~ 600 mJ per shot, with a shot-to-shot fluctuation of ~ 6%. The probe pulse used in this experiment is

very similar to that used in the previous experiment as the optics remain the same. Any changes in probe-pulse as a result of the change in intensity and pre-pulse of the pump-pulse are unlikely to be significant as the difference in intensity between pump and probe remain large. For a full description of the probe-pulse setup see section 4.2.

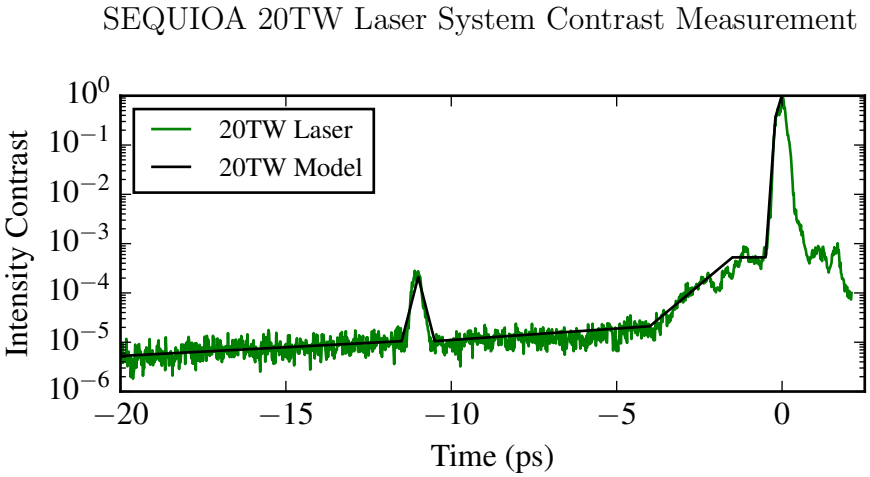

Figure 5.1: Plot of the laser contrast measurements from 3rd order cross correlator (green), and piece-wise linear envelope used in HYADES input to remove high frequency noise (black) between $t = -20$ ps to $t = 2$ ps. The full pre-pulse is ~ 500 ps long, with the intensity (measured again with the cross-correlator) during this time $I_p = 5 \times 10^{12}$ Wcm^{-2}.

5.2.2 20TW Pump-3ω-Probe Experimental Results

The results obtained from this experiment, (see Fig. 5.2), appear to show a similar process to the previous experiment described in the last chapter (see Fig 4.2). There is an initial zero Doppler shift followed by a positive shift (red-shift), at 2 ps, indicating motion towards the bulk of the target, possibly as a result of compression at the front surface. This initial positive shift is followed by a longer period of negative Doppler shift measurements, from 4 ps to 32 ps, showing a surface moving away from the bulk of the target.

The scale of the Doppler shifts observable in Fig. 5.2 are around a factor of ten smaller than those observed in the experiment described in the previous chapter

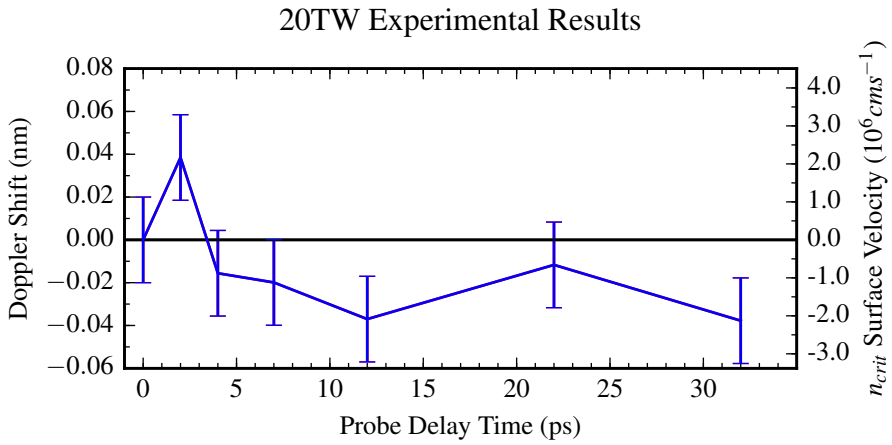

Figure 5.2: Plot of the shot averaged Doppler shift. A blue shift (a negative Doppler shift) would indicate an object travelling towards the spectrometer (a reduction in λ). The right hand axis displays the calculated critical surface velocity, the positive velocity direction was chosen so that it represents material flowing towards the target surface and away from the spectrometer, while material ablating away from the target surface would have a negative velocity. The fitting error on the resulting measured spectrum is smaller than the instrumental resolution of 0.02 nm, and so the instrumental resolution is quoted here.

(see Fig 4.2), which indicates significantly smaller observed velocities. However the time at which the sign of the Doppler-shift changes, around 2-3 ps after the pump-pulse is incident on the target, is similar in both experiments. There is some difficulty in reconciling a similar picture of a shock travelling through a critical surface, as described in the last chapter, for this experiment. The scale-length of the pre-plasma could be expected to be longer in this experiment to that seen in the experiment described in the previous chapter. The longer pre-plasma is due to the higher intensity pre-pulse seen in this experiment compared to that described in the previous chapter.

The increase in density scale-length means that the distance between the pump critical surface (at $n_{crit} = 1.7 \times 10^{21}\ cm^{-3}$) and the probe critical surface (at $n_{3\omega} = 1.6 \times 10^{22}\ cm^{-3}$, noting that $n_{3\omega} = 9n_{crit}$) would be significantly larger, and so for a shock to traverse the greater distance in the same time a larger velocity could be expected to be measured by the probe at this time, which is not what is seen.

5.2.3 Radiation Hydrodynamics Modelling

The 20TW experiment set up can be emulated in HYADES much as with the experiment described in the previous chapter. In the ablated under-dense region higher dimensional effects (such as instabilities or non-symmetrical behaviour) may be relevant. However, given that the pre-pulse intensity is nearly two orders of magnitude larger than that in the experiment described in the previous chapter, the pre-plasma could become significantly more extended than in the previous experiment. This extra extension in low-density plasma ahead of the critical density could result in a variety of instabilities and so a significant loss of energy, which may not be captured by the 1-D radiation-hydrodynamics model.

A 1-D slab like geometry maybe suitable, but given the extra energy deposited in the pre-plasma any plasma-density gradients could develop scale-lengths in excess of the 14 μm spot size. In the ablated under-dense region higher dimensional effects (such as lateral expansion or non-symmetrical behaviour) may be relevant. If the ablation front has a significant enough outwards velocity any low density plasma disturbances are unlikely to be of significance to the formation of inwards travelling shock-like phenomena.

Given that there is a possibility of increased distortion in the spatial grid when compared to the simulations performed in the last chapter, a grid with an increased spatial resolution, extending to a greater depth the bulk of the target, is required. A 500 μm slab of silicate is used, but with a mesh split into two sections (see Fig . 5.3). The first section consists of 1500 cells over a distance of 40 μm. Each individual cell is constructed so that the cell length $l_i = rl_{i-1}$, with the ratio $r = 1.0015$. The second region consists of the remaining 460 μm of the target, constructed with a ratio of the ratio $r = 1.008$. The ratio chosen so that the length of the first cell of the second section matches the final cell length in the previous section to within 5%.

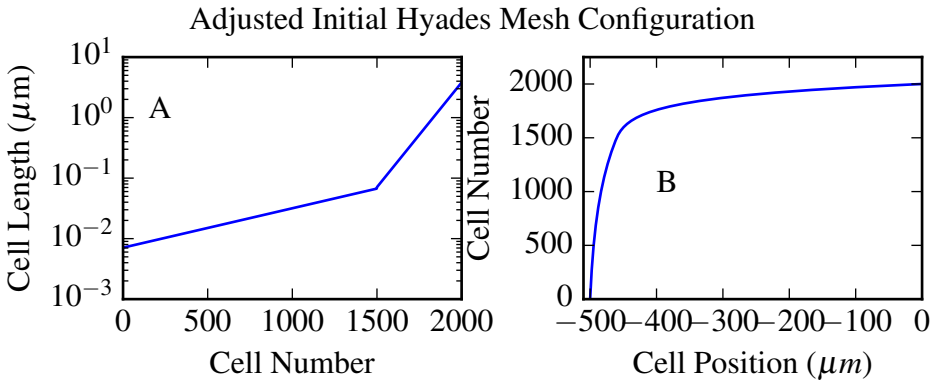

Figure 5.3: The mesh used for HYADES simulations. The mesh is constructed in two parts, the laser facing side consists of a mesh 40 μ**m** long with 1500 cells having a length ratio of 1.0015. The side furthest from the laser consists of just 500 cells with a length ratio of 1.008. The tighter grid spacing on the front surface provides extra resolution at the point where the grid is most likely to distort.

The grid is constructed so that the cells closer to the laser entry side of the simulated slab are much narrower than those on the side facing away from the laser entry side. The increased number of cells towards the laser entry point result in acceptable resolution around the critical density in spite of the increased grid distortion.

The target is modelled in 1D slab geometry and consists of BK7 glass modelled as a fluid with $\hat{Z}$ = 10.00, $\hat{A}$ = 20.028, and ρ = 2.65 gcm^{-3}. An equation of state from the SESAME library for fused silica (record 7386, as previously used in section 4.3.1) is used along with an LTE average-atom ionisation model. The multi-group radiation package is used with 100 photon groups from 10^{-6} to 10^{-4} keV upto 10 keV, as shown in Fig.4.4. Only the Fresnel/Inverse Bremsstrahlung packages are use in the analysis in this chapter as the Helmholtz results show considerable spatial grid distortion despite the increased grid density at the front of the target (ending in a situation where parts of the simulation are no longer described by the EOS table), for a discussion on the physics used in this package see section 3.3.2.3. The laser solver is set up with parameters of λ = 800 nm, θ = 40°, along with plane polarisation, which is consistent with the experimental setup and the setup described in section 4.3.1.

The flux-limited thermal conductivity model is used along with values between 0.3 and 0.05 also as discussed previously in section 4.3.1.

5.2.3.1 Radiation-Hydrodynamics Results

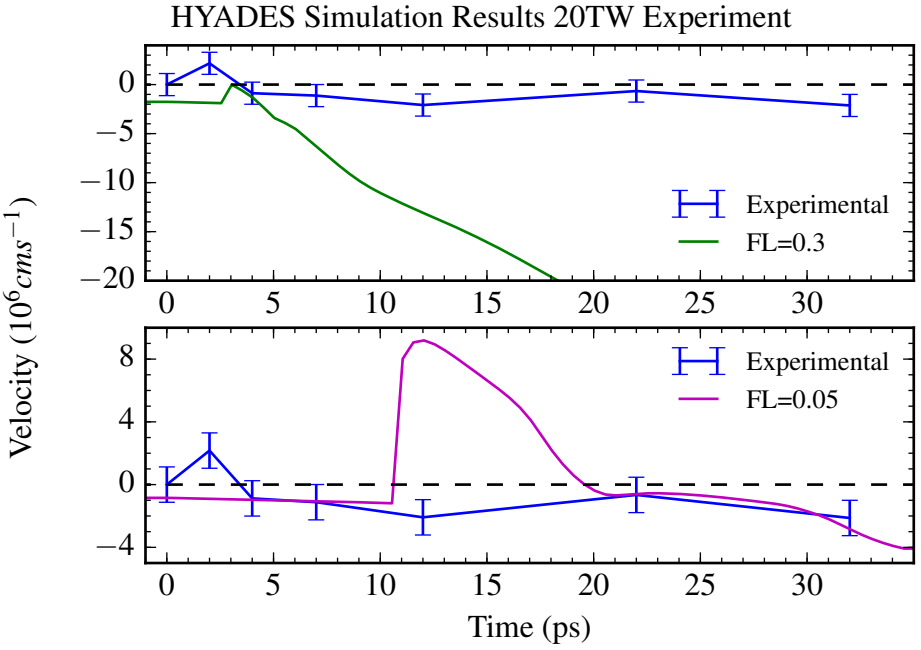

Figure 5.4: Top: HYADES results using a flux limiter values of 0.3. Bottom: HYADES results using a flux limiter values of 0.3 of 0.05. Time $t = 0$ ps corresponds to the impact of the main pulse. Both simulations used a Fresnel reflectivity model for laser absorption.

Results from HYADES simulations in comparison to the experimental data are shown in Fig.5.4. The results from HYADES clearly do not match with the experimental results. At lower flux limiters (bottom Fig. 5.4) there is an inward motion of the critical surface, visible as a large positive velocity peak at $t = 10 - 15$ ps, is far too large and arrives too late compared to the experimental results. Whilst at higher flux limiters (top Fig. 5.4), the inward motion is of a comparable velocity and timing, visible as a small positive velocity at $t = 3 - 4$ ps, but the post-shock expansion, at $t > 5$ ps, is much larger than the experimentally measured velocity.

It is worth looking at the differences between the two scenarios presented by

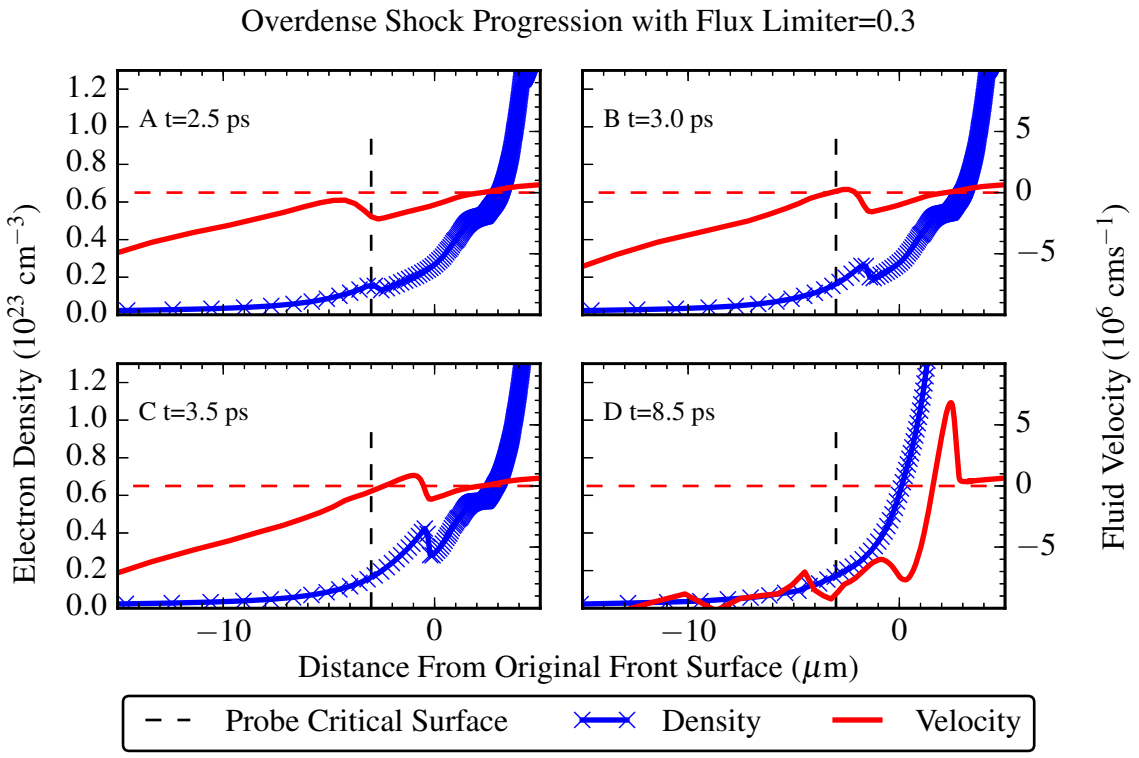

Figure 5.5: Snapshots of electron density at various times after the arrival of the main pulse. Plots are from HYADES simulations using the Fresnel model and a flux limiter set to 0.3. Position is relative to the original location of the target front surface. Time $t = 0$ ps is set to corresponds to precisely mid-way through the main pulse (i.e. the peak of the laser pulse). The dotted lines show the probe density $n_{3\omega}$ (horizontal) and the density surface from which the velocity is obtained (vertical).

the change of flux limiter as they present quite different outcomes. Selected time slices from setting the flux limiter to a value of 0.3 can be seen in Fig. 5.5 where the evolution of the electron density around the probe critical density ($n_{p,crit} = 1.6 \times 10^{22}$ cm^{-3}) is plotted. At an early time, $t = 2.5$ ps, a small compressive disturbance can be seen with a velocity slightly higher than that of the surrounding material, though still away from the target surface. At time $t = 3$ ps the disturbance has travelled further towards the front surface of the target. At this time the density in the disturbance is high enough that the 3ω probe can reflect from the rear part of the disturbance and detects a slightly positive velocity (towards the bulk of the target). Later in time the disturbance travels further into the bulk target and gains velocity as it does so, at these times, $t = 3.5$ ps and later, the probe measures an

outwards velocity as material is ablated from behind the forming shock.

In the simulation using a flux limiter of 0.3, while the probe critical surface velocities did not match the experimental values well, the shock-like perturbation has some possible similarities to the experimental results. The first of these similarities is the apparent magnitude of the velocity of the disturbance, Fig. 5.5C shows the disturbance a short time after it has passed through the probe critical density $n_{p,crit}$. At this time the apparent velocity of the disturbance is similar to that of the initial disturbance measured in the experiment (approximately 2×10^6 cms^{-1}).

Whilst the timing and the dynamics of the shock-like perturbation appear close to the experimental values at early times during the simulation, the later time-evolution of the simulation is very different. There are a number of possible reasons for the apparent divergence from experiment. One possibility being that the main pulse could have lost energy to kinetic plasma instabilities in the longer pre-plasma. Another possibility is that there are dimensional effects which cannot be simulated using a 1D slab geometry. One of the most notable geometric effect being that of lateral expansion which could have the effect of a shortening of the plasma scale-length, so that any outflow from the rear of the shock surface falls off to lower densities past the probe critical density. This would have the effect that the probe could follow the disturbance further into the target, and so measure the velocity closer to the shock front for a longer time. A third possibility is that pre-heat from fast electrons deposition reduces the speed of the shock as it enters the higher density region, however this might be expected to increase the blow off velocity later in time. Some of these possibilities will be explored later in this chapter.

Selected time slices from the second simulation, with a flux limiter of 0.05, can be seen in Fig. 5.6, a comparison of the calculated probe critical surface over time to the experimental results can be seen again in Fig 5.4. There is a good match at early and later times, before 10 ps and after 20 ps (see the bottom plot in Fig 5.4), between the experimental results and the 0.05 flux limited simulation.

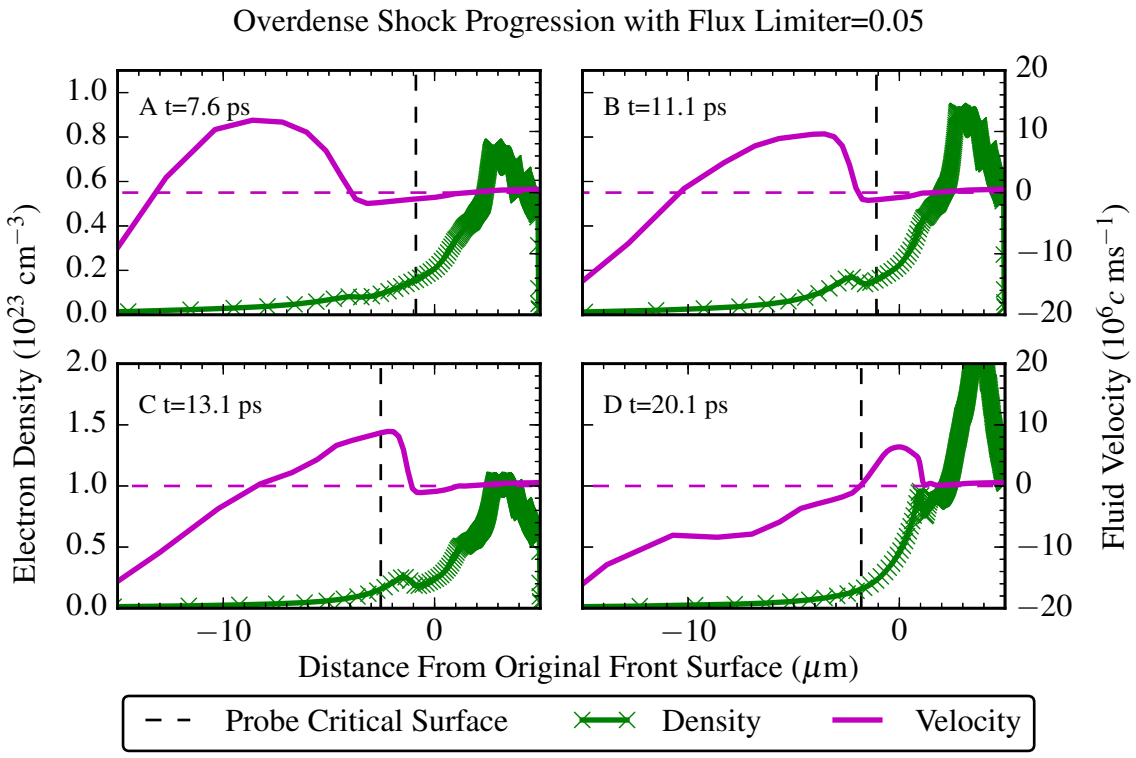

Figure 5.6: Snapshots of electron density at various times after the arrival of the main pulse. Plots are from HYADES simulations using the Fresnel model results and a flux limiter set to 0.05. Position is relative to the original location of the target front surface. Time $t = 0$ ps is set to corresponds to precisely mid-way through the main pulse (i.e. the peak of the laser pulse). The dotted lines show the probe density $n_{3\omega}$ (horizontal) and the density surface from which the velocity is obtained (vertical).

However a large inwards motion can be seen occurring between 10 ps and 20 ps which is not recorded in experiment, though this could be a related phenomena (e.g. a large compressive shock travelling towards the target bulk) to that occurring in the experiment at 2 ps. The density evolution profiles seen in Fig. 5.6 show a shock with a much larger positive velocity than observed in the 0.03 flux limited simulation. This perturbation is initially present at lower densities than the probe critical density, see Fig. 5.6A. After approximately 10 ps, the perturbation travels towards the higher density region accessible by the probe, where a positive velocity can be seen for another 10ps period, Fig. 5.6B-C. The final sub figure, Fig. 5.6D, shows out-flowing plasma from the back of the shock as it travels towards the bulk target.

While both of these simulation match the experimental results at particular times, the 0.3 flux limited simulation showing similar inward motion initially, and the 0.05 flux limited simulation shows similar outflow from the front surface of the target, neither fit the experimental results well overall.

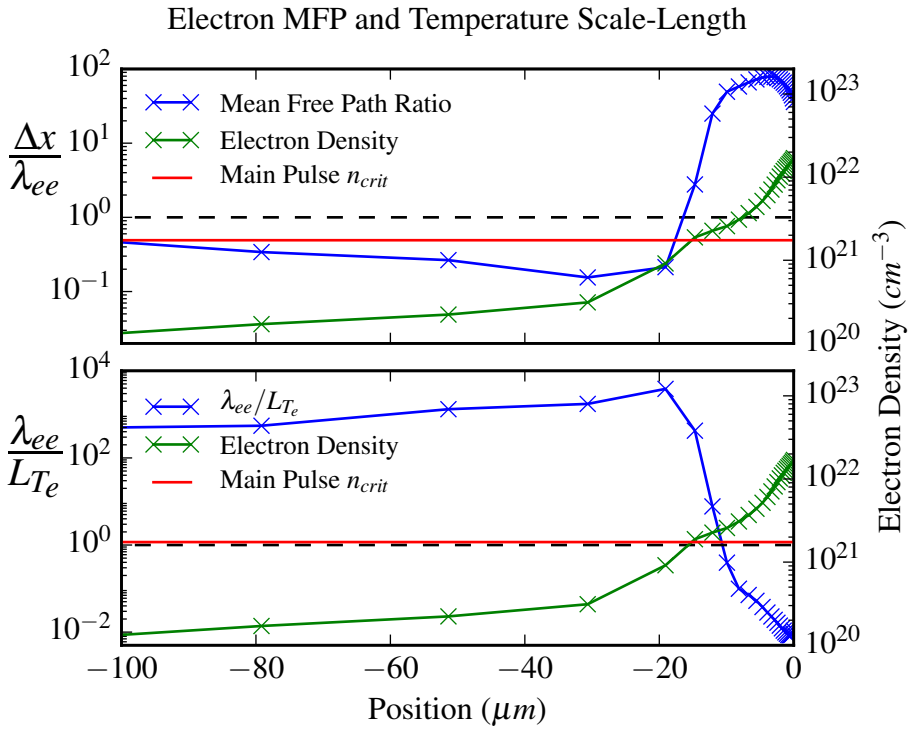

Figure 5.7: Snapshots taken at the arrival of the main pulse in a HYADES simulation using the Fresnel model and a flux limiter of 0.05. Top: The ratio of the electron-electron mean-free-path λ_{ee} to cell size plotted next to the electron density n_e. The cell length leading up from the low density regions up to the critical density is much smaller than λ_{ee}. Bottom: The ratio of λ_{ee} to the electron temperature scale-length L_{T_e} plotted next to n_e. There is a large region ($\sim 80\mu m$) leading up to and past n_{crit}, where λ_{ee} is significantly larger than L_{T_e}. The dotted black line in both plots represents where the ratios are equal to one.

To investigate why the results from the radiation-hydrodynamic model are so far from the experimental results some basic assumptions used in this framework can be tested. A fluid cell should be large enough that the interior of the cell can be thought of as in local thermal equilibrium. If the electron-electron mean-free-path λ_{ee} is not contained within a single cell of the fluid, this assumption is violated. If there are temperature gradients with a scale-length L_{T_E} shorter than λ_{ee} then the

assumption of a local thermal equilibrium is also broken.

A snapshot of a simulation just after the main pulse has arrived is used to check these criteria. From Fig.5.7 it is clear that both of these assumptions are violated for an extended region ($\sim 80\ \mu m$) up to and past n_{crit}. It is not surprising that $\lambda_{ee} >> L_{T_E}$ around n_{crit} since this region is subjected to the largest amount of heating. The fact that the region appears to extend so far around this region implies that a fluid picture of the phenomena that could occur here is likely to be inaccurate and that a kinetic approach might show additional phenomena. Whilst the use of a flux-limited thermal conduction model accounts for some of the thermal behaviour there are other processes that cannot be modelled in such a way (e.g. kinetic instabilities).

5.2.4 Particle-in-Cell Modelling

There are several ways an EPOCH simulation can be set up to investigate the main pulse interaction using the pre-plasma conditions outputted from HYADES. The different scenarios are summarised here for clarity, and will be discussed in detail in the remainder of this section:

1 Fully ionised plasma with EPOCH density profiles as $n_e = \sum_s Z_s n_s = \bar{Z} n_i$, fitted from the HYADES n_i.

2 EPOCH profile set with multiple ionisation values and matched to HYADES ionisation, and HYADES n_e.

3 EPOCH profile set up with reduced scale-length density gradients.

5.2.4.1 EPOCH Setup Profile 1, Fully Ionised Plasma

The output from the HYADES simulation using a flux limiter of 0.05 is used to initialise an EPOCH simulation. The lower value for the flux limiter is chosen

initially to maintain consistency between the analysis presented here and the analysis presented in the previous chapter, however the difference in density gradient scale length is very slight when considering only the pre-pulse interaction. A snapshot of the HYADES results at 10 ps before the onset of the peak laser intensity is plotted in Fig. 5.8. The density scale-length appears to be significantly longer in this scenario when compared to the density profile plotted in Fig. 4.7 presented in the previous chapter. Since there is a longer density scale length a longer simulation box will be used in an attempt to capture any low-density laser-plasma interactions that might occur. The first attempt to simulate the laser-plasma interaction in EPOCH uses a

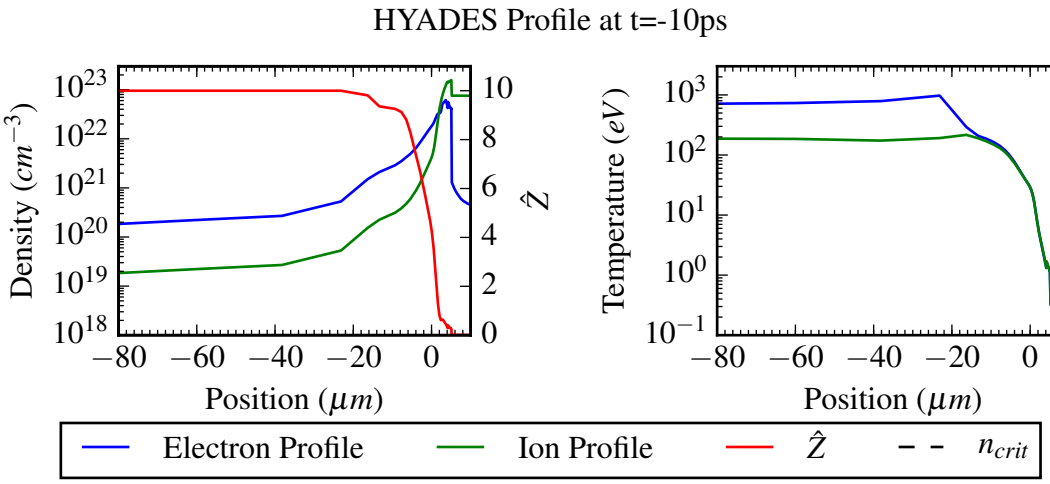

Figure 5.8: Density (left, n_e and n_i) and temperature (right, T_e and T_i) profiles from HYADES simulation with a flux limiter of 0.05. Taken at a time 10 ps before the onset of the peak laser intensity (see 5.1). in addition to the density profiles the left plot shows the average ionisation per cell $\hat{Z}$ in red, while the front surface appears fully ionised there is a sharp drop at 78-81 μm down to a very low ionisation fraction.

fit to the ion density n_i shown in Fig. 5.8. Since the ionisation is roughly constant past the critical density and stays close to constant up to the probe critical density ($n_{p,crit} \sim 9n_{crit}$) the entire simulation box is treated as fully ionised and the electron density is chosen so that $n_e = \sum_s Z_s n_s$. As used in the previous chapter the ion population consists of two sub-populations with 65% oxygen ions and 35% silicon ions. There are 2500 particles per cell divided between the electrons (60%) silicon ions (20%) and oxygen ions (20%).

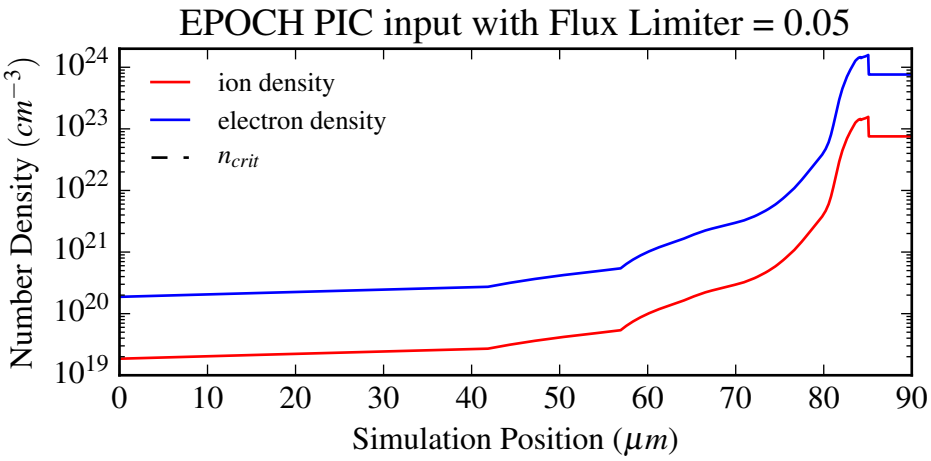

Figure 5.9: Ionisation is not taken into account in this simulation as the average ionisation is roughly constant until significantly past the probe critical density, and so plotted above is the electron and ion density profiles used in profile 1. The electron density is set so that $n_e = \sum_s Z_s n_s$, where s is an ion species. Ion species are set up so that $n_O = 65\% \hat{Z} n_e$ and $n_{Si} = 35\% \hat{Z} n_e$.

The simulation box is 18,000 cells in length with a cell length of 5 nm making a 90 μm box. In order to minimise numerical artefacts and minimise self-heating the current smoothing options and 3rd order spline particle shape options are used. These options are necessary as the density profile in this scenario goes to quite high densities ($> 10^{24}$ cm^{-3}), at these densities it is extremely difficult to obtain a convergent result. For example at a density of 10^{24} cm^{-3} and given the cell length of 5 nm, an electron temperature of > 500 keV would be required to resolve the Debye length λ_d. At such high temperatures the density profile would undergo significant thermal expansion and so the density profile that the laser interacts with would not be the density profile that is input into the PIC code initially. For this reason the initial electron and ion temperatures have been set to zero. While this is unrealistic when compared to the HYADES codes, it is hoped that given the temperatures that should occur later in time, at least in the low density regions, that there will be sufficient resolution to obtain reasonable results.

The collisional routines supplied in the EPOCH package are used in this scenario, as it was found that without collision routines no absorption of the electron

plasma wave, excited by the laser pulse at around the critical density, occurred. This meant that the energy in the electron population was not efficiently coupled with the ion population. Collisions are set with a Coulomb log Λ_c = 2.5 based on the temperature and density profiles from the HYADES calculation.

The laser pulse is a plane polarised pulse with a Gaussian envelope with of width $t_{2\sigma}$ = 18 fs (corresponding to a t_{FWHM} = 30 fs) and an intensity set to $I = 10^{18}$ Wcm^{-2}. The envelope for the laser is set to $5t_\sigma$ with the peak intensity at $2.5t_\sigma$ so that the there is no sharp truncation to the pulse envelope or any high frequency noise as a result of truncation.

5.2.4.2 EPOCH Profile 1, Fully Ionised Plasma Results

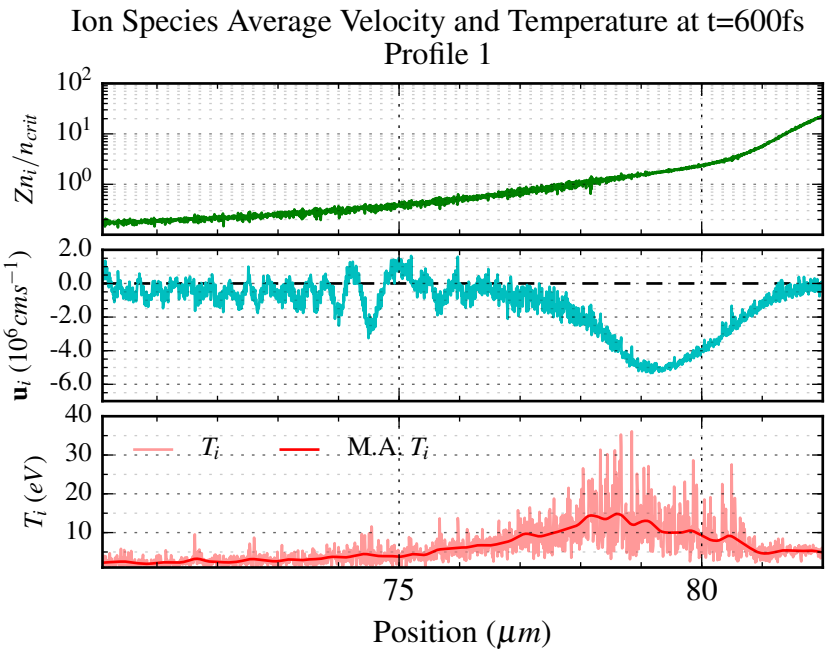

Figure 5.10: Plots from the first PIC input profile results. The top plot shows the ion density profile normalised by n_{crit}/Z, the middle plot shows the ion velocity profile and the lower plot shows the ion temperature profile. Results are taken approximately 150 ps after the main pulse is incident onto the pump critical surface.

The ion temperature and cell averaged ion velocity are shown alongside the ion density profile in Fig. 5.10. These profiles are taken at a time approximately

150 ps after the reflection of the laser pulse at the critical surface. A fairly small temperature peak is observable at 75 μm in the region around the critical density (n_{crit} is located at 78 μm) along with a negative velocity peak. While there are small positive peaks in velocity at approximately $n_{crit}/4$, possibly as a result of an excited ion acoustic wave, none are close enough to the over-critical region to be picked up by the probe (at $9n_{crit}$). The low density plasma leading up to the critical density is

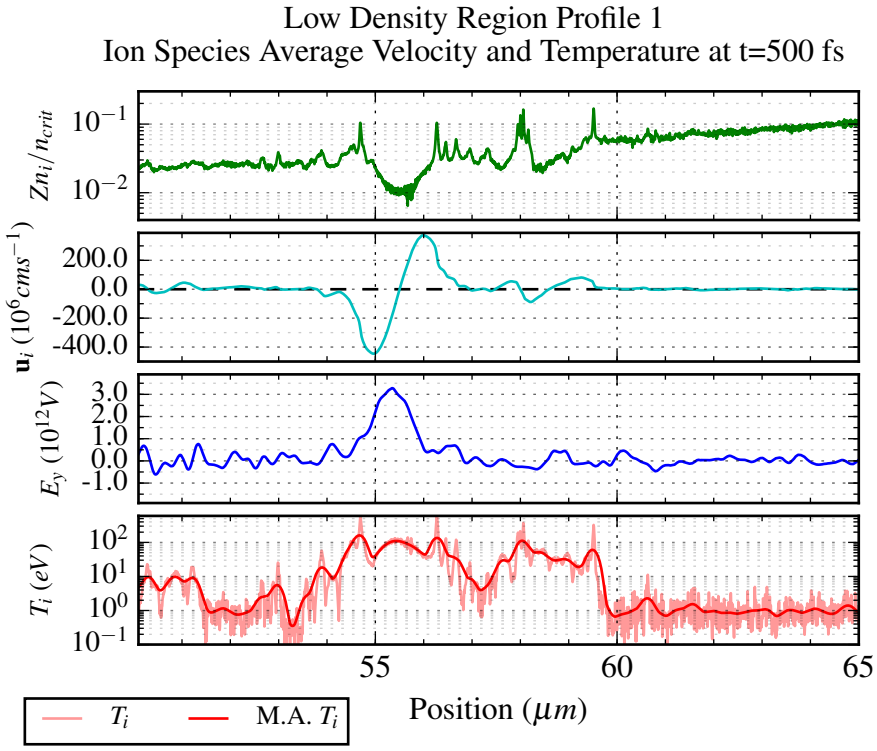

Figure 5.11: Plots from the first PIC input profile results. These plots focus on the low density pre-plasma ~ 15 μm in front of the pump critical surface. The top plot shows the ion density profile normalised by n_{crit}/Z, the second plot shows the ion velocity profile, the third plot shows the electric field in the y-direction E_y, and the fourth lower plot shows the ion temperature profile. Results are taken approximately 50 ps after the main pulse is incident onto the pump critical surface, though slightly before the reflected pump pulse passes through this region.

significantly disturbed by the passing laser pulse (see Fig. 5.11 between 55-60 μm), which may explain why there is no significant shock like phenomena observable closer to the critical density. The later evolution of the low-density region as seen in this simulation is not likely to match the experimental behaviour as the experimental

set up has the main pulse incident at 40^o to normal rather than perfectly normal as necessarily assumed by the 1D PIC. In the case of a perfectly normal incident pulse, the low density region of plasma is excited by both the incident pulse and the reflected pulse, and so the later time evolution (after the incidence of the pulse on the reflective region of the plasma) of this region of the plasma is not likely to evolve in a realistic fashion.

There are two shock-like phenomena observable in Fig. 5.11, the first is visible centred at 55.5 μm, and the second at 58.5 μm. Both regions have undergone significant heating to approximately $100eV$ and show significant disturbances in the ion density. While the plasma in the low-density region is in a very excited state it is unlikely to explain any direct effects on the experimental measurements (i.e. the probe is unlikely to reflect off any density spikes in this region) given how low the density is in these regions and how far away they are from the critical region (78 μm).

The shock like phenomena at 55.5 μm in Fig. 5.11 is of particular interest in its own right. The two pertinent features that are of interest are the electric field at this point and the ion density, resembling those of a post-soliton.[159] There is a large peak in E_y at the central point (55.5 μm) between two peaks in the ion density (at 54.5 μm and 56 μm) and within the two ion density peaks there is a higher temperature (100 eV) than outside them (1-10 eV). For this phenomena to be considered realistic however the collisionality of the plasma in the local area must be extremely low as the formation of solitions requires a hot, close-to-collisionless plasma, though post-solitons have been observed in near-critical plasmas.[160]

5.2.4.3 EPOCH Profile 1, Fully Ionised Plasma Hydrodynamic Evolution

To compare the EPOCH output with the experimental results the longer term hydrodynamic evolution of the system needs to be modelled. For this purpose the

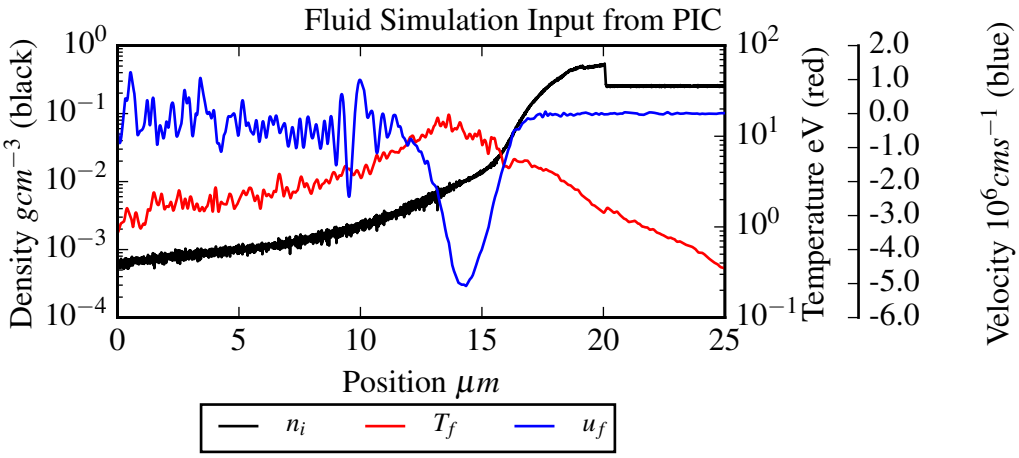

Figure 5.12: Hydrodynamics input taken from PIC code output at 600 fs (see Fig. 5.10).

same Lagrangian hydro-dynamics code as previously used in the last chapter is used again here. The initial conditions for the hydrodynamics calculation are shown in Fig. 5.12. These are taken directly from the ion velocity and temperature EPOCH output shown in Fig. 5.10 though a smoothing algorithm has been used to reduced the high frequency noise seen in EPOCH. Looking in more detail at 5.12 there are several features of interest. The first, most obvious feature is the large negative velocity peak at 14 μm, showing a large outwards motion to the left (from the over-dense section to the under-dense section). The negative velocity peak co-coincides with a thermal peak at around 10 eV which is likely to support any outwards expansion. The second feature of interest is at ~ 9 μm where there is an oscillation in velocity, with a positive velocity of 10 kms^{-1}. This is unlikely to propagate forward or to form a shock, primarily due to the significantly lower mass (and therefore momentum) in that region, and the small spatial extent of the positive velocity perturbation in that region. Probe surface velocities are calculated using the local velocity at the probe's (λ_p = 266 nm) critical desnsity, when testing a wide range of possible ionisation values for this region (from as low as 50% ionisation up to fully ionised) the results are very similar and start at -1.0 ± 0.5 10^6cms^{-1} to -1.5 ± 0.2 10^6cms^{-1}. These outward expansion velocities match the experimental values well,

though there is no initial inwards motion visible in the hydrodynamics calculation. This is not surprising considering that there was no positive motion in the probe critical density region in the PIC input.

5.2.4.4 EPOCH Profile 2, Ionisation Gradient Modelling, Overlapping Populations

Several attempts were made to simulate the effects of ionisation using step-like gradients (single step or multiple step) in either the ion or the electron density, however at the point where the ionisation changes large temperature peaks occur along with spurious velocity perturbations. There is a large gradient in the ionisation profile visible in the HYADES results, as shown in Fig. 5.8, however to properly model the effect of a steep ionisation gradient the gradient modelled in the PIC code must be finite.

To explore the possibility that a sharp ionisation gradient could cause significant temperature/velocity perturbations further, an ionisation profile using multiple spatially overlapping species with different ionisation states can be set up. To achieve this two species of ion are used to represent oxygen and silicon ion species, one species set is fully ionised and the other species set is doubly ionised. This type of setup would give a total of four initial ion species, two oxygen with Z_o = 8 and 2, and two silicon with Z_{Si} = 14 and 2. The total ion density for each ionised species-set $n_{i,zs}$ would still need to be maintained at $n_{i,zs} = 0.65n_{O,zs} + 0.35n_{Si,zs}$. An ionisation for a particular cell $\hat{Z}_c$, and with overall ion density $n_{i,c}$, could then be emulated using $\hat{Z}_c = Z_{i,full}r + Z_{i,2}(1-r)$, where $r = n_{i,full}/n_{i,c}$, and the subscript $i, full$ refers to the fully ionised ion species-set, and the subscript $i, 2$ represents the doubly ionised species-set. The spatial distribution of the ions can then be set up to match the ionisation profile seen in the HYADES result, for instance an average ionisation of $\hat{Z}$ = 5 would mean that a distribution of 37% fully ionised ions and 63% doubly ionised ions would be used.

However using only two species and with the second species being at least partially ionised does mean that ionisations lower than 2 are not accessible. A significant problem with this sort of distribution is the requirement of a large number of particles per cell *per species* for a convergent simulation. A large amount of noise is seen if either species is under-represented as the ionisation process produces a large number of electrons that need to be adequately represented in order to minimise noise in their production. This puts a limitation on where the doubly ionised species can actually be present as large numbers of them will be required even where their number density appears negligible. In practice a lower limit on the number density for the doubly ionised species is needed. This further limits the accuracy to which an ionisation profile can be matched. This limit is set to 10% of the lowest density in the fully ionised species; any higher and a reasonable match to the HYADES ionisation profile cannot be obtained. Any lower and the code becomes unfeasible to run on the computing resources available. Density profiles for the various species populating a new EPOCH input profile are shown in Fig. 5.13. The ionisation profile in the new profile is a far better match for the HYADES output profile than the previous step gradients, however there is still a steep gradient visible in the doubly ionised species (the green plotted line in the top plot of Fig. 5.13).

The new EPOCH profile uses a smaller simulation box of 50 μm, with a higher spatial resolution of 2.5 nm, with the hope of limiting noise at higher densities. There are 500 particles per cell shared between ions and electrons so that initially there are 300 electrons per cell. There a varying number of ions per cell due to their uneven distribution, though with not less than 50 particles per cell per species. The number of electrons per cell rapidly rises in the higher density regions due to particle creation via ionisation, which results in significantly better statistics at later times and at higher densities. The simulation is run with collisions, again using a coulomb log of 2.5. The simulation is run twice, both versions include the field ionisation model, though one uses collisional ionisation, and one without.

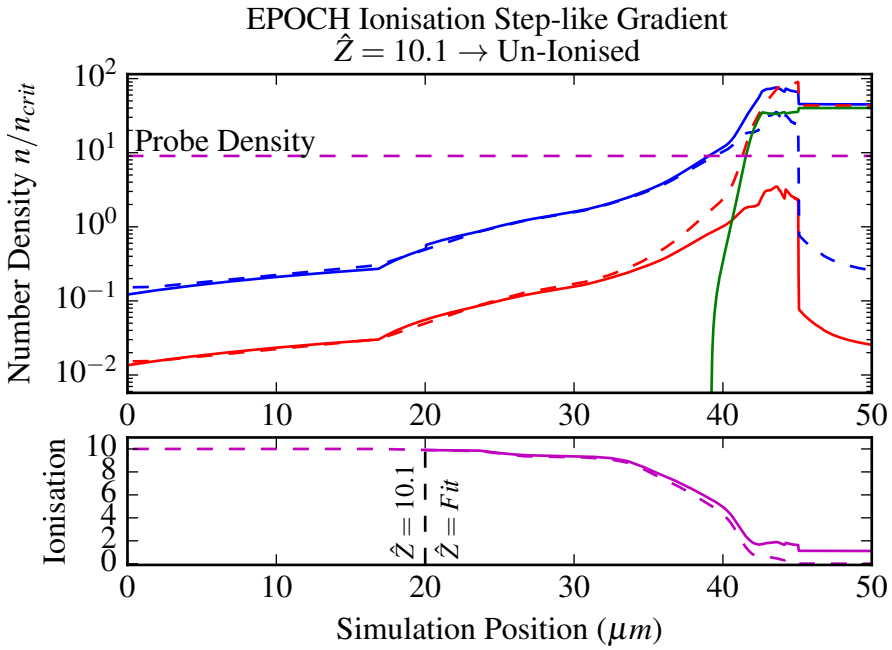

Figure 5.13: Density profiles for input into EPOCH compared to HYADES output. In the upper plot, the calculated ionisation profile for the EPOCH input is compared to the HYADES output on the lower plot. This profile is constructed using two sets of ion species (with both 65% oxygen and 35% silicon ions in both ion sets), the first set (red) consists of fully ionised ions, whilst the second set (green) are doubly ionised, the overall electron density is also shown (blue).

The results from this setup are seen in Fig. 5.14. There is a significant difference in temperature profile at higher densities where collisional ionisation is switched on compared to both fully ionised and field ionisation simulations. The region at the pre-pulse generated shock front, $x \sim 45$ μm, shows a significant thermal gradient. At $x < 45$ μm significantly higher temperatures along with a much larger electron density is seen with collisional ionisation switched on. In contrast to this, in the region $x > 45$ μm, a much lower temperature is seen, leading to a drop of $80eV$ in the ion temperature in a region slightly less than 1 μm in size.

A small temperature spike is observable at 39 μm (at 11 n_{crit}), at the same point as a sharp rising gradient in the doubly ionised ion density (see Fig. 5.13). While this peak is of a significant size, it is a deeper point into the target than the probe is able to reach, i.e. beyond the probe density surface, and so only outwards

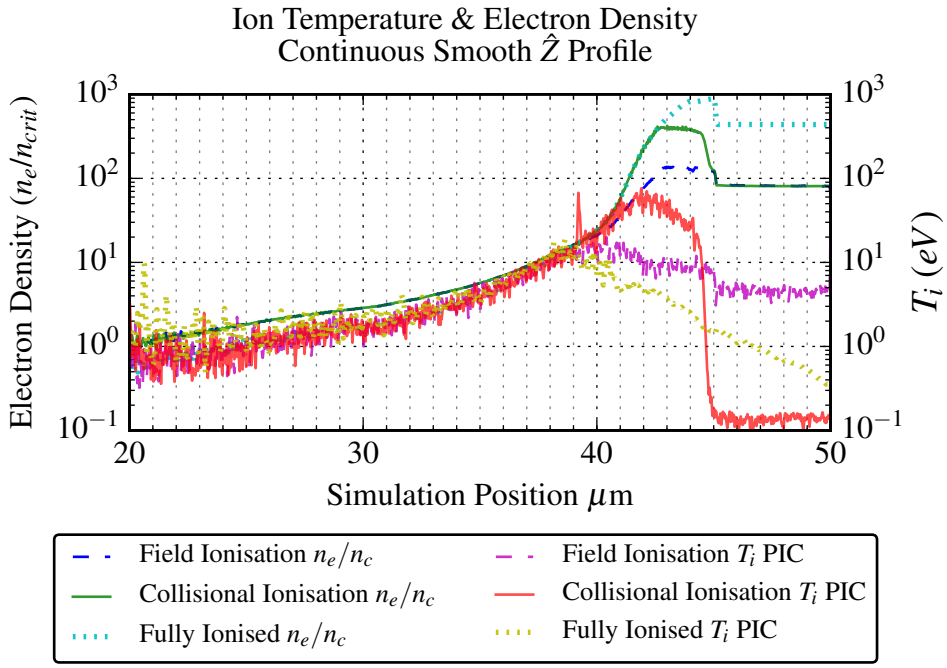

Figure 5.14: Plots of electron density and ion temperature taken from EPOCH calculations using input described in Fig. 5.13. There are three EPOCH calculations shown: the first (dashed lines) uses collisions and field ionisation, but not collisional ionisation; the second set (continuous lines) uses collisions, field ionisation and switches on collisional ionisation, the third set (dotted lines) shows results from a simulation using a fully ionised plasma where no ionisation model is used.

motion is likely to be observed as a result of its presence.

While such a sharp perturbation might account for the experimental results, the occurrence of such a perturbation requires a very steep density gradient in a low ionised species at around the critical density, which is unlikely to be realistic. The spatial distribution of differing ionised species is likely to be somewhat smoother prior to the shock front than is setup in the simulation above. The reason there is a sharp gradient in the doubly ionised species is simply due to the way the PIC code is set up. A larger number of different ionisation states modelled in the initial set up is more likely to result in shallower density gradients for each species (except, most notably, around any pre-existing shock front).

5.2.4.5 EPOCH Profile 3, Altering Density Scale-Length

Given that the FWHM of the focal spot is previously stated to be 14 μm and that HYADES calculates a pre-plasma, as a result of the 10^{13} Wcm^{-2} pre-pulse, that extends for more than 100 μm with a density of $\sim 0.1 n_{crit}$, it is likely that a 1D description of the pre-pulse interaction is insufficient. The HYADES code can be run with a variety of symmetries, two of which are relevant to this situation, planar slab-like geometry, and spherical geometry. The planar geometry has been used through all of the HYADES simulations up to this point, whilst changing the symmetry would be expected to change the resulting pre-plasma scale-length the result is complicated by the spherical symmetry of the laser driver and the total length of the initial target box. In the case of spherical symmetry the simulation box is a radial line out of a spherical target with a radially symmetric driver, whilst it is possible that the density of the blow-off at low densities drops off more quickly in that scenario, simply changing the geometry from planar to spherical is unlikely to produce a significantly different result without also changing the length of the

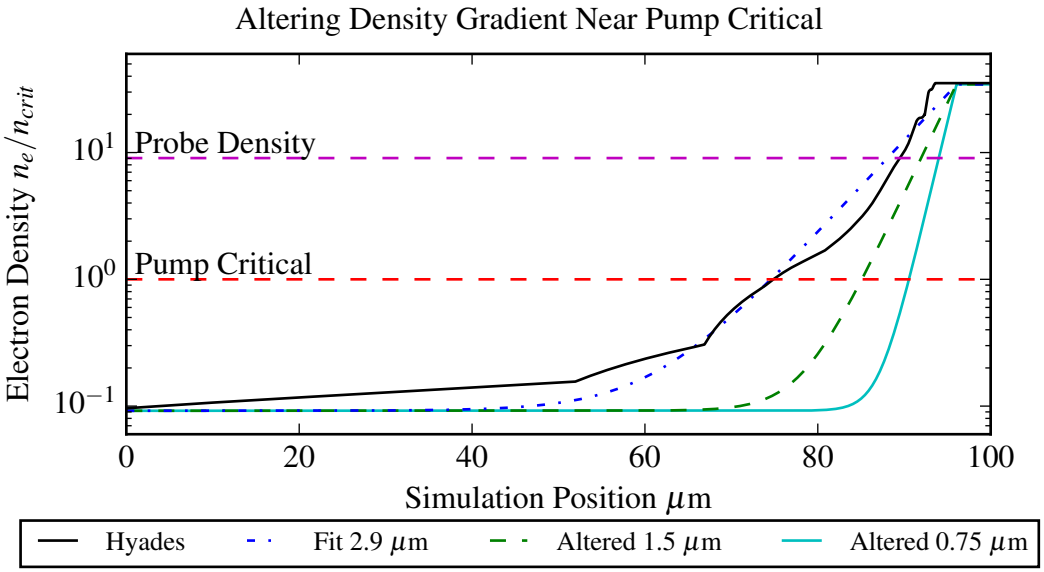

Figure 5.15: Electron density profiles from HYADES (black line), and several fit functions following Eqn. 5.1. L is the gradient scale length and is altered from 2.9 μm (dot-dashed line), through 1.5 μm (dashed line), and 0.75 μm (cyan continuous line). These density profiles are then used in further EPOCH simulations.

simulation box, and so this methodology is impractical to use effectively. A fit to the planar geometry HYADES ion density output can be made with the form:

$$n_i = n_{max} exp\Big(\frac{-(x-c)}{L}\Big) + n_{base} \tag{5.1}$$

Where x is the position along the x-axis, or simulation box, and L is a length-scale, and c is the peak position. Fig. 5.15 shows a fit made using Eqn. 5.1, a length scale L of 2.9 μm along with two other profiles based on this fit but with $L = 1.50 - 0.75 \mu$m

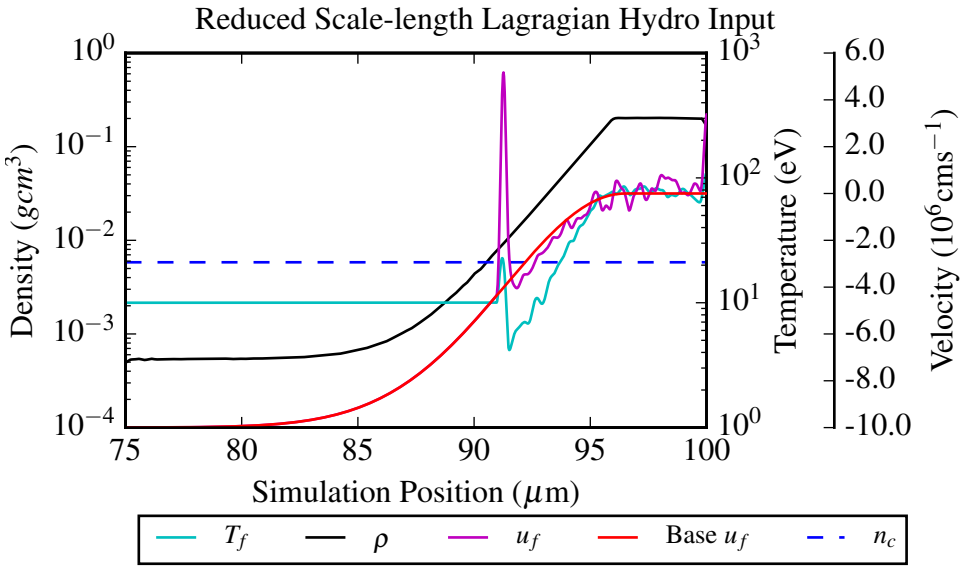

Figure 5.16: Plot of input profiles for Lagrangian hydrodynamics calculation. Density profile (black) calculated from fit described in Fig. 5.15, with critical density (dashed blue) calculated for fully ionised plasma. A base velocity profile (u_f, red line) is calculated from a fit to HYADES output using with the fitted scale length L then halved. The ion velocity profile (u_f, magenta line) taken from an EPOCH calculation, with EPOCH values set to zero before the critical density, is added to the base velocity for the final input into the hydrodynamic calculation.

The distance between the pump critical density to the probe critical surface for the planar geometry simulation is 15 μm, with distances of 6.9 μm and 3.4 μm for the profiles with the reduced scale lengths of 1.5 μm and 0.75 μm respectively. A shorter distance between the probe and pump surfaces will result in a shorter arrival time at the probe surface of any shock-like phenomena produced at the pump critical

density, but a shorter scale-length around the pump critical density may result in a larger shock velocity. To test whether a shorter density scale-length will generate a shock-like perturbation that matches the experimentally measured values another EPOCH simulation is run with the density profile with $L = 0.75\mu$m. To simplify the simulation the ions will be set so that they are fully ionised and $n_e = \hat{Z}n_i$, with n_i split so that $n_i = 0.35n_{Si} + 0.65n_O$. Given that the scale length is significantly shorter it is possible to run a simulation with a shorter box of length 25 μm and so a smaller cell size of $dx = 2.5$ nm can be used. The probe-critical surface velocity evolution can

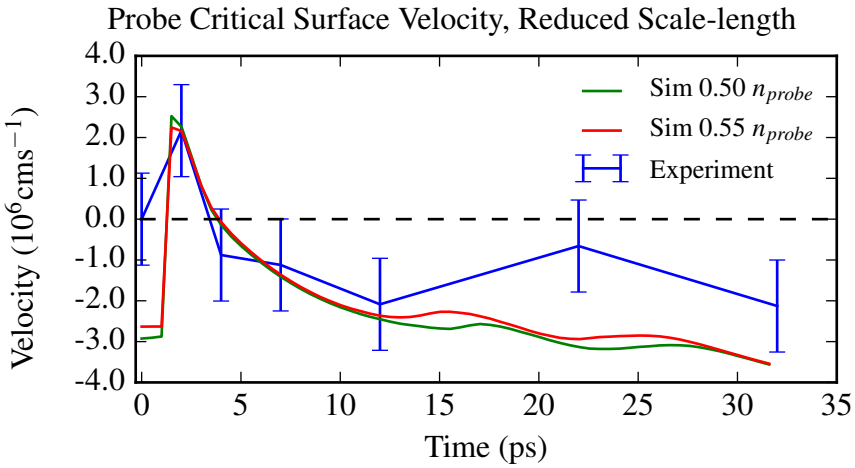

Figure 5.17: Probe critical surface velocity vs. time for Lagrangian hydrodynamics calculation, using input described in Fig. 5.16, compared to experiment. The probe velocity is calculated from the velocity at 50% and 55% the probes critical density surface.

now calculated by putting in the temperature/velocity profiles into the Lagrangian hydrodynamics code. As the density profile is created via a modification of a fit from HYADES the velocity profile must also be created. As the pre-pulse generated shock is not simulated in this setup the velocity profile will only deal with the expansion from the rear of the pre-pulse shock front. A fit to the HYADES planar calculation is made to the velocity profile in a similar fashion to the previous fit using the ion density profile, however a semi-Gaussian profile rather than an exponential is used

for the fit:

$$v_f = v_{min} exp\Big(\frac{-(x-c)^2}{L^2}\Big) + v_{min} \tag{5.2}$$

Where x is the position along the simulation box; c is the peak of the Gaussian, and also where the semi-Gaussian splits into a constant output of value $v_{min} = 0.0$. The density scale length is decreased by a factor of two from the original fitted value (the reduced output from this fit is seen in Fig. 5.16). The low density ($n_e < n_{crit}$) EPOCH velocity profile is ignored for this calculation and the temperature profile at the same lower densities were set to a constant 10 eV. The probe critical surface velocities calculated can be seen in Fig. 5.17, to match the experimental values the velocities for a critical surface approximately 50% less dense than the probes density is used. Whilst Fig. 5.17 shows a good match to experiment, the reduction

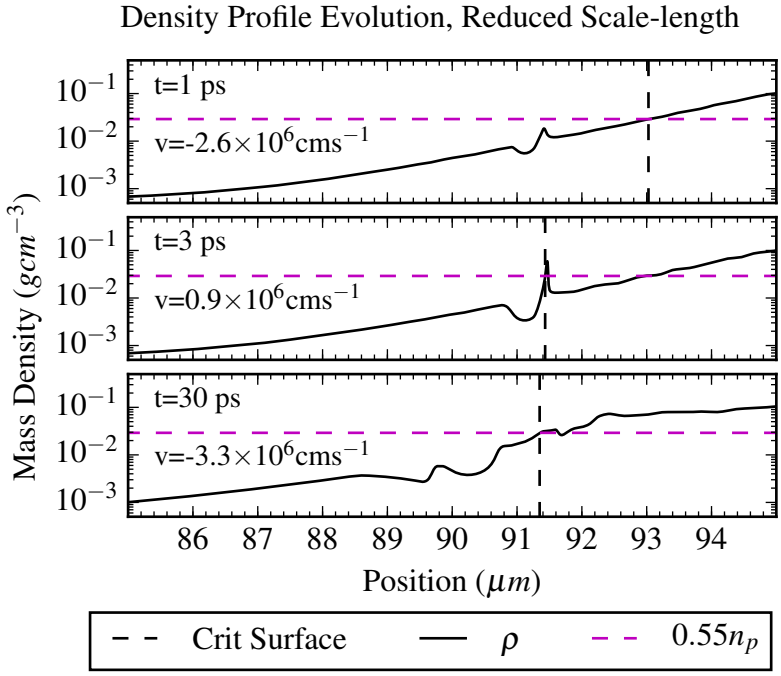

Figure 5.18: Plot of density from Lagrangian hydrodynamics calculation using input described in Fig. 5.16, density profiles taken at t = 1, 3 and 30ps. Early time profile, at 1 ps, shows a probe critical surface beyond formation of shock, showing expanding target bulk (-26 kms^{-1}) followed quickly by probe critical surface occurring at shock peak showing a motion inwards towards target bulk at 3ps. Later time profile, at 30 ps, shows passage of a compression wave past the probe density (seen as a peak at ~ 93μm), with the probe density surface showing an expansion, or velocity away from the target bulk.

in the probe critical surface density implies that the density scale-length in the higher density region is not modelled well and may well be even steeper in this region ($n_{crit} \rightarrow 10n_{crit}$) than the reduction to a scale length of $0.75\mu m$ implies. That the Lagrangian hydrodynamics calculation only matches with the under-dense velocity/temperature perturbations removed indicates that the density scale length in the under-dense region immediately behind the critical density surface is likely considerably shorter than $L = 0.75\mu m$, similarly to the over-dense region.

The evolution of the density profile from the Lagrangian hydrodynamics calculation is plotted, in the form of three snapshots, in Fig. 5.18. The perturbation produced in the PIC code appears to travel only a small amount in the 34ps that the simulation is run, less than a μm, while it does produce a strong shock front initially (visible in the 3ps snapshot in Fig. 5.18) this shock front does not stay strong throughout the simulation run.

5.3 Conclusions

5.3.1 Interpretation of Experimental Results

There are several possible hydrodynamic or kinetic phenomena that could account for the Doppler-shift results seen in Fig. 5.2. It is worth noting that all of the hypothesis described below rely on the assumption of the same probe pulse reflectivity behaviour, that the probe-pulse travels unaffected through the pre-plasma to the $n_{3\omega}$ density surface where it reflects. The measured Doppler shift of the probe being due solely to the motion of the $n_{3\omega}$ density surface. The first possible scenario is the phenomena observed in the last chapter, where a shock is formed from a perturbation at, or close to, the critical density (e.g. from the velocity perturbation observed in the previous chapter) which then travels through the over critical density region before passing through the probe density surface. The distance between n_{crit} and

the probe density, $n_{3\omega}$, is key to testing this description. There is a very small time between the first and second data points (2 ps) for such a perturbation to travel between these two locations. At a constant velocity of $2{\times}10^6$ cms^{-1} the distance that could be traversed is very small: 0.04 μm. This would clearly require a very steep density gradient, however it is very unlikely that the shock will travel at a constant velocity. If the perturbation started at a larger but decreasing velocity this would weaken the requirement for the steep density gradient. Another possible factor is compression due to the passage of a strong shock. In an ideal gas a compression by a factor of 4 can be expected in this case (given a γ = 5/3), and so a strongly compressive shock would be visible to the probe much earlier due to the density increase.

The second possible explanation of the phenomena observed in the experimental results is a localised absorption of energy transferred from the critical density, possibly in the form of a warm electron population whose energy is collisionally transferred to ions at a location close to the probe density. The switch from inwards to outwards motion observable in the experimental results between 2-4 ps (see Fig. 5.2) would require this absorption to be very localised and at significantly lower densities than is seen in EPOCH calculations (see Fig.5.14).

A third possible explanation lies with ionisation causing a localised change in n_e so that motion detected at one point is occluded by plasma, that has gained free electrons from ionisation, moving in a different direction.

Of the three hypothesis described above; the first, describing a shock formed at the critical density travelling through the over-critical probe density, seems the most likely possibility, especially as the results from modelling a steeper density gradient lie within the experimentally obtained results (see Fig. 5.17). The second hypothesis, describing a localised over-critical absorption, is a phenomena likely to happen too deep into the target for a probe monitoring a density surface at $9n_{crit}$ to see. No such phenomena is observable in the PIC results (see Fig. 5.14). The

third hypothesis being an alteration of the local electron density via ionisation is unlikely to be the cause as there is a significant amount of ionisation that happens on a time-scale far too short (extremely quickly due to fast electron propagation through un-ionised or low-ionised material) to be a cause of a significant change in the direction of motion over 4ps (as shown in Fig. 5.14, the plasma is mostly fully ionised up to the pre-pulse generated shock front).

5.3.2 Shock Propagation

The long term evolution of a shock-like perturbation in a dense fluid, modelled via an ideal gas Lagrangian Hydrodynamics calculation, (shown in Fig. 5.18) does not appear to show a shock travelling significantly far into the main bulk of the target. This may be due to a number of effects already described in the conclusion to the last chapter. The temperature profile used in the Lagrangian code shows significant heating deep into the pre-pulse created shock, this is largely due to deposition of energy from fast electrons produced in the sub-critical region. It seems likely that the difference in later behaviour of these shocks in the Lagrangian calculations compared to the HYADES calculations, is more to do with the locations the energy is deposited in HYADES as compared to EPOCH. The HYADES outputs do not show the same amount of heating from warm electrons deeper into the target than that observed in the PIC calculations.

The PIC code results show a significant amount of energy deposition in the low density regions of the plasma blow off. Once the laser has passed through the low density regions there is an interaction of the laser pulse with the plasma at the critical density which accelerates electrons. After these electrons are accelerated they leave this region and deposit the energy some distance away from the critical region. This leaves a deposition which has a velocity perturbation with a small temperature rise at the critical region. This velocity perturbation causes a shock-

like phenomena to travel into the target. This shock-like phenomena has to travel through a significantly hotter dense region of the target which is thermodynamically expanding outwards so the shock does not propagate significantly into the target bulk.

5.3.3 Further Work

There are some improvements that can be made to the simulation technique described here. Of the three main stages of modelling, Radiation-Hydrodynamics for the pre-pulse, Particle-in-Cell for the main pulse, and hydrodynamics for the late time evolution, the most notable improvement required is exchanging the use of a 1D Radiation Hydrodynamics code for a 2D Radiation hydrodynamics code. There are several possible choices available for this, the suitable candidates include (but are not limited too): H2D,[161] a 2D Lagrangian code which has a similar set of models available to those available in HYADES, and is produced by the same company; FLASH[135] is a 2D Eulerian code with an adaptive mesh, which also comes with a similar set of models as available in HYADES. A full 2D approach may be necessary for the EPOCH particle-in-cell modelling as well, the lateral spread of the energy deposition may have a significant effect on the temperature of the bulk and so could have an effect on the progression of a shock formed in the critical region through the over-dense material. The simple hydrodynamics code would most easily be improved by adding in facilities for using alternative equations of state and possibly an ionisation model. Radiation transport is only likely to be useful if the material is heated very significantly by the pre-pulse, or if the material has a particularly high Z.

Chapter 6

Low Density Foam Target Doppler-shift Spectroscopy and Shockwave-Velocity Measurements in a High-Contrast Laser System

6.1 Introduction

This chapter describes a 3ω Doppler-shift spectroscopy experiment using an ultra-low density TMPTA foam target, with a similar setup to that described in Chapter 4. The density of the foam target, at 30×10^{-3} gcm^{-3}, is larger than the pump critical density of 5.5×10^{-3} gcm^{-3}, whilst still smaller than the probe critical density of 50×10^{-3} gcm^{-3}, so that $n_{crit} < n_{foam} < n_{3\omega}$. The hydrodynamic evolution of over-dense foams has been the subject of considerable study in the longer pulse regime ($t_{main} > 1$ ns) and with intensities between 10^{13-15} Wcm^{-2} (see references 162–167), the production of shock-like perturbations by ultra-short ultra-intense laser pulses is less well understood. Such phenomena could have impacts on possible use of foams in fast particle and X-ray production.[168,169]

The section 6.2 describes the novel details of the foam pump-probe experiment and a description of the foam target, followed by an analysis of the collected probe spectra and the Doppler shift temporal evolution. Section 6.3 describes modelling of the pre-pulse foam interaction, as well as a description of the results for the radiation-hydrodynamics modelling for the full intensity profile. Section 6.4 discusses several attempts to model the main-pulse interaction with the EPOCH particle-in-cell code.

6.2 Foam Target Pump-Probe Experiment

The same pump-probe experimental setup as described in section 4.2 is used again in this experiment, with the exception of the target type. The temporal intensity profile of the 100 TW laser system can be seen in Fig. 4.1, with a 500 ps contrast of $\sim 10^7$, the laser intensity is set to $I_l = 9.5 \times 10^{17}$ Wcm^{-2} and is focused to a spot size of 14 μm diameter using an f/3 off-axis parabolic mirror at an angle of incidence of 40°.

6.2.1 TMPTA Foam Target

The foams are formed by polymerisation in-situ[168] from a polymer TriMethylol Propane TriAcrylate (TMPTA, $C_{18}H_{20}O_6$). The foam consists of 36.59% carbon atoms, 48.78% hydrogen atoms, and 14.63% oxygen by number, or 60.81% carbon, 6.80% hydrogen, and 32.39% oxygen by mass. The foam has a density of 0.03 gcm^{-3}, which, if fully ionised ($\bar{Z} = 3.85$), gives an electron density of 9.64×10^{21} cm^{-3} (equivalent to $5.5n_{crit}$). The fully ionised electron density is smaller than the probe-critical density $n_{3\omega} = 1.6 \times 10^{22}$ cm^{-3}, which would allow the probe pulse to pass through the foam with little or no reflection if the foam were a uniform density. The foam has some microscopic structure (characterised using the process described in Ref. 170) consisting of pores $\sim$ 900 nm in size with a distance between pore centres of approximately 1400 nm. If some of the foam were to remain intact through the pre-pulse

then it is possible that the probe could interact with a plasma up to four times higher than the macroscopic density. However, this scenario is unlikely if there is a significant compressive shock formed by the pre-pulse.

6.2.2 Analysis Techniques

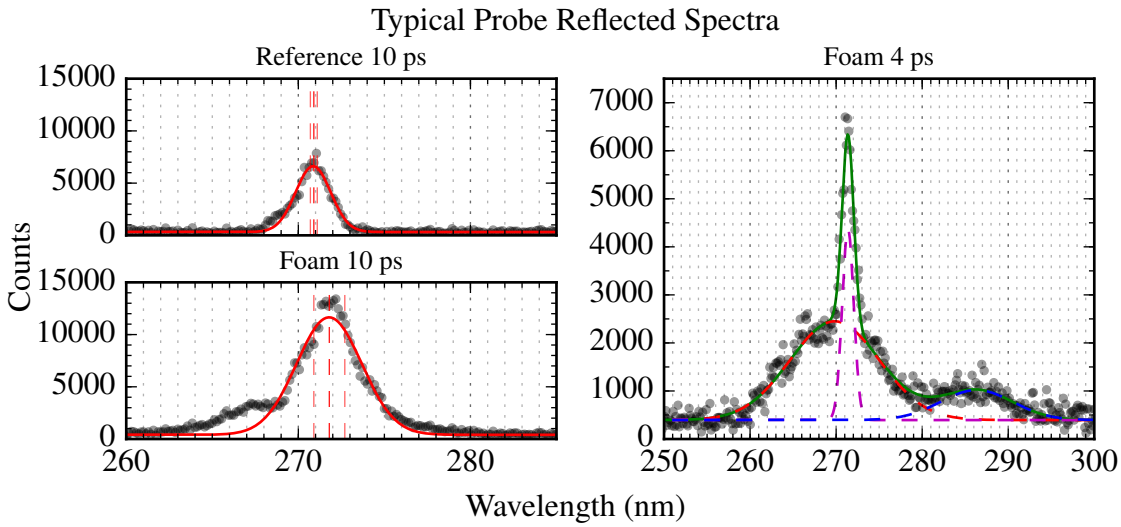

Figure 6.1: An example of several probe reflected spectra including fits used to determine the peak wavelength. The top left plot shows a reference spectra from the probe reflecting off the frame, with an exponential fit (red) and vertical dashed lines indicating the peak wavelength and fitting errors. The bottom left shows the spectra of a 10ps delayed probe, with an exponential fit and peak wavelength with errors. The right plot shows an example of a 4 ps delayed reflected probe spectra with multiple peaks, the green indicates the summed peak fits, with the individual peak fits shown as dashed lines coloured red, magenta, and blue.

Sample results from the experiment are shown in Fig. 6.1. The probe spectra (seen in the top left plot) has very narrow spectral width $\Delta\lambda = 0.9 \pm 0.2$ nm. A typical reflected spectra of a pump-probe shot can be seen in the bottom left of Fig. 6.1. This shows a significantly wider and red-shifted peak, with an additional wider base on the shorter wavelength side of the peak. On several occasions, most notably during the experiments with a 4 ps and 20 ps delay setting, more than one peak is observed: with a wider base peak; a sharp narrow peak and a highly red-shifted smaller peak. An example of results with multiple reflections is shown in the right

plot of Fig. 6.1.

To obtain a value for the spectral location of each of the spectral peaks from the probe's reflected-spectra, first a noise baseline with and amplitude of A_b is fitted to the noise floor. Once the noise floor is found the data is fitted to a function of the form:

$$f(\lambda) = A_b + \sum_n A_n exp\left(\frac{(\lambda - \Delta\lambda_n)^2}{\sigma_n^2}\right) \tag{6.1}$$

where $\Delta\lambda_n$ is the spectral location of the n^{th} peak, A_n is the amplitude of the n^{th} peak, and σ_n is the spectral width of the n^{th} peak. The minimisation routine used for fitting the function above to the experimental data is the 'curve fit' routine from the Python SciPy package, which uses a least squares minimisation routine. The number of peaks is set to a fixed value for fitting, and their approximate location (judged by eye) is used as initial values for the minimisation routine. An example of a fit with multiple peaks can be seen in Fig. 6.1.

At least four reflected spectra are gathered for each delay-stage setting. For each foam-reflected spectra gathered, a reflection of the probe onto the frame housing the foams is also gathered as a reference spectrum. In the spectra with multiple peaks the peaks can be broadly separated into three groups: a group with a very large positive Doppler shift (12 nm to 18 nm, i.e. a large red-shift); a group with a moderately large negative Doppler shift (−0.76 nm to −2.5 nm,i.e blue-shifted); and a group which appears to follow a similar trend to earlier experiments with smaller Doppler shifts. To calculate the red/blue-shift of a probe-foam reflection, the spectral location of the probe-*frame* reflection is used as the initial wavelength, so that $\Delta\lambda = \lambda_{foam} - \lambda_{frame}$. All the $\Delta\lambda$ values for each delay setting (separated into groups as appropriate) are used to calculate an average red/blue shift for each group at each delay setting. These average values are shown in Fig. 6.2. There is a significant amount of variation in the Doppler shift of the probe reflection from shot-to-shot for the same delay setting. This shot-to-shot variation is significantly

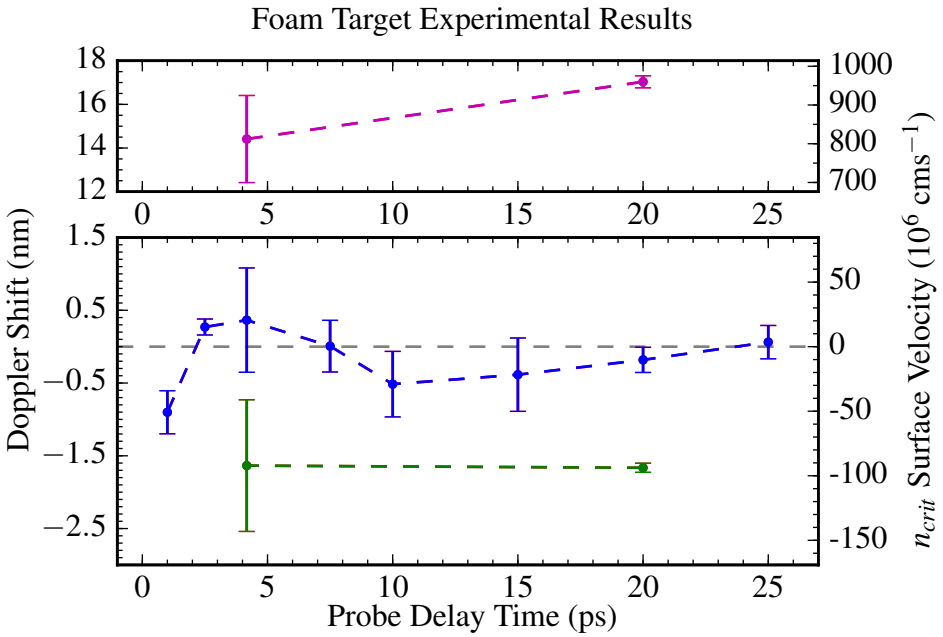

Figure 6.2: Plot of the shot-averaged Doppler shift, a blue shift (a reduction in λ) would indicate a surface travelling towards the spectrometer. The results are subdivided into three sets, the blue set indicate the peaks with the least deviation from the probe wavelength, green have a large red-shift, and the magenta set have a very large blue shift. The calculated probe-surface velocity is denoted on the right hand axis of both plots. Here the positive velocity direction was chosen so that it represents material flowing towards the target surface and away from the spectrometer, while material ablating away from the target surface would have a negative velocity.

larger than both the spectral width of the peaks from the probe-reflected spectra and the error from fitting, and so the standard error from the shot-to-shot variation is used to calculate error bars for the resulting time evolution of the reflected probe Doppler-shift. Whilst the error bars shown in Fig. 6.2 are very large, there is still a visible trend: an early time outward motion of approximately $40{\times}10^6$ cms^{-1}; followed by an inwards motion between 2 and 6 ps (though this could vary significantly given the large variation in the data at 4 ps); and then finally an outwards motion is observed gradually falling back down towards zero velocity between 10 and 25 ps.

An additional delay setting is also used in an attempt to characterise the pre-plasma conditions, the delay stage is set to −20 ps, i.e. 20 ps before the impact of the main pulse. The measured Doppler-shift of the negatively delayed probe reflection is

measured at (0.39 ± 0.54) nm with a corresponding velocity of (22 ± 30) $\times 10^6$ cms^{-1}.

The results in blue on Fig. 6.2 are possibly Doppler-shifted as a result of a similar hydrodynamic process as seen in the last two chapters, i.e. a shock-like phenomena travelling through an over-dense plasma. However, the larger wavelength shifted results are unlikely to be the result of Doppler-shifting from reflections off moving over-critical plasma, simply due to the much larger Doppler-shifting in both cases. Whilst there is likely to be material travelling at high speeds away from the target in the blow-off region, this material is unlikely to be dense enough to affect the probe-pulse. However, depending on the scale-length and collisionality of the pre-plasma, there maybe other phenomena that can account for the shift in wavelength observed.

6.3 Radiation-Hydrodynamics Modelling

A foam with a macroscopic electron density n_m (considering the foam to be fully ionised) consists of pores which are either empty or have a density $n_{pore} << n_m$ and strands with a density $n_{strand} > n_m$. The size of the pores and the fractal-like structure of the foam dictates the density of the strands. A more fractal-like structure will lead to narrower denser strands. The very early time pre-pulse foam interaction will form a highly non-equilibrium plasma consisting of ablating strands and pores filled with hot low-density plasma.[165] The time taken for this plasma to equilibriate will depend on the transfer of energy from the pre-pulse through the forming plasma and how quickly a shock-like phenomena forms. If the plasma is under-dense for the majority of this interaction then the foam could heat volumetrically to form a large non-equilibrium plasma.[163,171] If the target ionises quickly to an over-critical density then the heating process is likely to be dominated by the formation of a shock-like phenomena forming around the critical density region, similar to the behaviour seen in homogeneous targets. At higher

intensities (10^{13-14} Wcm^{-2}) the absorption of laser light into foam targets is likely to be significantly altered, with much higher absorption than solid targets.[164] At later times, in cases with high intensity, greater penetration of the laser would lead to the formation of a cavity inside the foam.[165] It is not clear if these effects are likely to take place at lower intensities and at timescales shorter than 1 ns. With a pore-like structure on the front surface (scaled at ~ 900 nm) that has a similar scale to the pump wavelength (800 nm) and so it is also possible that surface effects could play a part in laser absorption.[172]

Since the target is ~ 50% hydrogen atoms by number and the target has a macroscopic density ~ $5n_{crit}$ if fully ionised, it is possible that the target ionises quickly enough to a density > $2n_{crit}$ that it might be possible for the foam-like structure to behave in a similar way to a homogenous low density target. Several attempts to simulate the early time foam behaviour have been made as a part of this investigation using 2D PIC simulations (using a similar approach to the 1D calculations done in other studies[169]).

The foam structure can be emulated using a regular grid of circular voids set inside a homogeneous background material adjusted to keep the macroscopic density the same as the TMPTA foam. Different levels of fractal-like structure can be achieved by adding grids of smaller voids inside the larger homogeneous background, and adjusting the background density so that the macroscopic density matches the original foam. However, a significant difficulty arises due to the fact that the PIC code has to be run for more than 20-50 ps in order to see any significant deformation or ablation of the foam strands. This long time requirement means that the number of particles per cell has to be reduced to a very small number in order to make the computation possible, which results in noisy, non-convergent results. Another problem with this approach is that the field-ionisation model used in EPOCH appears to be insufficient to simulate ionisation at very low intensities, as the PIC simulations results show little to no ionisation at laser intensities of

$I_p = 10^{11}$ Wcm^{-2} .

6.3.1 Radiation Hydrodynamic Calculations

Whilst the PIC calculations described above cannot predict the behaviour of the foam at early times, an alternative approach using HYADES can be taken. The alternative to the PIC approach is to approximate the structure of the foam in 1D using a target setup as layers of high and low density material.[162] This approach can then be compared to a simpler setup where the foam is assumed to be homogeneous.

The same 100 TW laser system is used here as in section 4.2 along with the contrast and intensity settings, so that the laser intensity profile from section 4.3.1 can also be used. An average-atom LTE ionisation model is used as in previous sections along with the polystyrene equation of state from record 7592 of the SESAME library. The multi-group radiation package is used with 100 photon groups from $10^{-3} - 10^{-1}$ eV up to 10 keV, the same set up as shown in Fig. 4.4, with the corect atomic ratios for the TMPTA foam. The laser solver uses parameters of λ = 800 nm, $\theta = 40°$, and plane polarisation, consistent with experimental setup. Both the Helmholtz and the Fresnel solver are used. The flux-limited thermal conductivity model is used, the range of values tested is varied between 0.6 and 0.05. The extra transport allowed by a higher flux limiter may offer a better description of the foam target dynamics given the possibility of greater penetration by the pre-pulse laser.[163] The initial mesh used for these calculations is a uniform grid of 1000 cells, 0.5 μm thick. While a uniform grid of this type might lead to greater mesh distortion at later times, it significantly simplifies the creation of structured targets in 1D. A target with a modulated density is shown in Fig. 6.3. Unfortunately there are a number of hard coded limitations in HYADES which restrict the types of structured target that can be created, and so only a small section of the front surface of the target is structured. These limitations also constrain the density gradient between

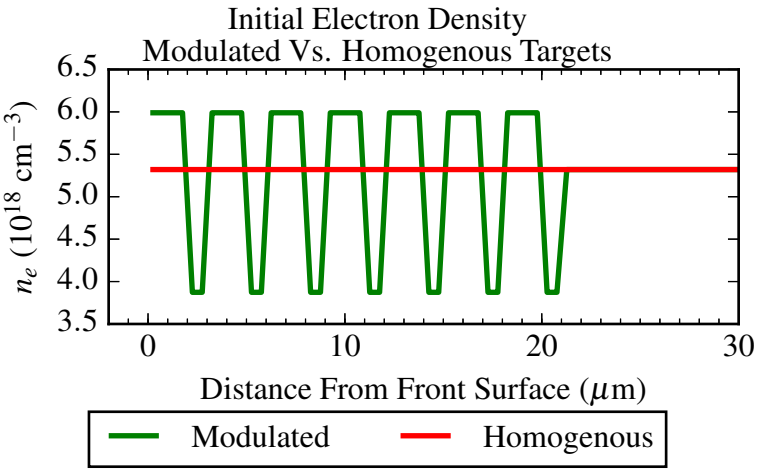

Figure 6.3: Plots of the initial electron density used in the HYADES calculations. The red line shows an assumed homogeneous density with the mass density set to the average density. The green line shows a modulated density with pores 900 nm in length and with bulk sections 1400 nm in length. To avoid numerical errors the pores were set with a density of around 70 % of the macroscopic density whilst the bulk is set to 115 % of this density. Due to several hard coded limitations in HYADES only the first 21 μm are modulated.

the low and high density regions, as to avoid numerical errors neighbouring cells cannot have significantly differing masses (by more than 50 %), therefore in order to have steeper density gradients between cells, a larger number of small cells is required.

6.3.2 HYADES Calculation Results

A comparison of the time evolution of the electron density and fluid velocity is shown in Fig. 6.4. As can be seen in the figure there is very little variation in the pre-plasma formation between homogeneous and modulated target profiles, with a long scale-length pre-plasma forming and a large compressed shock front travelling at approximately 5×10^6 cms^{-1}, which does fit in with the range of measured values for the negatively delayed probe pulse. There are several similar features that can be seen when comparing the experimental measurements to the probe-surface velocity calculated in HYADES simulations (shown in Fig. 6.5). At low flux-limiter values of 0.05, a large inward motion can be seen at 5-10 ps. This inwards motion has

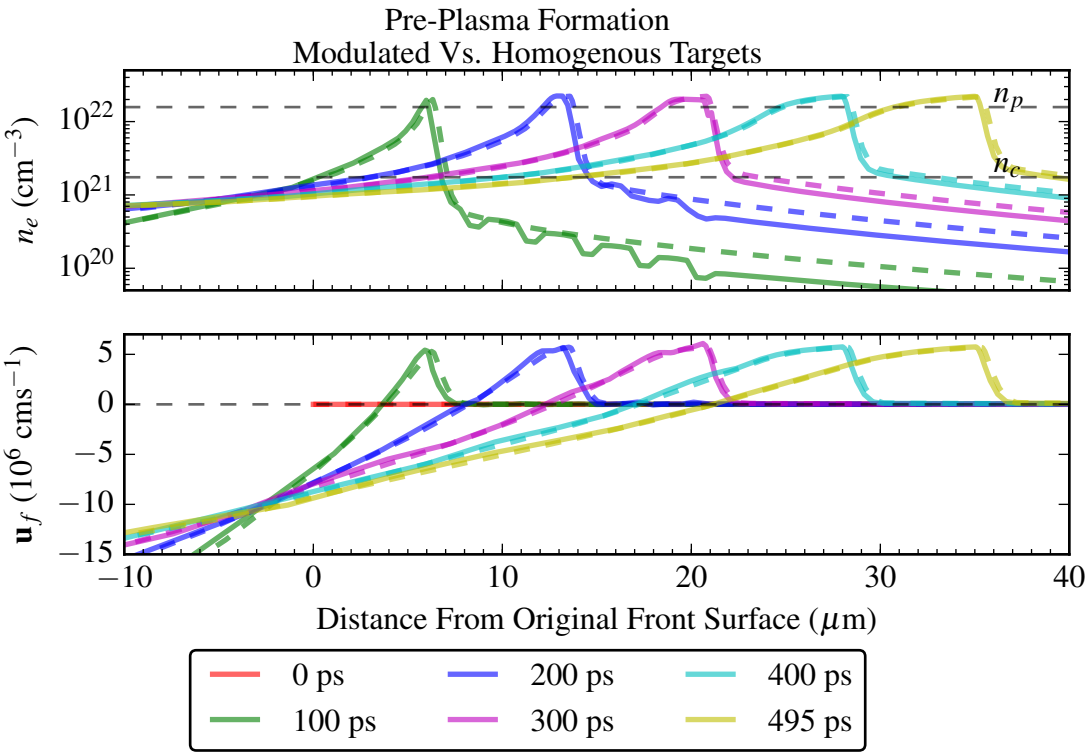

Figure 6.4: Comparison of the pre-plasma formation for the homogeneous and the modulated target profiles, HYADES uses a Fresnel absorption model along with a flux limiter of 0.3. Top figure: plots of electron density at varying times with dashed lines showing data from the homogeneous target calculations and solid lines from the modulated target calculations. Bottom figure: plots of the fluid velocity for the homogeneous target (dashed) and modulated target (solid) at several points in time. The times shown are from the beginning of the simulation; the central main intensity peak occurs at 500 ps.

a similar magnitude, though it is slightly later in time than the experimentally measured motion (observable at 2-6 ps). With higher flux limiters (0.1-0.6) the magnitude of this motion decreases significantly and a large outward motion is then observed. The later time trend ($t \gg 15$ ps) of the probe-surface velocity appears to change suddenly from an outward motion (upto -25×10^6 cms^{-1}) to an inward motion (upto $+25 \times 10^6$ cms^{-1}). This change is most visible at $t = 15$ ps and later in the simulations using flux limiters of 0.3 and 0.6. To understand exactly what is happening when a sudden change in probe-surface velocity occurs, it is useful to look at the electron density and fluid velocity as a function of time after the main pulse interaction. Results from one simulation can be seen in Fig. 6.6. It is possible

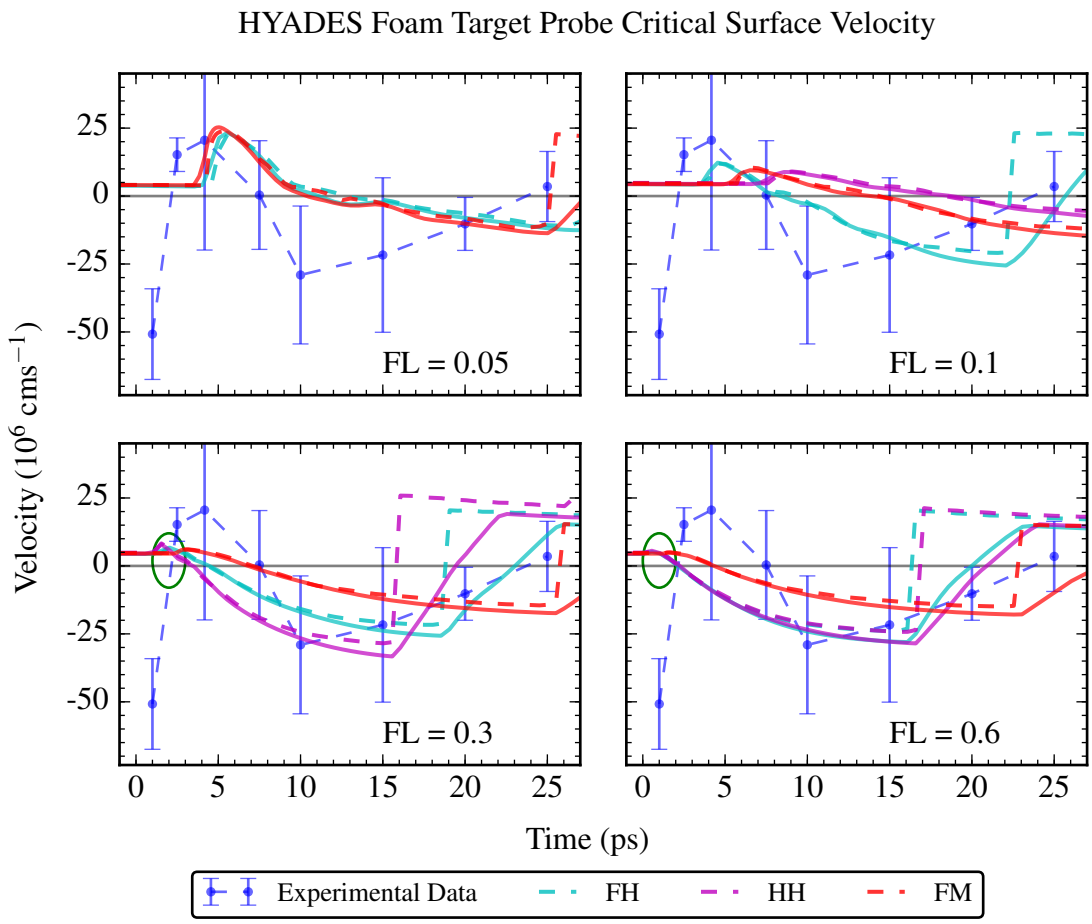

Figure 6.5: Plots of probe-surface velocities calculated from the HYADES simulations compared with the experimental results. There are three HYADES set-ups, the first two compare a Fresnel reflectivity model (F H, light blue) with the Helmholtz solver (H H, magenta), both with a homogeneous target using the macroscopic average density. The third model uses the modulated density profile with a Helmholtz solver (H M, red). The set-ups are run with differing values of the flux limiter (denoted FL on the plots). The green ellipse highlights a small inwards perturbation that is visible in the modulated density outputs. The dashed lines indicate that the critical surface velocity is taken at a density of exactly the probe critical, the solid lines show an average taken from 70-100% of the probe density.

that the probe will interact with material slightly less dense than the probe critical density, if there is enough material at that density in front of it. For this reason an average velocity of density-surfaces between 70% and 100% of the probe-critical density can be calculated, and is plotted as solid lines in Fig. 6.6.

The cause of the sudden switch of negative velocity to positive velocity can be seen in subplots C and D. In these plots there are two peaks visible in the

electron density, at $x \simeq 30$ μm and $x \simeq 42 - 46$ μm. Initially the probe is reflecting off a surface on the first peak, which is travelling away from the target bulk. After some time this peak has decreased in density below the the probe-critical density and the probe reflects off the peak in electron density travelling into the target bulk.

The cause of the break of the pre-pulse generated shock is due to the fast moving shock produced in the main-pulse interaction. This large fast moving shock then travels *through* the pre-pulse formed shock, after which the density of the pre-pulse formed shock decreases dramatically.

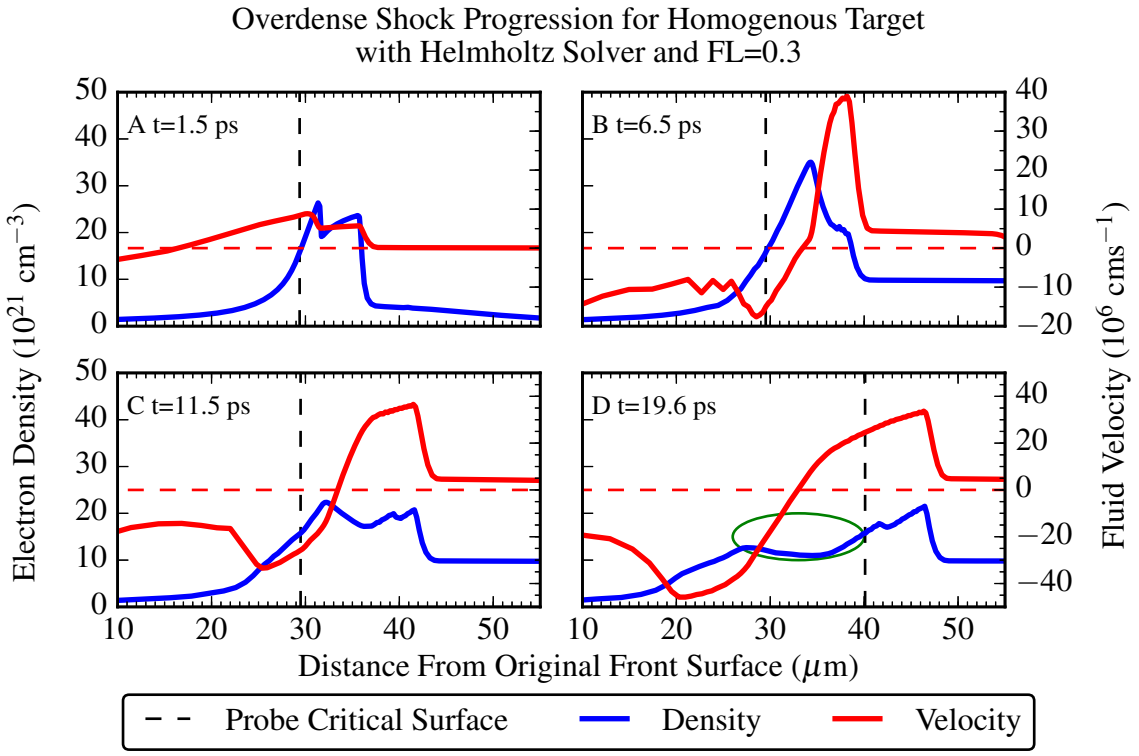

Figure 6.6: The electron density (blue) and fluid velocity (red) data taken from a HYADES calculation using a homogeneous target, a flux limiter of 0.3 and a Helmholtz laser absorption model. The probe-critical-surface location is shown as a vertical black dashed line. The first plots shows a shock (located at 31 μ**m**) that has formed and passed through the probe-surface. The second plot shows the shock (37 μ**m**) after travelling through the pre-pulse generated shock front (32 μ**m**). The third plot shows the shock (42 μ**m**) travelling through the cold bulk target. The fourth plot shows the break up of the pre-pulse generated shock. A region of plasma close to the probe density is denoted using a green ellipse in the fourth plot.

6.3.3 Radiation-Hydrodynamics Conclusions

While none of the HYADES radiation-hydrodynamics calculations show all of the phenomena visible in the experimental results for an individual set value of the flux-limiter, there are some similarities in both the timing of some of the phenomena and magnitude of the velocities observable. At low flux limter values, there is an inward motion as a result of a shock-like phenomena travelling through the probe-surface. This inward motion is similar in magnitude (25×10^6 cms^{-1}), but occurs slightly later than in the experiment. While at higher flux-limiter values the early-time inwards motion is reduced to between 10×10^6 cms^{-1} and 5×10^6 cms^{-1}, with flux limiters of 0.1 and 0.3 respectively. However the main-pulse created shock is still visible in the electron density profile seen in Fig. 6.6 with a velocity at the probe surface of 20×10^6 cms^{-1} at later times, which is similar to the experimentally measured values at earlier times. The outward motion of the probe-surface at later times in the higher flux-limiter values (0.3 and 0.6) is also close to the experimentally measured values.

6.4 EPOCH Particle-In-Cell Modelling

6.4.1 1D Density Profile Selection

To further investigate the interaction of the high-intensity pulse with the front surface pre-plasma, two separate density profiles are obtained from the HYADES output. The first density profile is obtained directly from the HYADES simulation initialised with a flux limiter value of 0.3, and the modulated profile seen in Fig. 6.4 at a time t = 490 ps. The density profile is taken from the HYADES results 10 ps prior to the onset of the main pulse so that only the effect of the pre-pulse is taken into account. The second density profile uses a steepened version of this profile. This approach is taken as a shorter length-scale pre-plasma may be a better

approximation of the density profile in the experiment. The reason a shortened pre-plasma maybe more realistic is because a pre-plasma may have a more spherical expansion in reality. The density profile from a spherical expansion from a point will be steeper than for a planar expansion, with a given laser intensity profile. This profile is calculated by making a fit to the existing density profile and reducing the characteristic length-scale L. The best fit was found using the function:

$$f(x) = a + b\exp\left(-\frac{(x-d)^{\frac{1}{2}}}{L^{\frac{1}{2}}}\right) \tag{6.2}$$

where a is a minimum density, b is the maximum density, d is the location of the maximum density, and L is the characteristic length-scale. This function was chosen as the much longer decay of the density from the front surface was not well represented when using a Gaussian or super-Gaussian function. The density profile taken from HYADES and the fit to the profile are both shown in Fig. 6.7.

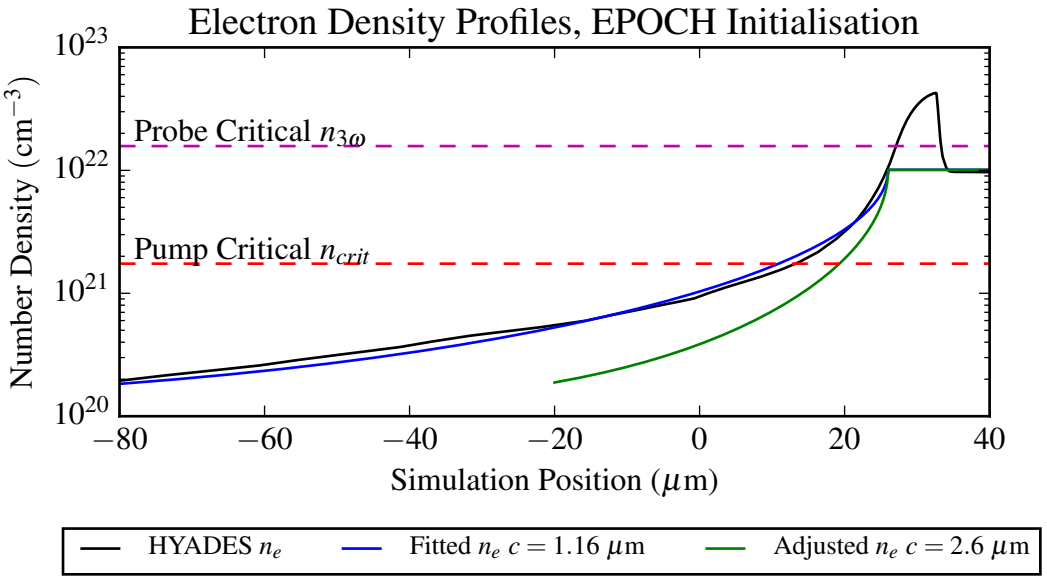

Figure 6.7: Plot of the density gradient taken from the HYADES simulation with a modulated initial density and a flux limiter of 0.3 taken 10 ps prior to the arrival of the main pulse. Plotted alongside the HYADES density gradient is a fit using eqn. 6.2, and a shortened profile based on this fit but with a shortened characteristic length scale.

6.4.2 EPOCH PIC Setup

Several simplifications are assumed for all of the PIC code simulations performed in studying the main-pulse foam-target dynamics. The first simplification is that ionisation is assumed not to have a significant effect, because the foam pre-plasma is seen in HYADES simulations, to be almost completely ionised up to the densest part of the pre-plasma shock front. The second simplification is that of using an average ion (with an atomic mass of $7.2m_p$ and charge of $3.85e$) rather than simulating multiple species of ions. This was necessary as it significantly reduced the number of particles required to achieve a convergent result. A cell size of 5 nm is used with 4000 particles per cell evenly divided between ions and electrons. Collisions were calculated using the automatic setting, which calculates a Coulomb logarithm based on local density and temperatures. The laser is set to an intensity of 10^{18} Wcm^{-2} and has a temporal FWHM of 30 fs.

6.4.3 EPOCH Results Analysis

6.4.3.1 EPOCH Results and Initial Hydrodynamic Calculations

Results from simulations using both the HYADES density profile and the shortened density profile can be seen in Fig. 6.8. Both of these plots are obtained at ~ 200 fs after the reflection of the main pulse. There are two groups of velocity perturbations visible in the longer scale-length pre-plasma (see Fig. 6.8b): a large perturbation around the $n_e \simeq n_{crit}/4$ and a much smaller perturbation around $n_s \simeq n_{crit}$. Around the same locations as both sets of velocity perturbations are temperature peaks. Leading up to the larger of the two temperature peaks is a region of heating, which appears to be a part of the phenomena leading up to the larger of the two velocity peaks, and will be explored in the next section.

The larger of the two sets of perturbations is visible in both the longer scale-length pre-plasma calculation (seen in Fig. 6.8a-c) and the shorter scale-length

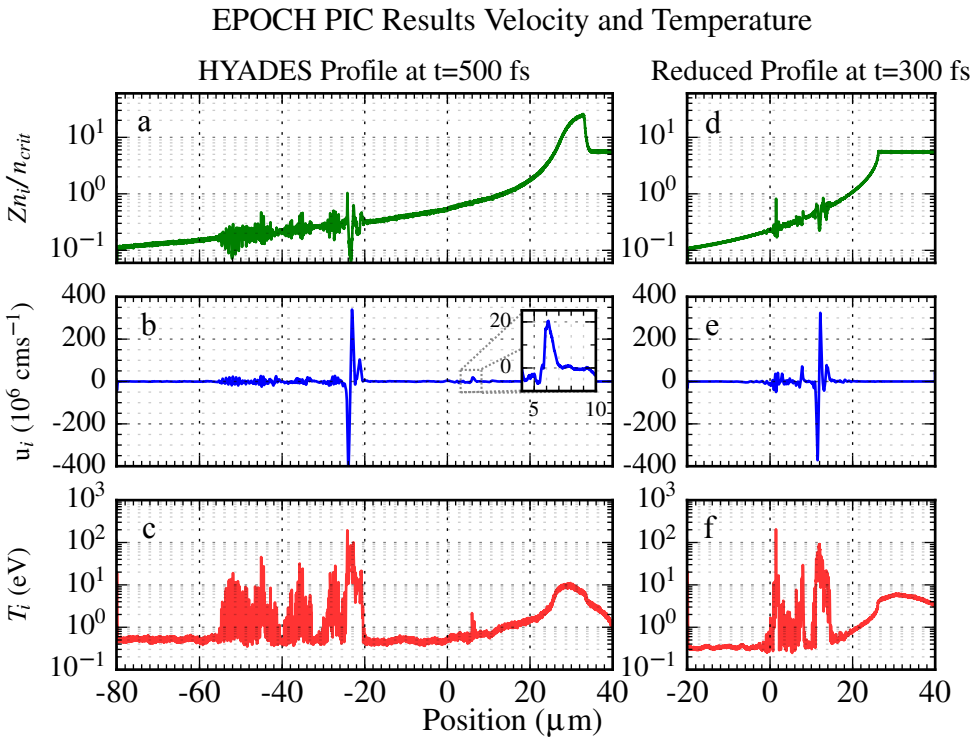

Figure 6.8: Plots showing results from EPOCH simulations using a HYADES density profile (left a-c) and a profile with a reduce density scale-length (right d-f). The top plots (a & d) show the ion density, the centre plots (b & e) show the cell-averaged fluid velocity of the ions, and the bottoms plots (c & f) show the cell averaged temperature. There are significant perturbations leading up to a region near $n_{crit}/4$, at which a large temperature spike is observable with concurring disturbances in the density and velocity plots. The inset plot highlights a comparatively small velocity perturbation of 20×10^6 cms^{-1} close to the critical density which is not observed in the shorter pre-plasma simulation.

pre-plasma (seen in Fig. 6.8d-f). The smaller perturbation, located at a denser region in the longer scale-length pre-plasma, does not appear to exist in the shorter pre-plasma results. Interestingly this smaller perturbation does not appear when these simulations are run without collisions, similar to the velocity perturbations seen in previous chapters.

A hydrodynamic calculation can now be initialised by combining outputs from the EPOCH simulation above, with T_i and $\mathbf{u}_f$ outputs from the original HYADES calculation 10 ps prior to the main pulse. To test whether the smaller velocity perturbation (visible in the inset in Fig. 6.8b) is related to the phenomena observed in the experimental results, only the region between -10 μm and 40 μm is simulated

initially. While there is a shock formed from this perturbation, it does not travel far enough into the denser region of the pre-plasma to be seen by the $n_{3\omega}$ probe. Also the shock front travels at a significantly smaller velocity ($\sim 4 \times 10^6$ cms^{-1}) than any of the experimentally measured phenomena.

The outward expansion of the pre-plasma at densities greater than n_{crit}, which initially starts at 4×10^6 cms^{-1} travelling *into* the target, and then gradually turns into an *outward* motion of 2.5×10^6 cms^{-1} at later times. The motion of the dense region of the target also does not appear to relate to phenomena observed in the experiment, and so further investigation into the lower density behaviour is required.

6.4.3.2 Instability Analysis

As the laser pulse travels through the under-dense plasma it suffers some significant degradation, possibly as the result of at least one plasma instability. To ascertain the nature of the instability, spectral analysis is required. Whilst both the longer and shorter scale-length simulations show significant disturbances, the longer scale-length pre-plasma is the simplest to analyse, as the instability occurs over a longer distance. The occurrence of many types of plasma instability are affected by collisions and so the analysis is performed with and without collisions switched on.

Using standard Fourier analysis techniques, pulse chirping, where the frequency or wavelength becomes a function of x or t, cannot be clearly resolved. By performing a Wigner-Ville transform on the laser pulse, rather than a Fourier transform, a determination of the wave-number $\mathbf{k}$ as a function of x is possible. The amplitude of a particular point, $a(x, \mathbf{k})$, in the Wigner-Ville transform can be understood as a quasi-probability that a wave, with a wave-number $\mathbf{k}$, is travelling through the point at position x. The 'quasi' nature of the quasi-probability comes from the fact that the amplitude a is also proportional to the amplitude of the original wave at this point. The sacrifice made in this type of analysis is that the output can suffer from some interference patterns.

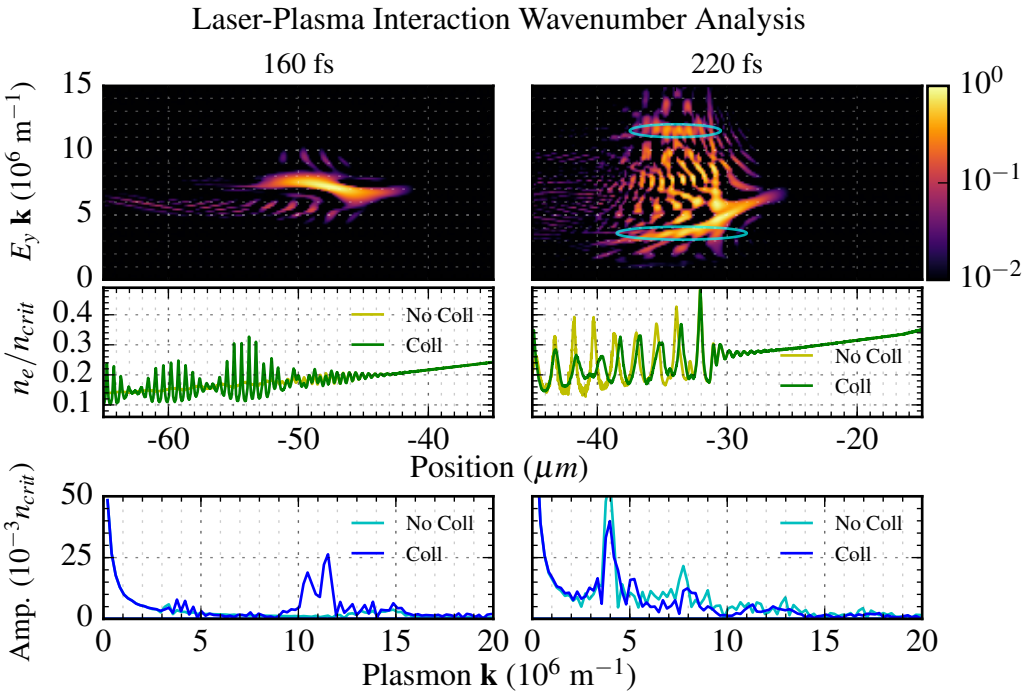

Figure 6.9: Plots from the EPOCH simulation using the HYADES density profile. The top plot shows the normalised Wigner-Ville distribution of the laser pulse at t = 160 fs and t = 220 fs for the simulation with collisions switched on. The middle plot shows the electron density and the bottom plot shows the Fourier transform of the electron density for simulations with collisions switched on and off. The ellipses visible in the top right plot show the location of scattered light waves calculated from the forward Raman scattering wave matching criteria.

Fig. 6.9 shows Wigner-Ville transforms of the laser pulse at two points in time. The first point in time (Fig. 6.9, left) shows the pulse at lower densities where the laser pulse is still mostly unperturbed. The second (Fig. 6.9, right) shows the pulse as it passes through plasma where $n_e \sim n_{crit}/4$. The electron density profile early on in time is significantly affected by collisions. The propagation and decay of stimulated Langmuir waves in the case where collisions are switched on appears to be significantly stunted and so Langmuir waves with $\mathbf{k}_{pe} \sim \mathbf{k}_l$ are still evident in the region behind the laser pulse. The Wigner-Ville transform of the laser pulse, 100 fs later in time, is significantly affected by instabilities in the plasma. The wave matching criteria for forward Raman scattering requires that the wave-number $\mathbf{k}_s = \mathbf{k}_l \pm \mathbf{k}_{pe}$, where the subscript s refers to a scattered wave, l refers to the incoming

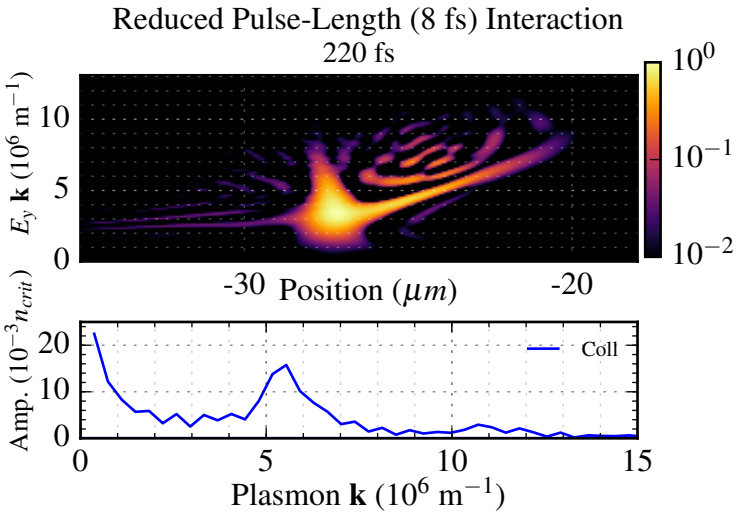

Figure 6.10: Plot showing Wigner-Ville transform of EPOCH simulation with shortened laser pulse-length of 8 fs. The top plot shows a significantly chirped pulse with the later part of the pulse significantly red-shifted close to where a soliton later forms at −20 μm. The bottom plot shows the a Fourier transform of the electron density at the same time.

laser pulse, and *pe* refers to a co-propagating Langmuir wave.

There is a significant peak in the Fourier transform of the electron density visible in both simulations at $\mathbf{k}_{pe} \simeq 4 \times 10^6$ m^{-1} (see the centre-right plot in Fig. 6.9). The laser pulse, when travelling through a vacuum, has a wavelength of 800 nm and so has a wave-number of $\mathbf{k} = 7.85 \times 10^6$ m^{-1}. So with the forward scattering wave-matching criteria there should be scattered light wave-numbers of $\sim 12 \times 10^6$ m^{-1} and $\sim 4 \times 10^6$ m^{-1}, which are drawn on Fig. 6.9.

Whilst it is possible that forward Raman scattering is the cause of the significant red-shifting of part of the main pulse, it may not be the sole cause. To eliminate the SRS instability a shorter pulse, shortened from 30 fs to 8 fs, can be used to see if the pulse still endures a significant amount of distortion despite insufficient time for SRS instabilities to grow. Fig. 6.10 shows the Wigner-Ville transform of the shortened 8 fs pulse at the same point in time (220 fs) and along the same density profile as the previous pulse. The pulse undergoes a significant chirp with a large amount of the pulse red-shifted to $\mathbf{k}_l = 4 \times 10^6$ m^{-1} (or $\lambda = 1600$ nm), the shift in wavelength of the affected pulse equates to a critical density $n_{shift} = n_{crit}/4$.

However, in this simulation the downshifted light simply reflects at the point where $n_e = n_{crit}/4$ rather than becoming trapped in the plasma. The anomalous red-shift of the laser pulse in this case may be as a result of scattering due to photon acceleration[173] (or deceleration in this case) which has been previously observed in laser wakefield settings.[174]

6.4.3.3 Soliton-Like Disturbance Formation And Evolution

The large disturbances visible in Fig. 6.8 at around the $n_e \sim n_e/4$ regions, in both simulations are re-plotted at later times in Fig. 6.11, along with the local electric and magnetic fields. The phenomena observable in the longer pre-plasma simulation shows a deep depression in both the electron and ion density surrounded by denser plasma. Within the depression there is a large-amplitude oscillating electromagnetic field with the same polarisation as the laser pulse. The phenomena in the shorter pre-plasma is similar, though the magnetic field does not appear to correlate, this could be related to the expansion of post-soliton walls. This particular type of

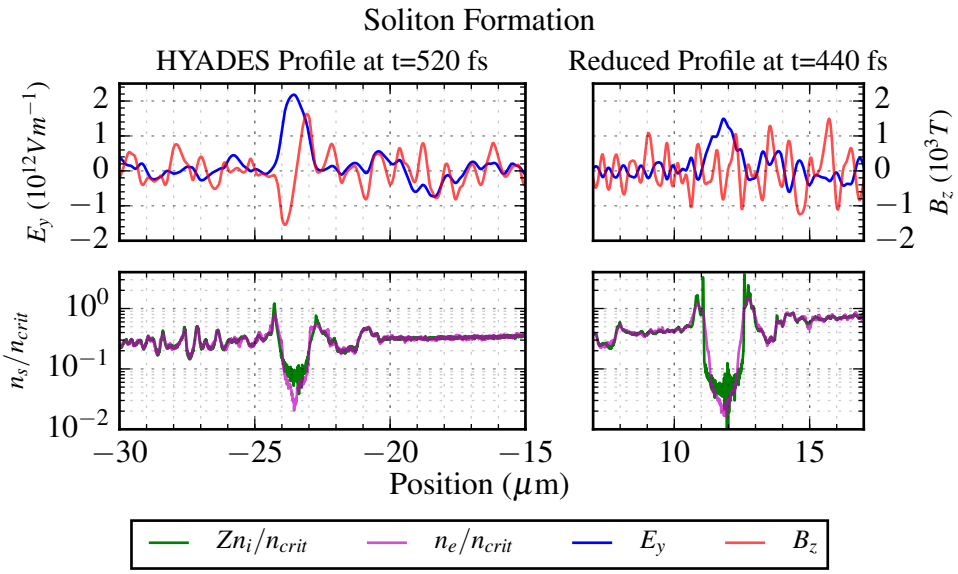

Figure 6.11: Plots from EPOCH simulations from both the longer (left) and shorter (right) pre-plasma runs. The top plots show electric and magnetic fields, whilst the bottom plots show ion (Zn_i/n_{crit}) and electron density (n_e/n_{crit}) around the $n_e \sim n_{crit}/4$ region.

feature appears to be very similar to magnetised post-solitons observed in similar conditions.[159,175–178] The low density material in the central depression is surrounded by a higher density region of ejected electrons (presumably ponderomotively pushed out of the higher field region) and ions. The surrounding material is travelling at extremely high cell-averaged ion velocities; with the wall on the low density side having a velocity of 400×10^6 cms^{-1} out away from the target, and the high density wall having a velocity of 200×10^6 cms^{-1} towards the target bulk.

Calculations of the longer term evolution of these structures has been attempted using the Lagrangian hydrodynamics code, in this case simply using the PIC code ion density n_i, ion temperature T_i, and a cell averaged ion velocity $\mathbf{u}_i$. The density at the shock fronts, n_{front}, varies significantly, starting at $n_{front} \leqslant n_{crit}$ and then rising as high as $n_{front} \sim 4n_{crit}$. The velocity of the walls is compared to experimental measurements in Fig. 6.12.

Whether a probe, with a critical density of $n_{3\omega} \simeq 9n_{crit}$, will interact with these structures depends on the evolution of the density in the shock fronts formed at the

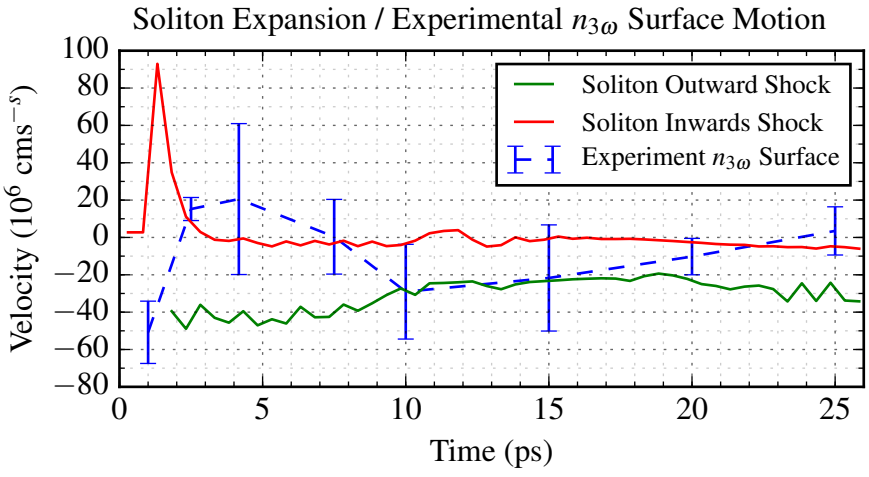

Figure 6.12: Hydrodynamic calculations of the expansion of the post-soliton like phenomena observable in the longer scale-length pre-plasma in Fig. 6.11. The green line shows the outwards motion of the shock facing away from the target bulk. The red line shows the motion of the shock on the denser side of the post-soliton, which is initially travelling towards the target bulk. These are compared to the experimentally observed $n_{3\omega}$ surface velocities.

walls of the post-solitons. The shock front density depends largely on the surrounding material, as there are several smaller features that produce smaller shocks which can then merge into the post-soliton wall shocks. The large compression of these wall shocks is due to the initial conditions set in the fluid code from EPOCH.

The initial formation of the walls, due to ponderomotive expulsion of electrons from a region of high electric field, is likely to be close to collisionless, due to the extremely high electron temperature in this region ($\sim 10^5$ eV).

The hydrodynamic calculation above assumes that the motion of the wall edges is a collisional hydrodynamic process rather than a collisionless one. This may not be a realistic assumption if the walls are driven by the electric field inside the soliton for a long (more than 0.5 ps) time after they are formed. In the simulations above the electric field continues oscillating inside the post-soliton cavity until the end of the PIC simulation, and so it is unclear whether the walls are driven apart by the ponderomotive force for a significant length of time or not.

6.4.3.4 Formation and Evolution of Post-Solitons

Whilst the formation and evolution of post-solitons has been discussed both analytically[177,179–185] and through the use of PIC codes,[175,178,186–189] it is only recently that they have been directly observed in laser-plasma experiments.[159,160,176,190,191]

Relativistic EM solitons are localised structures that can occur in collisionless plasmas. They consist of a low-frequency EM wave trapped in a low electron density cavity surrounded by a shell with a higher electron density. The relativistic electron motion is strongly coupled with the trapped electromagnetic mode, so that both particles and fields contribute equally to the total energy of the soliton.[178]

Post-solitons form as a result of the formation of relativistic EM solitons in a plasma. Relativistic EM solitons form as a result of dispersion effects[177,184,185] due to the finite inertia of the electron and the relativistic increase in the electrons effective mass. PIC simulations[175,192] show EM solitons are generated in the wake[193]

of an EM pulse and propagate at a velocity significantly lower than the speed of light, and with a frequency significantly lower than the local plasma frequency.

Ion motion can be neglected during the formation of a soliton as the oscillation period of the field inside the soliton is of the order[175] of $2\pi\omega_{pe}^{-1}$. Over a longer period of time the ponderomotive force due to the large amplitude EM field will push electrons out of regions of high field, lowering the local electron density at the centre of the pulse and raising the density around the edges of the pulse. The net effect of the density distortion is that the dielectric of the plasma in the central region is significantly decreased, whilst the dielectric around the edges is increased. The increase in the dielectric is not just as a result of the increased electron density, but by the increase in the electrons relativistic γ, in a similar manner to the relativistic self-focusing effect.[176]

At a much slower pace the ions are also pushed out of this region, not just by the ponderomotive push of the soliton EM field, but also by the charge separation effect of the electrons that have already exited the region. The charge separation can be significant enough to result in ion acceleration due to a coulomb explosion.[186] On the much longer timescale of ion dynamics, the soliton ceases to be a soliton, but a low frequency EM wave packet can still remain confined in the slowly expanding plasma cavity. Over time this low frequency EM structure can leak low frequency radiation[175,186,192] (though higher than the soliton oscillation frequency) and so gradually lose energy.

6.4.3.5 2D EPOCH Soliton Formation

A 2D density profile can be generated by taking a 1D profile in the y-direction and copying it along the x-axis to form a shelf-like, or cliff-like, edge. While this flat-faced type of density gradient is not likely to exactly match the experimental conditions, it can be used to test whether the laser pulse will create similar structures to those seen in the 1D case, if it enters the density gradient at an angle. An EPOCH

simulation using a 1200×2400 grid of cells for a box with dimensions 60×120 μm^2 is run with an electron species and an average ion species ($A = 7.2m_p$ and $Z = 3.85$). The laser is set with a $\lambda = 800$ nm and entering the simulation box at an angle of 40°.

While the cell dimensions, 0.05×0.05 μm^2, are small enough to resolve the laser wavelength adequately they will not resolve the Debye length for this density gradient. Due to the large number of cells in this simulation (2.88×10^6 cells) only a modest number of 100 particles per cell can be run with this simulation. The number of particles-per-cell can not increased without resorting to either much larger cells, which would compromise the resolution of the grid, or requiring significantly more computational power. Whilst a simulation with a reasonable signal-to-noise ratio is computable with collisions switched off, adding collisions increases the level of noise and self-heating due to grid aliasing, to the point where no useful results can be obtained.

Fig. 6.13 shows the ion density in the 2D collisionless EPOCH calculation approximately 200 fs after the reflection of the main pulse. The pulse reflects off a layer of plasma at $y = 20$ μm, which is the n_{crit} layer of this density gradient. In front of the critical density layer, at around $y = 15$ μm are three empty areas surrounded by denser plasma which are very similar to the post-solitons observed in the 1D calculation. However, the electric field quickly leaks out of the depressions and no trapped electromagnetic radiation is observable in the soliton depressions ~ 50 fs after they have formed. Without collision routines, the heating of the plasma at higher densities cannot be accurately calculated, and the ion temperature in the higher density regions remains below 1 eV as a result of this. To check whether the soliton expansion shown here would give a similar velocity to those observed experimentally, a 1D Lagrangian hydrodynamics simulation is set up using a slice of data from the 2D EPOCH calculation. This slice is taken from the region denoted in a green box in Fig. 6.13 and an average accross the y-direction is taken (as shown

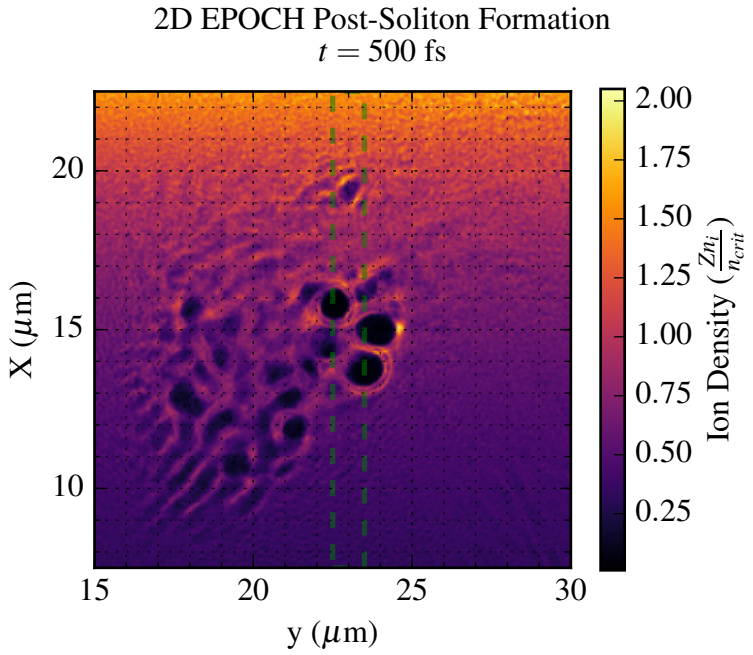

Figure 6.13: Plot showing the ion density profile from the 2D EPOCH calculation 200 fs after reflection of the main pulse off the $y = 20$ μm critical density layer. Deep depressions in ion density can be seen at around $y = 15$ μm. The region marked out with green dashed lines is used for a 1D hydrodynamic calculation.

in Fig. 6.14). The original input into the 2D EPOCH simulation did not include the pre-pulse shock front, and so there is no $n_{3\omega}$ density surface for a probe pulse to reflect from at $t = 0$. The results from this calculation can be seen in Fig. 6.15. At early times, 0-2 ps, there is no $n_{3\omega}$ critical surface and so the routine used to calculate the Doppler shift returns zero velocity. Between 2 and 10 ps the wall shock formed from the velocity peak at 16 μm (see Fig. 6.14) gains significant density and so is seen by the $n_{3\omega}$ probe. After this time the shock front formed by the soliton wall slows down and loses density to the point where $n_{front} < n_{3\omega}$. Later in time, between 17ps and 22ps, the slower shock merges with the smaller velocity peak (seen in 6.14 at 20 μm), and is again dense enough to be seen by the $n_{3\omega}$ probe.

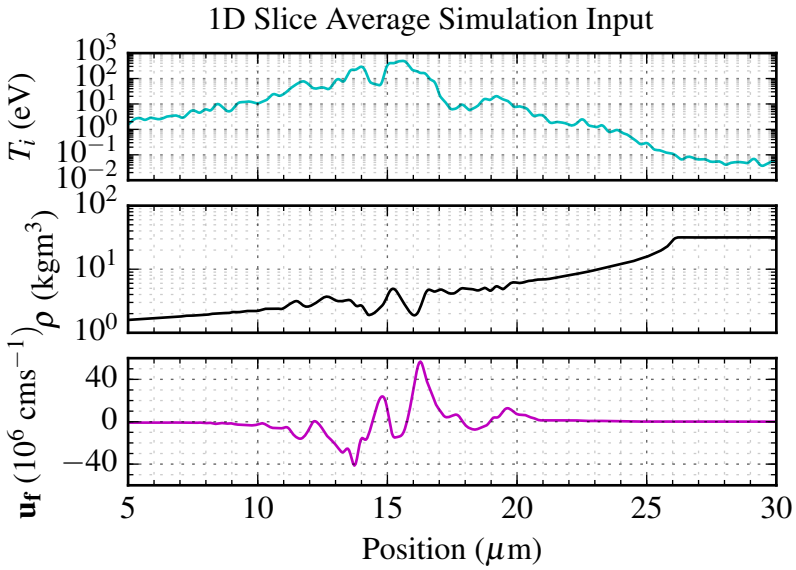

Figure 6.14: Plot showing input to a Lagrangian hydrodynamics calculation calculated from green area denoted in Fig. 6.13. The location of the post-soliton phenomena are approximately 14 μm and 16 μm.

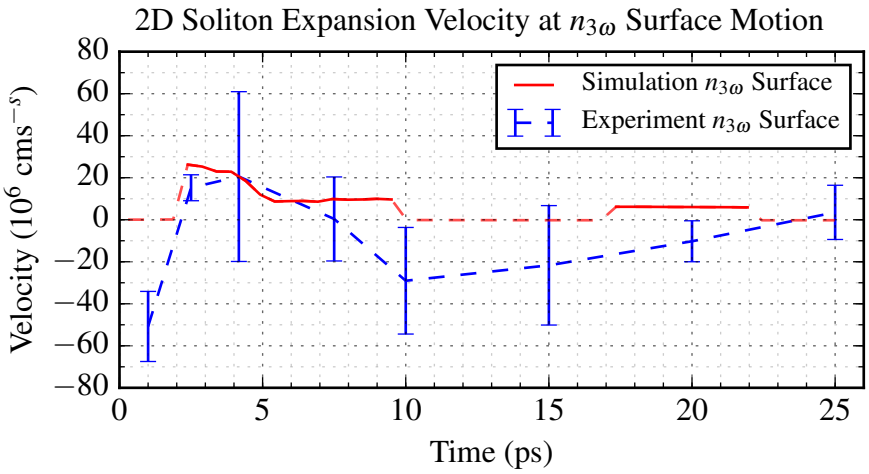

Figure 6.15: Plot showing velocity of $n_{3\omega}$ probe-density surface, blue line shows experimental data, while red line shows data taken from hydrodynamics code using input from 2D EPOCH calculation. The dashed red line indicates points in time where no $n_{3\omega}$ surface is available for reflection and so these velocities are recorded as zero.

6.5 Discussion

6.5.1 HYADES-Only Modelling

Results from modelling the entire laser-target interaction in HYADES (see Fig. 6.5), when using a small flux-limiter of 0.05, show similar inward motion to those

observed in the experiment. This inward motion is due to a shock forming at around the critical density. The outward motion, however, only matches when a larger flux-limiter, < 0.3, is used, where the outward motion comes from the breakup of the pre-pulse created shock-front (see Fig. 6.6). No explanation for the large outward motion detected at very early times ($t < 2$ ps) is apparent from the HYADES simulations, neither is any explanation for the smaller but extremely large Doppler shifted peaks seen in experiment (see Fig. 6.2). Attempts made to model the structure of the foam in HYADES did not result in significant changes to the pre-plasma structure or temperature, when compared to homogeneous target setups (see Fig. 6.3).

There are theoretical models that describe the hydrodynamic motion of foams[163] under intense laser illumination, but these are not generally implementable in standard fluid codes due to the fact they require a two-scale laser absorption model. Two such codes that have had some success at this include the 2D ALE hydro-code PALE[166] and the 1D hydro-code MULTI.[167] These methods may give different results to those obtained using the more simplistic fluid model of the foam applied here. In the case under investigation here there is a very large length-scale pre-plasma as calculated by HYADES, and so it is likely that 2D modelling would produce some significant departures from the findings presented here.

6.5.2 EPOCH 1D Modelling of Main Pulse Interaction

There are significant differences in the outcomes of the laser-plasma interaction with the main pulse that are seen in the EPOCH results as compared to those seen in HYADES. A large amount of energy appears to go into laser-plasma instabilities when the PIC code is employed. Both of the observed instabilities, the possible stimulated Raman scattering instability, and the photon acceleration type red-shifting of the laser pulse, generate post-soliton-like phenomena. These post-solitons generate large shocks at their edges in the low density regions of the pre-plasma. These wall

shocks progress at velocities comparable to those measured in experiment (see Fig. 6.12). However, hydrodynamic calculations of the progress of these shocks show that they do not progress deep enough into the target, in the time given, to reach the densities observable by the probe. An alternative method of modelling the pre-pulse interaction may give a different shaped pre-plasma which may enable these shocks to progress further into the target and thus still offer a possible explanation of the cause of the Doppler shifts seen in the experiment.

6.5.3 EPOCH 2D Modelling of Main Pulse Interaction

A 2D EPOCH PIC simulation, using the 1D shortened pre-plasma (seen in Fig. 6.7) was used to generate a shelf-like profile in 2D by copying the density profile along the y-axis. The laser-plasma interaction in this case generated more post-soliton like structures around the $n_{crit}/4$ region. The hydrodynamic motion of the wall-shocks surrounding the post-solitons are similar, in both timing and velocity, to the inwards velocities measured in the experiment, as well as reaching appropriate densities that will reflect a 3ω probe pulse. However, the outward expansion that is visible in the experimental data in Fig. 6.15 is not reproduced in the PIC calculation, most likely due to the heating at denser locations being dominated by collisional effects which were not simulated.

6.5.4 Conclusions

The extra reflected peaks recorded in the experimental results, (see Fig. 6.2) do not seem to match any phenomena occuring in either the HYADES or the EPOCH calculations and so no explanation can be made about the possible origins of these points. However, a possible explanation of the central larger Doppler shifted peaks can be made using the modelling shown in this chapter.

Post-soliton wall shock motion might explain the inward motion into the target

measured in the experiment (the positive velocities observed in Fig. 6.2). Electron heating of the pre-pulse formed shock (see Fig. 6.3 for the HYADES result), which explains the initial outward motion in the high contrast silicate target experiment (see Chapter 4), does not appear to explain the outward motion in this case. Looking at Fig. 6.12 it is possible that the initial outward expansion could come from an outward travelling wall-shock from a post-soliton like phenomena, if the soliton can be formed in a region with a high enough initial density. However at later times, these outwards travelling wall shocks would travel into less dense regions and so would be unlikely to account for later experimental results.

Chapter 7

Fast Electron Transport and Resistivity Dependent Filamentation

7.1 Introduction

In order to understand the effect of low temperature resistivity on early time electron beam filamentation the disordered forms of two materials with significantly different Z: aluminium and copper, are studied. The disordered state can occur either due to the materials being an amorphous alloy, or due to melting from the solid state. The hybrid code Zephyros is used to study the transport of electrons through these materials driven by a range of laser intensities. The resistivity of the background electron fluid is modelled using the Lee-More resistivity model,[194] and the Thomas-Fermi model is used to determine the ionisation state.

Two important results are obtained from this study: Firstly that materials with a lower peak resistivity tend to exhibit larger collimating magnetic fields, which act to suppress filament formation, and, secondly, that this magnetic field growth is due to a lower rate of heating in those materials. The role of the cold electron

resistivity in suppression of the filamentation instability is examined analytically and shows little change across the two materials, again indicating that the magnetic field growth is the main mechanism for suppression of filaments in this case.

There are several seed instabilities that can lead to the onset of the filamentation instability the two thought to be the most significant[195] are the Weibel[196] and transverse density modulational instabilities.[80]

The Weibel instability requires beam of electrons to have an anisotropic velocity distribution and results in the spontaneous growth of transverse density waves in that electron beam. A qualitative explanation,[197] but not fully rigorous, can be thought of starting from a small perturbed magnetic field of the form $B = Be^{ik_x}$. The trajectory of an electron travelling with velocity $\mathbf{v} = v_y$ through this field would be bent by the Lorentz force ($\mathbf{F} = -q_e\mathbf{v} \times \mathbf{B}$) in the $-z$-direction (the opposite for those with $\mathbf{v} = -v_y$). This results in a current sheet in the z-direction, Ampere's law implies that this current sheet generates a magnetic field with a component which acts to reinforce the initial magnetic perturbation, and so the instability grows. For a more rigorous approach see Refs 198 and 196. This instability can lead to a fragmentation of an electron beam into smaller divergent filaments.

The modulational instability occurs as a result of a density perturbation and can be thought of in a similar way.[80] However, a density perturbation in this case alters the resulting magnetic field generated from the electron current such that it generates a self reinforcing magnetic field perturbation. A more detailed approach to calculate a growth rate for the filamentation instability is taken in section 7.5.

7.2 Simulation Methodology

Zephyros is a hybrid fast-electron code which uses a particle-in-cell model for the fast electron modelling with a static fluid to represent the background electrons. The simulated targets have dimensions $200 \times 200 \times 50$ μm^3, consisting of cubic cells

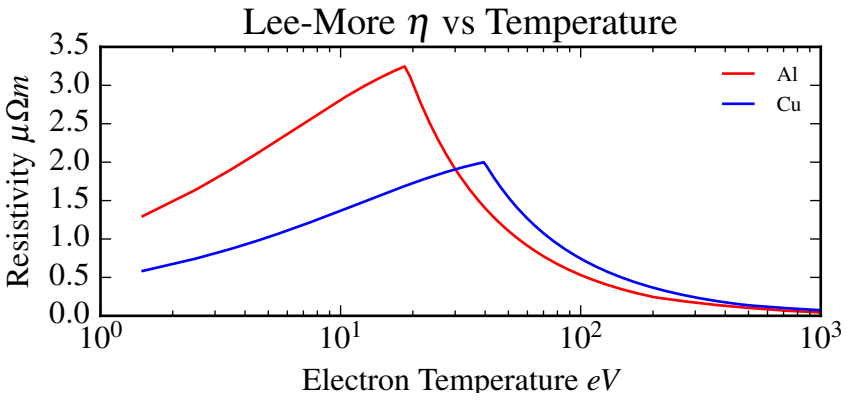

Figure 7.1: Reduced Lee-More resistivity curves for Aluminium and Copper with an effective cold-electron m.f.p. equal to the inter-atomic spacing at the solid density of the two metals.

0.5 μm to a side, with the laser normal to the largest surface.

An assumption of a disordered ion spatial distribution is used, which implies an isotropic cold-electron mean-free path (m.f.p.). To simulate the effect of the laser-plasma interaction, fast electrons are injected into the target across a focal spot with a FWHM of 9.4 μm, with a uniform injection angular distribution up to a maximum of 70° half angle. There are a total of 5×10^7 macro-particles used in each simulation which are gradually injected over the total length of the pulse, t_l = 800 fs, at each time-step according to a top-hat distribution.

The pulse length is chosen simply so that there is sufficient time for the fast electrons to propagate to the far side of the target during the laser pulse. The electrons have an energy spectrum determined using the ponderomotive scaling where $T_f = m_e c^2\left(\left(0.73 I_{18}\lambda_{\mu m}^2 + 1\right)^{1/2} - 1\right)$ and $I_{18} = 1\times10^{18}$ Wcm^{-2}. To calculate the scaling an effective laser wavelength λ = 1.053 μm is chosen to be consistent with an Nd:glass laser system. The intensity is varied from 0.1 to 5 $\times10^{20}$ Wcm^{-2} which, given the scaling described, produces an electron distribution with T_f varying between 1 and 10 MeV. The initial temperature of the targets is set to 1eV, which assumes a high-contrast laser-pulse. An implementation of the Lee-More[194] resistivity model is used as certain experiments[199] have compared well to theoretical predictions using this model, which along with it being relatively easy to implement, has led to its

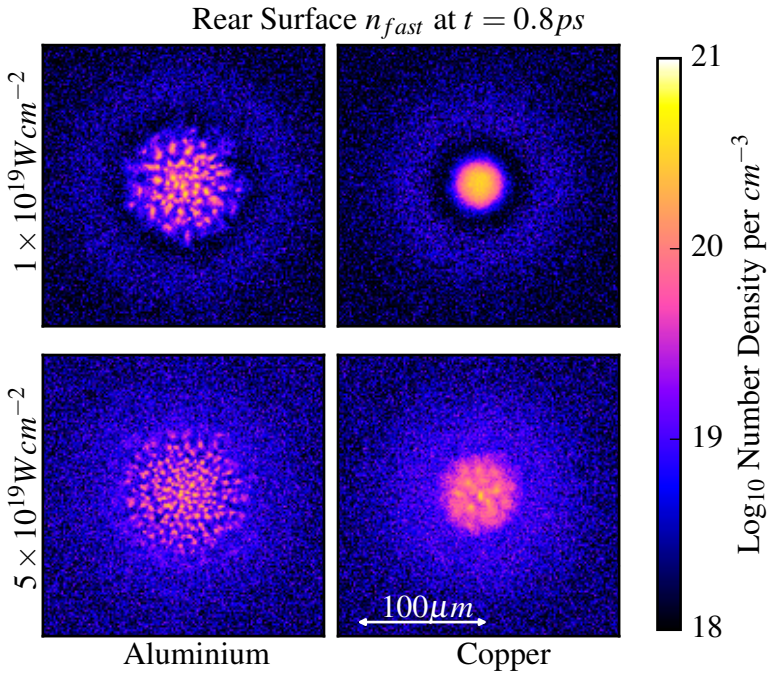

Figure 7.2: Rear surface fast electron density plots of aluminium (left) and copper (right). At the lowest intensity (top row 10^{19} Wcm^{-2}) copper shows no filamentation at all whilst aluminium shows a significant amount. At a slightly increased intensity of 5×10^{19} Wcm^{-2} (bottom row) there are a small number of more diffuse filaments in the copper, whilst the aluminium retains a large number of tight filaments. The halo-like features observable in the top two plots are refluxing electron populations.

widespread use.

The two materials, disordered allotropes of aluminium and copper, are chosen because their atomic number and solid density are different enough that the Lee-More model would give significantly different resistivity profiles. In this implementation, rather than use the prescription given in the original Lee-More model for the minimum m.f.p., the minimum cold-electron m.f.p. is specified as an input parameter to the model. The initial cold-electron m.f.p. is set, isotropically, to the inter-atomic spacing (r_s) (1.62 Å for Al and 1.45 Å for Cu) to simulate disordered ion spatial distributions. The two resistivity profiles can been seen in fig.7.1. The resistivity profile calculated for copper peaks at a higher temperature, but lower resistivity, when compared to the aluminium profile (2 $\mu\Omega$m at 40 eV for Cu vs. 3.2 $\mu\Omega$m at 19 eV for Al).

7.3 Comparison of Copper and Aluminium Transport

The fast electron transport pattern in each simulation can be examined by looking at transverse and longitudinal slices of the fast electron density at later times. Fig. 7.2 shows rear surface plots of the fast electron density at the end of the laser pulse (t=800fs), from these it is immediately obvious that there is a significant difference in the propagation of the electron beams through the two materials. The copper target at the lowest intensity shows a highly collimated beam terminating in a tight dense spot whilst the aluminium target shows multiple smaller spots indicating a highly filamented beam. When the laser intensity is raised to 5×10^{19} Wcm^{-2}, the copper then shows a slight breaking up of the beam.

In order to summarise results from all of these simulation runs; several slices, with a width of 10 cells, were taken out of the centre of the n_{fast} profiles in fig.7.2 and a Fourier spectrum of each was taken (see fig.7.3). To avoid being limited by noise these spectra were then averaged across the width of the slices to create a 1D profile before being transformed. The spectra in fig.7.3 show the relative prominence of features at particular scale lengths. A spectra showing a lot of features around the 5-15 micron level would denote a fragmented rear spectrum indicating filamentation of the electron beam. Conversely, a spectra showing a dominance of features around the 50-100 micron level would indicate a collimated beam. Only the lowest intensity copper target simulation shows collimation of the electron beam with negligible filamentation.

7.4 Magnetic Field and Resistivity

There is a remarkable difference in the global B-field in copper versus aluminium, namely that it has a larger magnitude and is has a more cylindrical shape in copper.

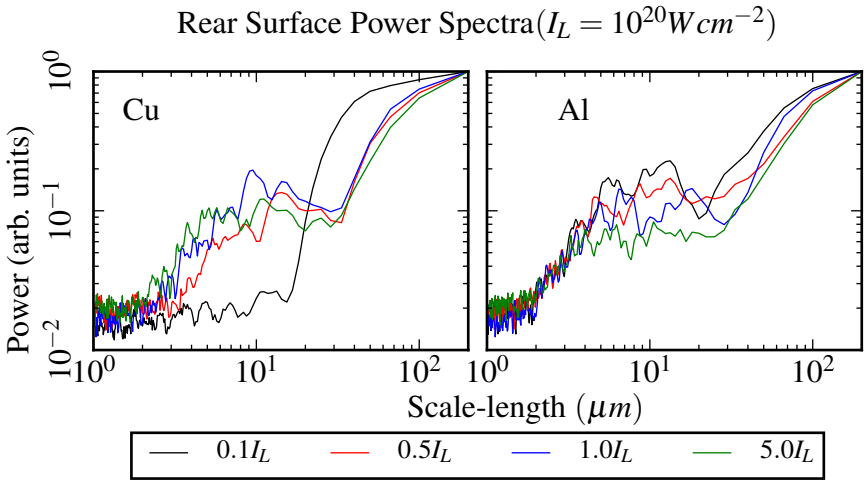

Figure 7.3: Power spectra of rear surface fast electron density features for aluminium (left) and copper (right). These spectra show how often features occur at particular scale lengths, in simulations where fast electron filamentation has occurred there is a significant rise in the quantity of features around the 5-10 micron size. It clear from these plots that the filamentation instability is turned off for copper at low intensities.

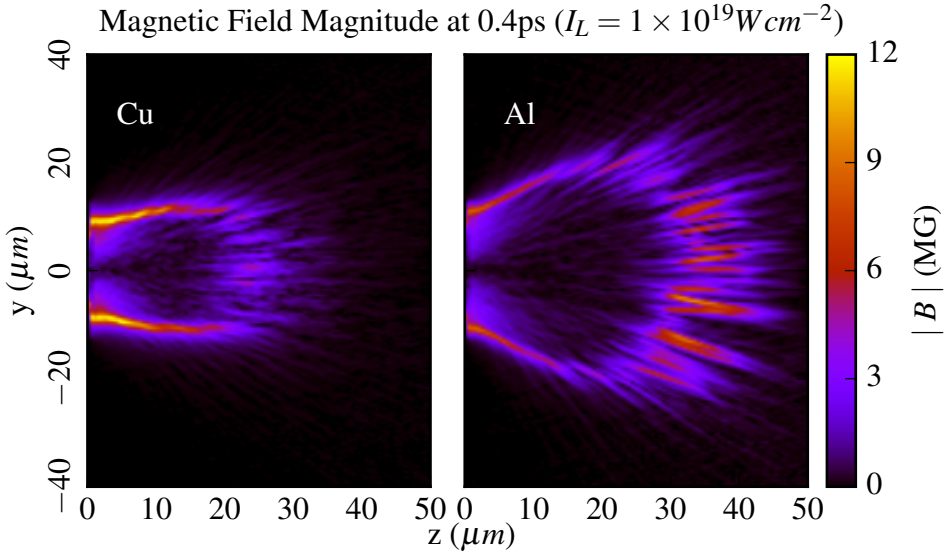

Figure 7.4: Plots of the magnetic fields after 0.4ps of growth, halfway into the 0.8ps laser pulse. The aluminium target shows magnetic field growth almost all the way across the target to the rear side where as the copper target has a much more compact magnetic field structure locate towards the source of the fast electrons.

This is curious given the lower peak resistivity of Cu. The magnetic field along the axis of propagation is shown for both targets in fig.7.4. Earlier growth of the magnetic field in the aluminium case appears to promote the growth of filamentary structures. At around 10 microns away from the injection region linear modulations

appear in the magnetic field in the aluminium target, whilst the copper target shows strong magnetic fields acting to confine the beam at this point.

The higher low-temperature resistivity in the aluminium target allows fine structures to grow more quickly in the magnetic field. These fine scale structures act to promote the divergent filamentation of the electron beam, with narrow B-field channels forming acting to individually collimate beam filaments leading to a refinement of the fine-scale structure. Conversely in the copper target, where the low temperature resistivity is smaller, larger-scale magnetic fields tend to grow which can then act to collimate the beam and suppress smaller-scale magnetic field growth. Whilst the fine-scale structures are still evident in the copper target, the large-scale collimating fields confine the electrons to a narrow channel, suppressing the smaller scale filament growth.

A simple rigid beam model[140] can be used to explore this phenomena further. In order to explain the larger magnetic fields seen in the copper target a rigid-beam calculation,[140] considering only Ohmic heating (eqn.7.1) and resistive magnetic-field growth (eqn.7.2) is used to calculate the expected magnetic fields. The fast-electron current J_f is considered as a rigid beam of electrons with a Gaussian profile decreasing with r. To keep the analysis consistent, the Lee-More model was used for the resistivity, and a simple fit from the Thomas-Fermi model for n_e was employed.

$$\frac{dT}{dt} = \frac{J_f^2 \eta(T)}{\frac{3}{2} n_e(T) e} \tag{7.1}$$

$$\frac{dB}{dt} = -\nabla(\eta(T) J_f(r)) \tag{7.2}$$

Fig. 7.5 shows much larger magnetic field growth closer to the centre of the beam in the copper target as compared to the aluminium target. The main reason for the larger fields in the copper target is the consistently lower resistivity at low temperatures. This allows for a lower rate of heating whilst still providing enough resistivity

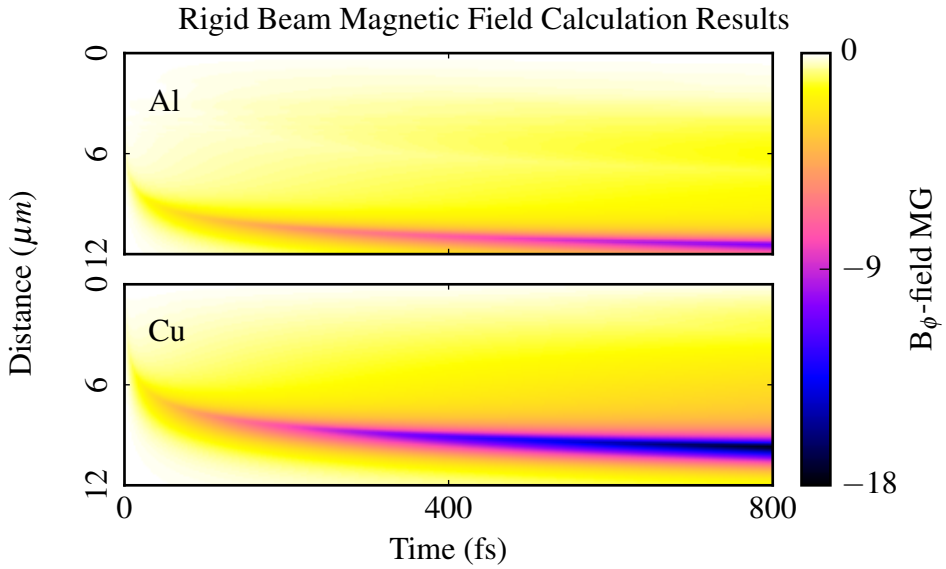

Figure 7.5: Magnetic field calculations made using a rigid-beam model, the copper target shows a significantly larger magnetic field compared to the aluminium target. The distance from the centre of the beam to the peak magnetic field is much smaller in the copper target than the aluminium.

to generate significant magnetic fields for a longer length of time before slipping into the Spitzer regime where the growth of the magnetic fields is significantly reduced.

The time taken to reach the peak resistivity is also of interest. The peak resistivity is the point at which the Lee-More model switches from a solid-state type model to using the Spitzer treatment, which significantly lowers the resistivity in the material (as shown in Fig. 7.6). The B-field calculated by the rigid beam model and t_{peak} peak at the same point in both the copper and aluminium calculations as can also be seen in fig. 7.6. An approximate time taken to reach peak resistivity, and so the peak growth of the magnetic fields, can be found using a simpler treatment than that given by the Lee-More model. Given a simplistic approximation where $\tau = \frac{\mathrm{d}_{ion}}{v_th}$ and d_{ion} is the inter-atomic spacing of the material, and substituting for v_{th}, we can now write:

$$\eta = \frac{m_e}{e^2 n_e \tau} = \frac{m_e}{e^2 n_e \mathrm{d}_{ion}} \sqrt{\frac{k_B T_e}{m_e}} \tag{7.3}$$

The electron density predicted by the TF model varies considerably with temperature in the region between 1 and 40 eV. However, given $n_e = n_i Z(\frac{Z_{eff}}{Z})$, the change

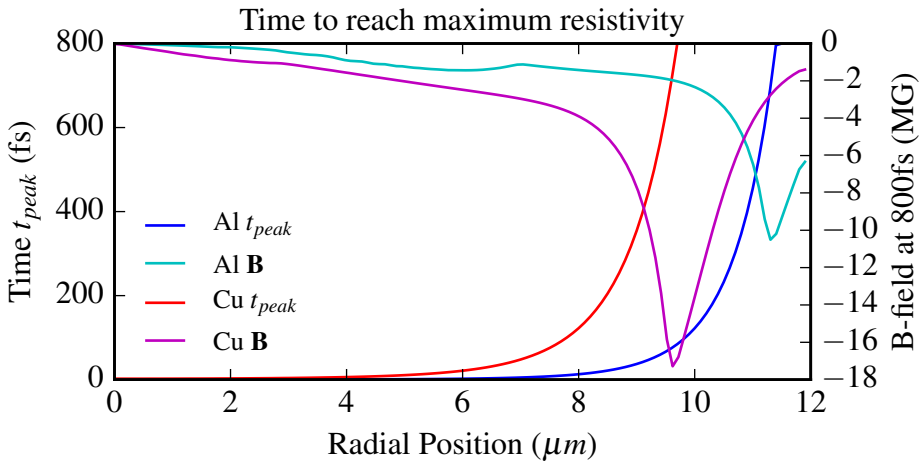

Figure 7.6: Time taken to reach the peak resistivity as a function of distance from the the center of the beam in the two materials, this was calculated using the rigid beam model. The increase in t_{peak} with distance matches up well with final B-file profile calculated using the rigid beam model.

in the relative ionisation as a function of the background electron-temperature $(\partial(Z_{eff}/Z)/\partial T_{back})$ of both materials is very similar. If the ratio of the peak times is calculated then the variation in the relative ionisation in the two materials cancels out. Equation 7.1 can then be integrated between 1 and 40eV to give the time taken to reach the peak temperature. The ratios of these two times can be equated as follows:

$$\frac{t_{Al}}{t_{Cu}} = \frac{n_{iAl}^2 Z_{Al}^2}{n_{iCu}^2 Z_{Cu}^2} \sim 0.1 \tag{7.4}$$

This result also matches up with the numerical treatment used in the rigid beam model where, at the center of the beam, at peak J_{fast}, copper t_{peak} = 2.24 fs and aluminium t_{peak} = 0.236 fs. Taking the peak resistivity from the Lee-More model used previously, the magnetic field can be given the same treatment as the time to reach peak η to give:

$$\frac{B_{Al}}{B_{Cu}} = \frac{\eta_{Alpeak} t_{Al}}{\eta_{Cupeak} t_{Cu}} \sim 0.16 \tag{7.5}$$

This treatment, though simplistic, does show a magnetic field strength that has a strong dependence on the time spent at low temperatures, i.e. the time spent outside of the Spitzer regime.

7.5 Resistivity Dependant Effects

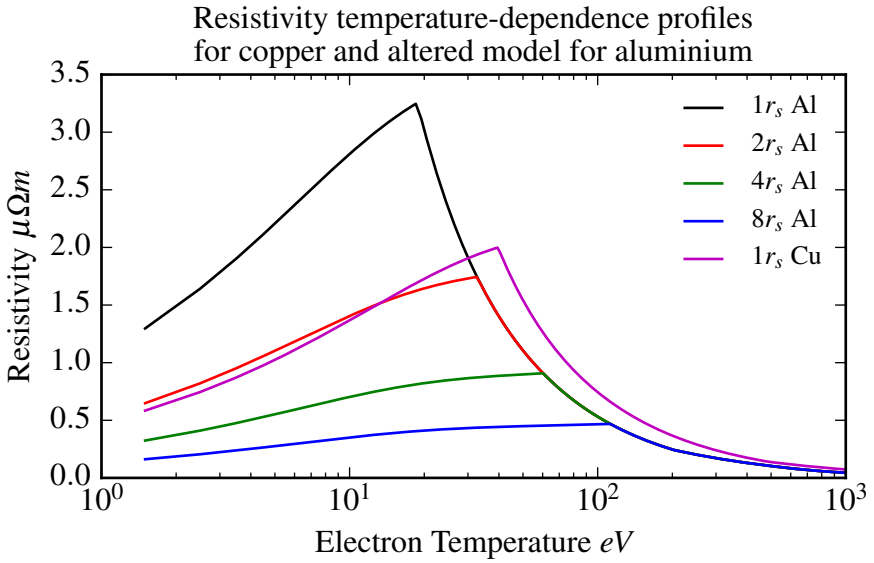

Figure 7.7: Plot comparing the resistivity of aluminium with different assumed cold-electron m.f.p. lengths alongside copper at the shortest assumed m.f.p. length.This comparison shows a similarity in the cold resistivity between the longest aluminium m.f.p. and the shortest copper m.f.p..

The Lee-More[194] model can be used with an arbitrary choice of the minimum m.f.p. for the electrons. So far in this study the m.f.p. has been set to the interatomic spacing, and this is also the absolute minimum for the m.f.p. in the original Lee-More model. However it should be noted that in the original Lee-More model, when the electron m.f.p. did not fall below the interatomic spacing, the minimum m.f.p. was determined using the Bloch-Grüneisen formula complemented by an expression to account for melting. Since an assumption that our target is already highly disordered/molten is made, our approach actually ends up being equivalent to the orignal Lee-More approach for the case where the target temperature is well above the melting temperature.

The value of the absolute limit on the minimum electron m.f.p. is, however, open to question, and varying this value can have a substantial effect on the resistivity curve. To study the effect of changing this parameter on the magnetic field

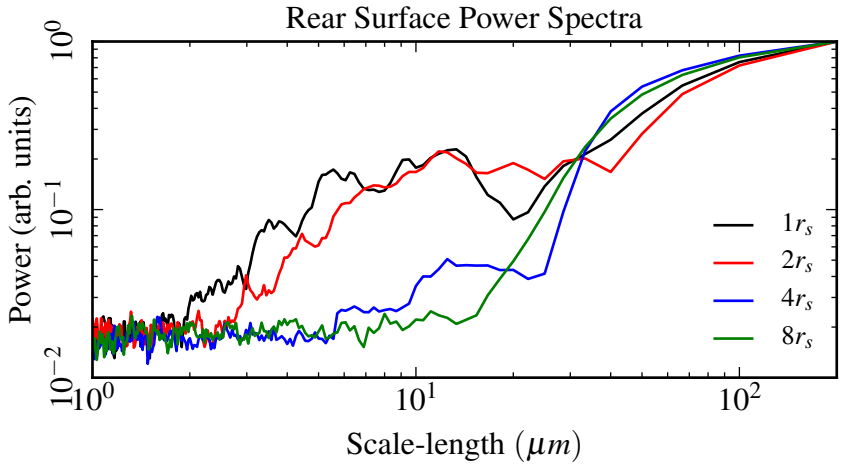

Figure 7.8: This plot show the effect of increasing the m.f.p. of the cold-electron background, which effectively lowers the resistivity calculated by the Lee-More algorithm. Increasing the m.f.p. beyond twice the inter-atomic spacing results in a smooth profile with no filamentation.

growth, in absence of any other factor, an altered version of the Lee-More model was calculated where the low temperature cold-electron m.f.p. was multiplied by a factor which was chosen to be 2, 4 or 8. The newly altered resistivity profiles are shown in Fig. 7.7.

By altering the resistivity profile of the aluminium at low intensities it is possible to suppress the filamentation of the electron beam enough to get significant collimation and confine the beam to ~ 20 μm. Fig. 7.8 show the newly generated spatial feature spectra for aluminium targets with the altered resistivity profiles. In the targets where the resistivity approaches more than 0.5 $\mu\Omega$m at a temperature of 1eV or below filamentation occurs and shows a multitude of tightly confined filaments. Above this limit and the electron beams are collimated. There is, however, a borderline case $l_{mfp} = 4r_s$, which shows less well defined individual filaments that are held together in a large scale collimating magnetic field. These collimating fields are a result of low resistivity at low temperatures, meaning less ohmic heating at earlier times and larger magnetic fields as a result.

Whether the filaments are suppressed by the large collimating fields, or they do

not grow as a result of lower resistivity, is now investigated. Starting with Faraday's law, Ohm's law, and a linearised set of fluid equations, the growth rate for the resistive filamentation instability can be found[80] (which is also similar to an earlier treatment described in ref. 198) so that this time-scale can be compared to the growth of the larger-scale magnetic fields. Given Faraday's law:

$$\frac{\partial \mathbf{B}}{\partial t} = -\nabla \times \mathbf{E} \tag{7.6}$$

and Ohm's law:

$$\mathbf{E} = -\eta \mathbf{j}_f \tag{7.7}$$

and considering a two-dimensional geometry with an isotropic resistivity and $j_x = J_{fast}$, we can write:

$$\frac{\partial B_z}{\partial t} = \eta \frac{\partial j_x}{\partial y} \tag{7.8}$$

The system is then perturbed so that $n_f = n_{f0} + n_1$, $u_{fy} = u_{y1}$, $u_{fx} = u_{x0}$ and $\gamma = \gamma_0$. Using these perturbations and only considering first order terms gives a linearised continuity equation:

$$\frac{\partial n_1}{\partial t} + n_{f_0} \frac{\partial u_{y_1}}{\partial y} = 0 \tag{7.9}$$

The magnetic portion of the Lorentz force (linearised again) can be written for the fast electrons as:

$$\frac{\partial u_{y_1}}{\partial t} = \frac{e u_{x_0} B_z}{\gamma_0 m_e} \tag{7.10}$$

Taking the density (and therefore current) perturbations to be sinusoidal, the velocity (and therefore magnetic field) must be 90° out of phase, giving $n_1 = n_{f_0} \mathrm{N(t)} \cos(ky)$, $J_{fast} = J_{fast} \mathrm{N(t)} \cos(ky)$, $u_{y_1} = u \sin(ky)$, and $B_z = B \sin(ky)$. Substituting into the continuity (eqn. 7.9), Lorentz (eqn. 7.10), and the modified Faraday/Ohm's law

(equation 7.8) and cancelling out the sinusoidal functions gives:

$$\frac{\partial B}{\partial t} = -\eta J_{fast} \mathrm{N} k \tag{7.11}$$

$$\frac{\partial \mathrm{N}}{\partial t} = -ku \tag{7.12}$$

and

$$\frac{\partial u}{\partial t} = \frac{eu_{x_0}}{\gamma m_e} B \tag{7.13}$$

Repeatedly differentiating and substituting for N in equations 7.11,7.12 and 7.13 gives:

$$\frac{\partial^3 \mathrm{N}}{\partial t^3} = \frac{\eta k^2 e u_{x_0} J_{fast}}{\gamma_0 m_e} \mathrm{N} \tag{7.14}$$

This differential equation has a solution of the form:

$$N \propto e^{gt} \tag{7.15}$$

where

$$g = \left[\frac{\eta k^2 e u_{x_0} J_{fast}}{\gamma_0 m_e} \right]^{1/3} \tag{7.16}$$

Given that the growth factor, $g \propto \eta^{1/3}$, a change (at 1eV) from η_{Al} = 1.07 $\mu\Omega$m to η_{Cu} = 0.48 $\mu\Omega$m yields a growth rate in copper of 76% of that in aluminium. At the lowest laser intensity investigated here the filaments in the copper target are completely suppressed and a strongly collimated beam is observed. This behaviour is likely not due to the reduction in the filamentation growth rate, which is in itself due to the change in resistivity across the two materials, but lies with the larger magnitude and scale magnetic fields observed in the copper target.

7.6 Conclusions

The filamentation of the electron beam in a high-intensity laser-plasma interaction is critically dependant on the magnitude and typical feature size in the resistive magnetic fields generated by drawing of a cold-electron return current. In this simulation-based study several hybrid fast-electron simulations were used to investigate disordered forms of aluminium and copper.

The following observations were drawn from the results of these simulations: The simulations where the low-temperature resistivity is high were seen to have significantly higher levels of filamentation, indicating a critical relationship between the starting resistivity and the onset of filamentary structures in the electron beam. The resulting magnitude and scale-length of the later magnetic fields, in the material with the higher resistivity, was significantly smaller than that of the lower-resistivity material.

The heating effect attributed to high-resistivity materials has a very important effect on the growth of the magnetic fields within them, with higher resistivity effectively stunting the growth of large collimating magnetic fields, allowing small transverse scale filamentation to occur. Conversely a lower rate of heating allows for significantly larger fields to grow, resulting in far more effectively collimated electron beams and suppression of filamentation.

The growth rate of the resistive filamentation instability is not significantly different between the case where there is filamentation to that in which there is not. This implies that the fact that copper has a lower resistivity is not the sole, or main, cause of the absence of filaments where the beam is collimated. This collimation is, however, due to the fact that high resistivity materials are heated more quickly and so the enter the Spitzer resistivity regime much sooner, where the resistivity drops to a much lower level than when cold. These conclusions are supported by a simple analysis of the case of a rigid beam of fast electrons traversing a resistive medium

and a simple analytic model of the filamentation growth-rate.

Chapter 8

Conclusions

8.1 Doppler Spectroscopy

8.1.1 Silicate Target

Chapter 4 & 5 show Doppler spectroscopy experiment, and modelled, results for identical silicate targets with differing laser contrasts. The laser contrast appears to have a dramatic impact on the measured Doppler-shift. The lower contrast laser system used in chapter 5 has a pre-pulse intensity approximately a factor of ~ 100 larger than the pre-pulse occuring in the high contrast laser system used in chapter 4 (see Fig. 5.1 and Fig. 4.1 for the relevant contrast measurements). A low contrast laser system produces Doppler-shift results of significantly smaller sizes (by a factor of ~ 10) than those seen in the high contrast results (see Fig. 4.2 and Fig. 5.2).

The initial first step in modelling the experiment was to use HYADES, a radiation-hydrodynamics simulation, to model the entire experimental scenario; from pre-plasma generation through to the main-pulse interaction and then on to the motion of the excited plasma afterwards. The second step in modelling the experiment was to use a three stage approach: firstly using the HYADES simulation results to initialise EPOCH to calculate the effect of the main pulse interaction,

finally initializing a Lagrangian hydrodynamic code using the density, ion temperature, and ion velocity from EPOCH.

The result from using HYADES-only calculation in the high contrast scenario presented in chapter 4 (seen in Fig. 4.5) do resemble the experimental results in both magnitude and timing[1]. This simulation shows a shock produced around the critical density which then travels through the over-critical region of the plasma where the probe then detects the compressive motion of the shock. However, while the three stage modelling additionally performed shows only a slightly better match to experimental results, it shows a dramatically different hydrodynamic process occurring. In contrast to the HYADES simulation that shows a shock passing into the over dense region, the three stage modelling shows a shock forming and then being pushed back by expansion from the bulk plasma. The additional heating found in the PIC code is due to the collisional interaction of a warm electron population with the ions. It is possible that the heating in the PIC code was exaggerated. However, a great deal of care was taken to obtain convergent results, and so mode-aliasing, which is a particular problem at high densities, is unlikely to cause excessive heating. If there is excessive heating it is likely due to the warm electron population having a fan-like trajectory pattern which would not be captured in 1D, though given the very narrow length-scale (a few micron) this may not be a significant effect.

The results from the HYADES-only calculation in chapter 5 are very different to those obtained experimentally. The results are also highly dependent on the flux-limiter values chosen, with a larger inwards motion detected much later with large flux-limiters when compared to experimental values. While the laser-plasma interaction may not be sufficient to capture the behaviour of the target under a short-pulse ultra-intense laser interaction, the fact that the code cannot capture 2-

[1]With the notable exception of the initial outwards expansion at $t = 2$ ps, which is reproduced by the three-stage modelling.

3D expansion may also be a significant factor in the mismatch with the experimental results. The results from the three stage modelling were only comparable to the experimental results when using a reduced scale-length pre-plasma. This indicates that there is likely to be lateral expansion of the pre-plasma which is not captured by a 1D code.

The three-stage modelling for chapter 5 showed a similar, though with smaller velocities, hydrodynamic process to that shown in the same modelling for chapter 4. The shock produced by the main pulse does not appear to progress far into the plasma before it is pushed back by expansion from the bulk of the target. This expansion is again caused due to additional heating found in the PIC code due to the collisional interaction of warm electrons with the ion population. In this case however, but the inwards velocity of the shock, and the outwards expansion of the target bulk are around a factor of 10 smaller. The smaller magnitude of the inwards propagating shock is likely due to a combination of a slightly enlarged region around the critical density, and a large amount of energy being absorbed in the low density region of the plasma. The smaller magnitude of the outwards traveling motion is again likely due to a longer scale-length density profile in the over-dense region of the target, due to greater ablation from the pre-pulse.

8.1.2 Low Density Foam Target

Chapter 6 presents results from a similar Doppler spectroscopy experiment to those performed on the silicate targets in the preceding chapters. The low density foam is difficult to directly compare to the previous experiments using silicate targets, as the equation of state and opacity complicate the issue somewhat. The results from the foam target are seen in Fig. 6.1. There is a similar pattern in the results to those seen in the preceding experiments with velocities of a similar magnitude to the low-contrast silicate-target experiment. There are additional reflections observed in

this experiment that were not observed in previous experiments. The additional reflections had much larger wavelength shifts than any of the previous experiments show. No explanation for these extra reflections could be found using the modelling attempted.

The HYADES simulations of the foam targets, while they do show some similarity to experimental results, are more difficult to draw firm conclusions about the reasons for some of the mismatches between experimental and simulation results. While 2D-3D effects are likely to be very significant in the formation of long scale-length pre-plasmas, there may be additional effects due to the microscopic structure of the foam. The attempt to emulate the foam structure using a modulated density profile showed little difference in pre-plasma scale-length compared to a flat profile. This approach, however, is limited due to it not being possible to take into account the finer structure of the foam. In reality, if there is additional laser penetration at early times in the pre-pulse interaction, the pre-plasma scale-length may indeed be comparable to the pre-plasma formed in the 1D HYADES case.

An EPOCH simulation was then intialised using a density profile from HYADES. The EPOCH results for the main-pulse interaction consistently show large regions of plasma disturbed by plasma instabilities. These instabilities appear to be post-solitons produced by anomalous red-shifting of the main-pulse. The alteration of the main-pulse may be caused by SRS or photon deceleration, as shown in Wigner transforms of the laser pulse as it traverses the disturbed region of the under-dense plasma. When Lagrangian codes are run using EPOCH output they do not reproduce the velocities seen in the experimental results in the over-dense plasma region. At lower densities, however, the post-soliton wall expansion appears similar in magnitude to the experimentally measured velocities.

EPOCH simulations run with a 2D density profile derived from a modified HYADES density profile show similar outwards velocities, at similar times, to those measured experimentally. These velocities occur as a result of post-soliton wall

shocks travelling into the over-dense plasma.

8.1.3 Future Work

There are several ways the three-stage modelling approach could be extended. The most obvious way would be to use a 2D or 3D radiation-hydrodynamics code to calculate pre-plasma density profile. The 1D calculation in chapter 4 gave reasonable results due to the small scale-length of the pre-plasma compared to the laser spot size. For the case with a larger pre-pulse (chapter 5) a 2D approach will provide an improvement in accuracy. A 2-3D PIC code may improve the accuracy of the results in the three stage modelling approach, but any possible improvement here may be offset by the difficulty in obtaining convergent results when using collisional routines. Any alternative hydrodynamics code would require sufficient flexibility to be able to input PIC results directly.

There are a number of areas which might be worth exploring further experimentally. The measurement of soliton expansion using probes rather than 3ω might give a better understanding of the evolution of wall-shocks over a longer period of time, given that they form in under-dense plasma. There also may be some merit in using high-harmonic generation to explore shock traversal through denser plasma. This approach has already been demonstrated in part,[72] and might be used in studying equations of states in extreme conditions.

8.2 Fast Electron Transport and Resistive Filamentation

The low-temperature resistivity has a critical effect on the growth of large-scale magnetic-field growth. A low resistivity at low temperatures decreases the heating rate at the edge of the beam. The longer the time spent at low temperatures the

larger the large-scale collimating magnetic field is able to grow. These large scale magnetic fields not only act to collimate the fast-electron beam produced in a laser-plasma interaction but to suppress the filamentation instability. The filamentation instability is suppressed in cases where the initial resistivity is below 0.5 $\mu\Omega m$ for the conditions described in chapter 6.

Bibliography

[1] J. T. Larsen, S. M. Lane. HYADES-A plasma hydrodynamics code for dense plasma studies. *Journal of Quantitative Spectroscopy and Radiative Transfer*, 51(1-2):179–186, 1994.

[2] T. D. Arber, K. Bennett, C. S. Brady, A. Lawrence-Douglas, M. G. Ramsay, N. J. Sircombe, *et al.*. Contemporary particle-in-cell approach to laser-plasma modelling. *Plasma Physics and Controlled Fusion*, 57(11):1–26, 2015.

[3] P. Gallant, Z. Jiang, C. Chien, P. Forget, F. Dorchies, J. Kieffer, *et al.*. Spectroscopy of solid density plasmas generated by irradiation of thin foils by a fs laser. *Journal of Quantitative Spectroscopy and Radiative Transfer*, 65(1):243–252, 2000.

[4] W. E. Lamb. Theory of an optical maser. *Physical Review*, 134(6A), 1964.

[5] L. E. Hargrove, R. L. Fork, M. A. Pollack. Locking of hene laser modes induced by synchronous intracavity modulation. *Applied Physics Letters*, 5(1):4–5, 1964.

[6] A. L. Schawlow, C. H. Townes. Infrared and optical masers. *Physical Review*, 112(6):1940–1949, 1958.

[7] C. E. Cook. Pulse Compression - Key to More Efficient Radar Transmission. *Proceedings of the IRE*, 48(3):310–316, 1960.

[8] D. Strickland, G. Mourou. Compression of amplified chirped optical pulses. *Optics Communications*, 56(3):219–221, 1985.

[9] P. Maine, D. Strickland, P. Bado, M. Pessot, G. Mourou. Generation of Ultrahigh Peak Power Pulses By Chirped Pulse Amplification. *IEEE Journal of Quantum Electronics*, 24(2):398–403, 1988.

[10] M. Perry, D. Pennington, B. Stuart, G. Tietbohl, J. Britten, C. Brown, *et al.*. Petawatt laser pulses. *Optics Letters*, 24(3):160–162, 1999.

[11] C. Edwards, J. Aldis, R. Allott, P. Brummitt, J. Collier, R. Clark, *et al.*. The vulcan Petawatt interaction facility. In C. Cavailler, G. Haddleton, M. Hugenschmidt, Herausgeber, *25th International Congress On High-Speed Photography and Photonics*, Band 4948 von *Proceedings Of The Society Of Photo-Optical Instrumentation Engineers (Spie)*, 444–451. nac Image Technol; Photron (Europe) Ltd; Photo Son Int Ltd; Vis Res Inc, 2003. 25th International Congress on High-Speed Photography and Photonics, BEAUNE, FRANCE, SEP 29-OCT 04, 2002.

[12] O. Chekhlov, E. J. Divall, K. Ertel, S. J. Hawkes, C. J. Hooker, I. N. Ross, *et al.*. Development of Petawatt laser amplification systems at the central laser facility - art. no. 67350J. In V. Panchenko, V. Golubev, A. Ionin, A. Chumakov, Herausgeber, *International Conference On Lasers, Applications, and Technologies 2007: High-Power Lasers and Applications*, Band 6735 von *Proceedings Of The Society Of Photo-Optical Instrumentation Engineers (Spie)*, J7350. Natl Acad Sci; Russian Acad Sci; Moscow State Univ, M V Lomonosov; BI Stepanov Inst Phys; Int Sci & Technol Ctr; Belarus Fdn Basic Res; Belarus Phys Soc; Russian Phys Soc; SPIE Russian Chapter, 2007. International Conference on Lasers, Applications, and Technologies, Minsk, BELARUS, MAY 28-JUN 01, 2007.

[13] C. J. Hooker, J. L. Collier, O. Chekhlov, R. Clarke, E. Divall, K. Ertel, *et al.*. The Astra Gemini project - A dual-beam petawatt Ti : Sapphire laser system. *Journal De Physique Iv*, 133:673–677, 2006. 4th International Conference on Inertial Fusion Sciences and Applications, Biarritz, FRANCE, SEP 04-09, 2005.

[14] S. C. Wilks, W. L. Kruer, M. Tabak, A. B. Langdon. Absorption Of Ultra-Intense Laser-Pulses. *Physical Review Letters*, 69(9):1383–1386, 1992.

[15] K. Shigemori, Y. Hironaka, H. Nagatomo, S. Fujioka, A. Sunahara, T. Kadono, *et al.*. Extremely high-pressure generation and compression with laser implosion plasmas. *Applied Physics Letters*, 102(18), 2013.

[16] M. Roth, A. Blazevic, M. Geissel, T. Schlegel, T. Cowan, M. Allen, *et al.*. Energetic ions generated by laser pulses: A detailed study on target properties. *Physical Review Special Topics-Accelerators and Beams*, 5(6), 2002.

[17] M. Borghesi, A. Mackinnon, D. Campbell, D. Hicks, S. Kar, P. Patel, *et al.*. Multi-MeV proton source investigations in ultraintense laser-foil interactions. *Physical Review Letters*, 92(5), 2004.

[18] S. Hatchett, C. Brown, T. Cowan, E. Henry, J. Johnson, M. Key, *et al.*. Electron, photon, and ion beams from the relativistic interaction of Petawatt laser pulses with solid targets. *Physics Of Plasmas*, 7(5, 2):2076–2082, 2000. 41st Annual Meeting of the Division of Plasma Physics of the American-Physical-Society, SEATTLE, WASHINGTON, NOV 15-19, 1999.

[19] M. Roth, I. Alber, V. Bagnoud, C. R. D. Brown, R. Clarke, H. Daido, *et al.*. Proton acceleration experiments and warm dense matter research using high power lasers. *Plasma Physics and Controlled Fusion*, 51(12), 2009. 36th European-Physical-Society Conference on Plasma Physics, Natl Palace Culture, Sofia, BULGARIA, JUN 29-JUL 03, 2009.

[20] A. Bell, J. Davies, S. Guerin, H. Ruhl. Fast-electron transport in high-intensity short-pulse laser-solid experiments. *Plasma Physics and Controlled Fusion*, 39(5):653–659, 1997.

[21] Y. Sentoku, E. Humieres, L. Romagnani, P. Audebert, J. Fuchs. Dynamic Control over Mega-Ampere Electron Currents in Metals Using Ionization-Driven Resistive Magnetic Fields. *Physical Review Letters*, 107(13), 2011.

[22] E. J. Reed, M. Soljac. Coherent Optical Photons from Shock Waves in Crystals. *Physical Review Letters*, 013904(January):1–4, 2006.

[23] A. Adak, A. P. L. Robinson, P. K. Singh, G. Chatterjee, A. D. Lad, J. Pasley, *et al.*. Terahertz Acoustics In Hot Dense Laser Plasmas. *Physical Review Letters*, 114(11), 2015.

[24] T. Afsharrad, S. E. Coe, O. Willi, M. Desselberger. Evidence Of Stimulated Raman-Scattering Occurring In Laser Filaments In Long-Scale-Length Plasmas. *Physics Of Fluids B-Plasma Physics*, 4(5):1301–1322, 1992.

[25] M. R. Amin, C. Capjack, P. Frycz, W. Rozmus, V. T. Tikhonchuk. 2-Dimensional Studies Of Stimulated Brillouin-Scattering, Filamentation, and Self-Focusing Instabilities Of Laser-Light In Plasmas. *Physics Of Fluids B-Plasma Physics*, 5(10):3748–3764, 1993.

[26] A. C. L. Chian, F. B. Rizzato. Coupling Of Electromagnetic Filamentation Instability and Electrostatic Langmuir Parametric-Instabilities In Laser-Plasma Interactions. *Journal Of Plasma Physics*, 51(1):61–73, 1994.

[27] C. D. Gregory, B. Loupias, J. Waugh, P. Barroso, S. Bouquet, E. Brambrink, *et al.*. Astrophysical jet experiments. *Plasma Physics and Controlled Fusion*, 50(12):124039, 2008.

[28] C. D. Gregory, J. Howe, B. Loupias, S. Myers, M. M. Notley, Y. Sakawa, *et al.*. Astrophysical Jet Experiments with Colliding Laser-produced Plasmas. *The Astrophysical Journal*, 676(1):420–426, 2008.

[29] Y. Kuramitsu, Y. Sakawa, J. N. Waugh, C. D. Gregory, T. Morita, S. Dono, *et al.*. Jet Formation in Counterstreaming Collisionless Plasmas. *The Astrophysical Journal*, 707(2):L137–L141, 2009.

[30] G. Chatterjee, P. K. Singh, A. Adak, A. D. Lad, G. R. Kumar. High-resolution measurements of the spatial and temporal evolution of megagauss magnetic fields created in intense short-pulse laser-plasma interactions. *Review Of Scientific Instruments*, 85(1), 2014.

[31] S. Mondal, V. Narayanan, W. J. Ding, A. D. Lad, B. Hao, S. Ahmad, *et al.*. Direct observation of turbulent magnetic fields in hot, dense laser produced plasmas. *Proceedings Of The National Academy Of Sciences Of The United States Of America*, 109(21):8011–8015, 2012.

[32] K. M. Schoeffler, N. F. Loureiro, R. A. Fonseca, L. O. Silva. The generation of magnetic fields by the Biermann battery and the interplay with the Weibel instability. *Physics Of Plasmas*, 23(5), 2016. 57th Annual Meeting of the APS-Division-of-Plasma-Physics (DPP), Savannath, GA, NOV 16-20, 2015.

[33] K. V. Modi, P. P. Tiwary, R. K. Singh, V. R. Satsangi, R. P. Sharma. Filamentation of magnetosonic wave and generation of magnetic turbulence in laser plasma interaction. *Physics Of Plasmas*, 21(10), 2014.

[34] G. Gregori, A. Ravasio, C. D. Murphy, K. Schaar, A. Baird, A. R. Bell, *et al.*. Generation of scaled protogalactic seed magnetic fields in laser-produced shock waves. *Nature*, 481(7382):480–483, 2012.

[35] Y. G. Kang, K. Nishihara, H. Nishimura, H. Takabe, A. Sunahara, T. Norimatsu, *et al.*. Blast-wave-sphere interaction using a laser-produced plasma: An experiment motivated by supernova 1987A. *Phys. Rev. E*, 64:047402, 2001.

[36] M. J. Edwards, A. J. MacKinnon, J. Zweiback, K. Shigemori, D. Ryutov, A. M. Rubenchik, *et al.*. Investigation of Ultrafast Laser-Driven Radiative Blast Waves. *Phys. Rev. Lett.*, 87:085004, 2001.

[37] F. Fiuza, R. A. Fonseca, J. Tonge, W. B. Mori, L. O. Silva. Weibel-Instability-Mediated Collisionless Shocks in the Laboratory with Ultraintense Lasers. *Phys. Rev. Lett.*, 108:235004, 2012.

[38] L. Romagnani, S. V. Bulanov, M. Borghesi, P. Audebert, J. C. Gauthier, K. Löwenbrück, *et al.*. Observation of Collisionless Shocks in Laser-Plasma Experiments. *Phys. Rev. Lett.*, 101:025004, 2008.

[39] A. Burrows, E. Livne, L. Dessart, C. D. Ott, J. Murphy. A New Mechanism for Core-Collapse Supernova Explosions. *The Astrophysical Journal*, 640(2):878, 2006.

[40] R. A. Snavely, M. H. Key, S. P. Hatchett, I. E. Cowan, M. Roth, T. W. Phillips, *et al.*. Intense high-energy proton beams from petawatt-laser irradiation of solids. *Physical Review Letters*, 85(14):2945–2948, 2000.

[41] S. C. Wilks, A. B. Langdon, T. E. Cowan, M. Roth, M. Singh, S. Hatchett, *et al.*. Energetic proton generation in ultra-intense laser-solid interactions. *Physics of Plasmas*, 8(2):542–549, 2001.

[42] C. Perego, A. Zani, D. Batani, M. Passoni. Extensive comparison among Target Normal Sheath Acceleration theoretical models. *Nuclear Instruments and Methods in Physics Research Section A: Accelerators, Spectrometers, Detectors and Associated Equipment*, 653(1):89–93, 2011.

[43] V. Tikhonchuk. Physics of laser-assisted ion acceleration. *Nuclear Instruments and Methods in Physics Research Section A: Accelerators, Spectrometers, Detectors and Associated Equipment*, 620(1):1–13, 2010.

[44] H. Daido, M. Nishiuchi, A. S. Pirozhkov. Review of laser-driven ion sources and their applications. *Reports on progress in physics. Physical Society (Great Britain)*, 75(5):056401, 2012.

[45] G. Turchetti, V. Malka, M. Giovannozzi. Ions acceleration with high power lasers: Physics and applications 15–18 June 2009, Senigallia (AN), Italy. *Nuclear Instruments and Methods in Physics Research Section A: Accelerators, Spectrometers, Detectors and Associated Equipment*, 620(1):vii–viii, 2010.

[46] P. Bolton, T. Hori, H. Kiriyama, M. Mori, H. Sakaki, K. Sutherland, *et al.*. Toward integrated laser-driven ion accelerator systems at the photo-medical research center in Japan. *Nuclear Instruments and Methods in Physics Research Section A: Accelerators, Spectrometers, Detectors and Associated Equipment*, 620(1):71–75, 2010.

[47] S. V. Bulanov, V. S. Khoroshkov. Feasibility of using laser ion accelerators in proton therapy. *Plasma Physics Reports*, 28(5):453–456, 2002.

[48] S. S. Bulanov, A. Brantov, V. Y. Bychenkov, V. Chvykov, G. Kalinchenko, T. Matsuoka, *et al.*. Accelerating protons to therapeutic energies with ultraintense, ultraclean, and ultrashort laser pulses. *Medical Physics*, 35(5):1770, 2008.

[49] A. Yogo, T. Maeda, T. Hori, H. Sakaki, K. Ogura, M. Nishiuchi, *et al.*. Development of laser-driven quasi-monoenergetic proton beam line for radiobiology. *Nuclear Instruments and Methods in Physics Research Section A: Accelerators, Spectrometers, Detectors and Associated Equipment*, 653(1):189–192, 2011.

[50] M. Grech, S. Skupin, R. Nuter, L. Gremillet, E. Lefebvre. High-quality ion beams from nanometric double-layer targets and their application to hadron-therapy. *Nuclear Instruments and Methods in Physics Research Section A: Accelerators, Spectrometers, Detectors and Associated Equipment*, 620(1):63–66, 2010.

[51] M. Suzuki, M. Watanabe, T. Kanai, Y. Kase, F. Yatagai, T. Kato, *et al.*. LET dependence of cell death, mutation induction and chromatin damage in human cells irradiated with accelerated carbon ions. *Advances in space research : the official journal of the Committee on Space Research (COSPAR)*, 18:127–136, 1996.

[52] S. Bagchi, P. P. Kiran, K. Yang, A. M. Rao, M. K. Bhuyan, M. Krishnamurthy, *et al.*. Bright, low debris, ultrashort hard x-ray table top source using carbon nanotubes. *Physics of Plasmas*, 18(1), 2011.

[53] A. S. Sandhu, G. R. Kumar. Laser-Pulse-Induced Second-Harmonic and Hard X-Ray Emission: Role of Plasma-Wave Breaking. *Physical Review Letters*, 95(2):025005, 2005.

[54] E. J. Reed, M. R. Armstrong, K. Kim, M. Soljačić, R. Gee, J. H. Glownia, *et al.*. Terahertz radiation from shocked materials. *Materials Today*, 10(7-8):44–50, 2007.

[55] G.-Q. Liao, Y.-T. Li, Y.-H. Zhang, H. Liu, X.-L. Ge, S. Yang, *et al.*. Demonstration of Coherent Terahertz Transition Radiation from Relativistic Laser-Solid Interactions. *Physical Review Letters*, 116(20), 2016.

[56] A. G. Davies, A. D. Burnett, W. Fan, E. H. Linfield, J. E. Cunningham. Terahertz spectroscopy of explosives and drugs. *Materials Today*, 11(3):18–26, 2008.

[57] C. Regan, T. Schlegel, V. T. Tikhonchuk, J. J. Honrubia, J.-L. Feugeas, P. Nicolaï. Cone-guided fast ignition with ponderomotively accelerated carbon ions. *Plasma Physics and Controlled Fusion*, 53(4):045014, 2011.

[58] M. Ogawa, U. Neuner, a. Sakumi, J. Hasegawa, K. Sasa, K. Horioka, *et al.*. Heavy ion beam inertial confinement fusion studies in TIT. *Fusion Engineering and Design*, 44(1-4):279–283, 1999.

[59] K. Long, N. Tahir. Heavy ion beam ICF fusion: The thermodynamics of ignition and the achievement of high gain in ICF fusion targets. *Physics Letters A*, 91(9):451–456, 1982.

[60] B. Hegelich, D. Jung, B. Albright, J. Fernandez, D. Gautier, C. Huang, *et al.*. Experimental demonstration of particle energy, conversion efficiency and spectral shape required for ion-based fast ignition. *Nuclear Fusion*, 51(8):083011, 2011.

[61] J. Meyer-ter Vehn. Fast ignition of ICF targets: an overview. *Plasma Physics and Controlled Fusion*, 43:A113–A125, 2001.

[62] A. G. MacPhee, L. Divol, A. J. Kemp, K. U. Akli, F. N. Beg, C. D. Chen, *et al.*. Limitation on prepulse level for cone-guided fast-ignition inertial confinement Fusion. *Physical Review Letters*, 104, 2010.

[63] S. Atzeni, J. Meyer-Ter-Vehn. *The physics of inertial fusion : beam plasma interaction, hydrodynamics, hot dense matter*. Oxford University Press, Oxford, U.K, 2009.

[64] J. I. Castor. *Radiation Hydrodynamics*. Cambridge University Press, 2007.

[65] P. Gibbon. *Short Pulse Laser Interactions with Matter: An Introduction*. World Scientific Publishing Company, 2005.

[66] J. F. Luciani, P. Mora, J. Virmont. Nonlocal heat transport due to steep temperature gradients. *Physical Review Letters*, 51(18):1664–1667, 1983.

[67] T. Tajima. *Computational Plasma Physics: With Applications To Fusion and Astrophysics (Frontiers in Physics)*. Westview Press, 2004.

[68] Y. Sentoku, A. J. Kemp. Numerical methods for particle simulations at extreme densities and temperatures: Weighted particles, relativistic collisions and reduced currents. *Journal of Computational Physics*, 227(14):6846–6861, 2008.

[69] A. Pukhov, J. Meyer-ter Vehn. Laser Hole Boring into Overdense Plasma and Relativistic Electron Currents for Fast Ignition of ICF Targets. *Physical review letters*, 79(14):2686–2689, 1997.

[70] A. D. Lad, S. Mondal, V. Narayanan, S. Ahmed, P. P. Rajeev, A. P. L. Robinson, *et al.*. Real-time ultrafast dynamics of dense, hot matter measured by pump-probe Doppler spectrometry. *Sixth International Conference On Inertial Fusion Sciences And Applications, Parts 1-4*, 244, 2010.

[71] S. Mondal, A. D. Lad, S. Ahmed, V. Narayanan, J. Pasley, P. P. Rajeev, *et al.*. Doppler Spectrometry for Ultrafast Temporal Mapping of Density Dynamics in Laser-Induced Plasmas. *Physical Review Letters*, 105(10):105002, 2010.

[72] K. U. Akli, S. B. Hansen, A. J. Kemp, R. R. Freeman, F. N. Beg, D. C. Clark, *et al.*. Laser heating of solid matter by light-pressure-driven shocks at ultrarelativistic intensities. *Physical Review Letters*, 100(16), 2008.

[73] M. E. Glinsky. Regimes of suprathermal electron transport. *Physics of Plasmas*, 2(7):2796, 1995.

[74] M. Storm, A. A. Solodov, J. F. Myatt, D. D. Meyerhofer, C. Stoeckl, C. Mileham, *et al.*. High-current, relativistic electron-beam transport in metals and the role of magnetic collimation. *Physical Review Letters*, 102(23):1–4, 2009.

[75] A. Bell, R. Kingham. Resistive Collimation of Electron Beams in Laser-Produced Plasmas. *Physical Review Letters*, 91(3):035003, 2003.

[76] M. Tatarakis, F. N. Beg, E. L. Clark, A. E. Dangor, R. D. Edwards, R. G. Evans, *et al.*. Propagation instabilities of high-intensity laser-produced electron beams. *Physical Review Letters*, 90(May):175001, 2003.

[77] P. McKenna, A. P. L. Robinson, D. Neely, M. P. Desjarlais, D. C. Carroll, M. N. Quinn, *et al.*. Effect of lattice structure on energetic electron transport in solids irradiated by ultraintense laser pulses. *Physical Review Letters*, 106(18):185004, 2011.

[78] L. Gremillet, G. Bonnaud, F. Amiranoff. Filamented transport of laser-generated relativistic electrons penetrating a solid target. *Physics of Plasmas*, 9(3):941, 2002.

[79] J. M. Hill, M. H. Key, S. P. Hatchett, R. R. Freeman. Beam-Weibel filamentation instability in near-term and fast-ignition experiments. *Physics of Plasmas*, 12(8):1–8, 2005.

[80] A. P. L. Robinson, R. J. Kingham, C. P. Ridgers, M. Sherlock. Effect of transverse density modulations on fast electron transport in dense plasmas. *Plasma Physics and Controlled Fusion*, 50(6):065019, 2008.

[81] D. A. Maclellan, D. C. Carroll, R. J. Gray, N. Booth, M. Burza, M. P. Desjarlais, *et al.*. Annular fast electron transport in silicon arising from low-temperature resistivity. *Physical Review Letters*, 111(9), 2013.

[82] A. Adak, P. K. Singh, D. R. Blackman, A. D. Lad, G. Chatterjee, J. Pasley, *et al.*. Controlling femtosecond-laser-driven shock-waves in hot, dense plasma. *Physics of Plasmas*, 24(7):072702, 2017.

[83] A. Adak, D. R. Blackman, G. Chatterjee, P. Kumar Singh, A. D. Lad, P. Brijesh, *et al.*. Ultrafast dynamics of a near-solid-density layer in an intense femtosecond laser-excited plasma. *Physics of Plasmas*, 21(6):062704, 2014.

[84] D. R. Blackman, A. P. L. Robinson, J. Pasley. Role of low temperature resistivity on fast electron transport in disordered aluminium and copper. *Physics of Plasmas*, 22(8):083108, 2015.

[85] J. Huba. *NRL plasma formulary*. Naval Research Lab., Washington, DC, 2016.

[86] L. Tonks, I. Langmuir. Oscillations in Ionized Gases. *Phys. Rev.*, 33:195–210, 1929.

[87] R. Fitzpatrick. *Plasma physics : an introduction*. CRC Press, Taylor & Francis Group, Boca Raton, 2015.

[88] R. Dendy. *Plasma Physics: An Introductory Course*. Cambridge University Press, 1995.

[89] J. Colvin, J. Larsen. *Extreme physics : properties and behavior of matter at extreme conditions*. Cambridge University Press, Cambridge, United Kingdom New York, 2014.

[90] J. C. Kieffer, J. P. Matte, S. Belair, M. Chaker, P. Audebert, H. Pepin, *et al.*. Absorption Of An Ultrashort Laser-Pulse In Very Steep Plasma-Density Gradients. *IEEE Journal Of Quantum Electronics*, 25(12):2640–2647, 1989.

[91] R. Fedosejevs, R. Ottmann, R. Sigel, G. Kühnle, S. Szatmari, F. Schäfer. Absorption of femtosecond laser pulses in high-density plasma. *Physical Review Letters*, 64(11):1250–1253, 1990.

[92] H. M. Milchberg, R. R. Freeman. Light absorption in ultrashort scale length plasmas. *Journal of the Optical Society of America B*, 6(7):1351, 1989.

[93] F. Brunel. Not-So-Resonant, Resonant Absorption. *Physical Review Letters*, 59(1):52–55, 1987.

[94] E. Weibel. Anomalous Skin Effect In A Plasma. *Physics Of Fluids*, 10(4):741–&, 1967.

[95] W. Kruer. *The Physics Of Laser Plasma Interactions (Frontiers in Physics)*. Westview Press, 2003.

[96] P. McKenna, D. Neely, R. Bingham, D. Jaroszynski. *Laser-Plasma Interactions and Applications (Scottish Graduate Series)*. Springer, 2013.

[97] H. Barr, L. Hill. Stimulated scattering and harmonic generation from relativistically intense laser light in plasma. *Physics Of Plasmas*, 10(4):1135–1145, 2003.

[98] P. Kaw, G. Schmidt, T. Wilcox. Filamentation And Trapping Of Electromagnetic Radiation In Plasmas. *Physics Of Fluids*, 16(9):1522–1525, 1973.

[99] P. E. Young, H. A. Baldis, R. P. Drake, E. M. Campbell, K. G. Estabrook. Direct Evidence of Ponderomotive Filamentation in a Laser-Produced Plasma. *Phys. Rev. Lett.*, 61:2336–2339, 1988.

[100] A. B. Borisov, A. V. Borovskii, V. V. Korobkin, A. M. Prokhorov, O. B. Shiriaev, X. M. Shi, *et al.*. Observation of relativistic and charge-displacement self-channeling of intense subpicosecond ultraviolet (248 nm) radiation in plasmas. *Physical Review Letters*, 68:2309–2312, 1992.

[101] W. B. Mori, C. Joshi, J. M. Dawson, D. W. Forslund, J. M. Kindel. Evolution of self-focusing of intense electromagnetic waves in plasma. *Physical Review Letters*, 60:1298–1301, 1988.

[102] G.-Z. Sun, E. Ott, Y. Lee, P. Guzdar. Self-focusing of short intense pulses in plasmas. *Physics of Fluids*, 30:526–532, 1987.

[103] A. Upadhyay, V. Tripathi, A. Sharma, H. Pant. Asymmetric self-focusing of a laser pulse in plasma. *Journal Of Plasma Physics*, 68(1):75–80, 2002.

[104] F. W. Perkins, E. J. Valeo. Thermal Self-Focusing of Electromagnetic Waves in Plasmas. *Physical Review Letters*, 32:1234–1237, 1974.

[105] Ghanshyam, V. Tripathi. Self-Focusing And Filamentation Of Laser-Beams In Collisional Plasmas With Finite Thermal Conduction. *Journal Of Plasma Physics*, 49(2):243–253, 1993.

[106] C. E. Max, J. Arons, A. B. Langdon. Self-Modulation and Self-Focusing of Electromagnetic Waves in Plasmas. *Physical Review Letters*, 33:209–212, 1974.

[107] A. Pukhov. Strong field interaction of laser radiation. *Reports on Progress in Physics*, 66:47–101, 2003.

[108] F. H. Shu. *The Physics of Astrophysics Volume II: Gas Dynamics (A Series of Books in Astronomy)*. University Science books, 2009.

[109] E. L. Lindman. Dispersion relation for computer-simulated plasmas. *Journal of Computational Physics*, 5(1):13–22, 1970.

[110] L. Chen, A. Bruce Langdon, C. K. Birdsall. Reduction of the grid effects in simulation plasmas. *Journal of Computational Physics*, 14(2):200–222, 1974.

[111] H. Okuda. Nonphysical noises and instabilities in plasma simulation due to a spatial grid. *Journal of Computational Physics*, 10(3):475–486, 1972.

[112] E. Cormier-Michel, B. A. Shadwick, C. G. R. Geddes, E. Esarey, C. B. Schroeder, W. P. Leemans. Unphysical kinetic effects in particle-in-cell modeling of laser wakefield accelerators. *Physical Review E - Statistical, Nonlinear, and Soft Matter Physics*, 78(1):016404, 2008.

[113] S. Lee, T. Katsouleas, R. Hemker, W. B. Mori. Simulations of a meter-long plasma wakefield accelerator. *Physical Review E - Statistical Physics, Plasmas, Fluids, and Related Interdisciplinary Topics*, 61(6 B):7014–7021, 2000.

[114] R. A. Fonseca, L. O. Silva, F. S. Tsung, V. K. Decyk, W. Lu, C. Ren, *et al.*. OSIRIS: A Three-Dimensional, Fully Relativistic Particle in Cell Code for Modeling Plasma Based Accelerators. In Sloot, P and Tan, CJK and Dongarra, JJ and Hoekstra, AG, Herausgeber, *Computational Science-ICCS 2002, Pt III, Proceedings*, Band 2331 von *Lecture Notes In Computer Science*, 342–351. Univ Amsterdam, Sect Computat Sci; SHARCNET, Canada; Univ Tennessee, Dept Comp Sci; Power Comp & Commun BV; Elsevier Sci Publ; Springer Verlag; HPCN Fdn; Natl Supercomp Facilities; Sun Microsyst Inc; Queens Univ, Sch Comp Sci, 2002.

[115] D. R. Welch, D. V. Rose, M. E. Cuneo, R. B. Campbell, T. A. Mehlhorn. Integrated simulation of the generation and transport of proton beams from laser-target interaction. *Physics of Plasmas*, 13(6), 2006.

[116] D. R. Welch, D. V. Rose, R. E. Clark, C. B. Mostrom, W. A. Stygar, R. J. Leeper. Fully kinetic particle-in-Cell simulations of a deuterium gas puff z pinch. *Physical Review Letters*, 103(25):18–21, 2009.

[117] H. Fehske, R. Schneider, A. Weiße, D. Tskhakaya, Herausgeber. *The Particle-in-Cell Method*, 161–189. Springer Berlin Heidelberg, Berlin, Heidelberg, 2008.

[118] J. A. Roden, S. D. Gedney. "Convolution PML (CPML): An efficient FDTD implementation of the CFS-PML for arbitrary media". *Microwave and Optical Technology Letters*, 27(5):334–339, 2000.

[119] A. Thomas, M. Tzoufras, A. Robinson, R. Kingham, C. Ridgers, M. Sherlock, *et al.*. A review of Vlasov–Fokker–Planck numerical modeling of inertial confinement fusion plasma. *Journal of Computational Physics*, 231(3):1051–1079, 2012.

[120] G. Pert. Algorithms for the self-consistent generation of magnetic fields in plasmas. *Journal of Computational Physics*, 43(1):111–163, 1981.

[121] J. VonNeumann, R. D. Richtmyer. A Method for the Numerical Calculation of Hydrodynamic Shocks. *Journal of Applied Physics*, 21(3):232, 1950.

[122] P. J. Roache. On artificial viscosity. *Journal of Computational Physics*, 10(2):169–184, 1972.

[123] L. Spitzer, R. Härm. Transport phenomena in a completely ionized gas. *Physical Review*, 89(5):977–981, 1953.

[124] S. Eliezer. *The Interaction of High-Power Lasers with Plasmas (Series in Plasma Physics)*. CRC Press, 2002.

[125] G. C. Pomraning. *The Equations of Radiation Hydrodynamics (Dover Books on Physics)*. Dover Publications, 2005.

[126] T. W. Johnston, J. M. Dawson. Correct values for high-frequency power absorption by inverse bremsstrahlung in plasmas. *The Physics of Fluids*, 16(5):722, 1973.

[127] J. Larsen. *Foundations of High-Energy-Density Physics: Physical Processes of Matter at Extreme Conditions*. Cambridge University Press, 2017.

[128] G. J. Tallents. *An Introduction to the Atomic and Radiation Physics of Plasmas*. Cambridge University Press, 2018.

[129] B. J. Crowley. Average-atom quantum-statistical cell model for hot plasma in local thermodynamic equilibrium over a wide range of densities. *Physical Review A*, 41(4):2179–2191, 1990.

[130] R. J. Kingham, M. Sherlock, C. P. Ridgers, R. G. Evans. Vlasov-Fokker-Planck simulations of fast-electron transport with hydrodynamic plasma response. *Journal of Physics: Conference Series*, 244(2):022042, 2010.

[131] D. A. MacLellan, D. C. Carroll, R. J. Gray, A. P. L. Robinson, M. P. Desjarlais, D. Neely, *et al.*. Influence of laser-drive parameters on annular fast electron transport in silicon. *Plasma Physics and Controlled Fusion*, 56(8):084002, 2014.

[132] R. J. Mason, C. W. Cranfill. Hybrid Two-Dimensional Electron Transport in Self-Consistent Electromagnetic Fields. *IEEE Transactions on Plasma Science*, 14(1):45–52, 1986.

[133] C. Cranfill, B. JU, G. SR. A Time-Implicit Monte-Carlo Collision Algorithm For Particle-In-Cell Electron-Transport Models. *Journal Of Computational Physics*, 66(1):239–249, 1986.

[134] R. Shanny, D. JM, G. JM. 1-Dimensional Model Of A Lorentz Plasma. *Physics Of Fluids*, 10(6):1281–&, 1967.

[135] B. Fryxell, K. Olson, P. Ricker, F. X. Timmes, M. Zingale, D. Q. Lamb, *et al.*. FLASH: An Adaptive Mesh Hydrodynamics Code for Modeling Astrophysical Thermonuclear Flashes. *The Astrophysical Journal Supplement Series*, 131(1):273–334, 2000.

[136] K. U. Akli, C. Orban, D. Schumacher, M. Storm, M. Fatenejad, D. Lamb, *et al.*. Coupling of high-intensity laser light to fast electrons in cone-guided fast ignition. *Physical Review E*, 86(6, 2), 2012.

[137] P. Radha, V. Goncharov, T. Collins, J. Delettrez, Y. Elbaz, V. Glebov, *et al.*. Two-dimensional simulations of plastic-shell, direct-drive implosions on OMEGA. *Physics Of Plasmas*, 12(3), 2005.

[138] P. Radha, T. Collins, J. Delettrez, Y. Elbaz, R. Epstein, V. Glebov, *et al.*. Multidimensional analysis of direct-drive, plastic-shell implosions on OMEGA. *Physics Of Plasmas*, 12(5), 2005. 46th Annual Meeting of the Division of Plasma Physics of the American-Physical-Society, Savannah, GA, NOV 15-19, 2004.

[139] A. A. Solodov, K. S. Anderson, R. Betti, V. Gotcheva, J. Myatt, J. A. Delettrez, *et al.*. Integrated simulations of implosion, electron transport, and heating for direct-drive fast-ignition targets. *Physics Of Plasmas*, 16(5), 2009. 50th Annual Meeting of the Division of Plasma Physics of the American-Physical-Society, Dallas, TX, FEB 01, 2008.

[140] J. R. Davies, J. S. Green, P. A. Norreys. Electron beam hollowing in laser solid interactions. *Plasma Physics and Controlled Fusion*, 48(8):1181–1199, 2006.

[141] C. A. McCoy, M. C. Gregor, D. N. Polsin, D. E. Fratanduono, P. M. Celliers, T. R. Boehly, *et al.*. Shock-wave equation-of-state measurements in fused silica up to 1600 GPa. *Journal of Applied Physics*, 119(21), 2016.

[142] C. A. McCoy, M. C. Gregor, D. N. Polsin, D. E. Fratanduono, P. M. Celliers, T. R. Boehly, *et al.*. Measurements of the sound velocity of shock-compressed liquid silica to 1100 GPa. *Journal of Applied Physics*, 120(23), 2016.

[143] R. Ramis, K. Eidmann, J. Meyer-Ter-Vehn, S. Hüller. MULTI-fs - A computer code for laser-plasma interaction in the femtosecond regime. *Computer Physics Communications*, 183(3):637–655, 2012.

[144] K. Eidmann, J. Meyer-ter Vehn, T. Schlegel, S. Hüller. Hydrodynamic simulation of subpicosecond laser interaction with solid-density matter. *Physical Review E - Statistical Physics, Plasmas, Fluids, and Related Interdisciplinary Topics*, 62(1 B):1202–1214, 2000.

[145] G. Guethlein, M. Foord, D. Price. Electron Temperature Measurements of Solid Density Plasmas Produced by Intense Ultrashort Laser Pulses. *Physical Review Letters*, 77(6):1055–1058, 1996.

[146] B. Yaakobi, T. C. Bristow. Measurement of reduced thermal conduction in (layered) laser-target experiments. *Physical Review Letters*, 38(7):350–353, 1977.

[147] G. Spindler, Y.-l. Teng, G. Tsakiris, S. Witkowski, M. P.-n. I.-t. Quantenoptik. Interaction of 1.3-μ laser radiation with thin foil targets. *Physical Review A*, 30(5), 1984.

[148] A. Zigler, P. G. Burkhalter, D. J. Nagel, M. D. Rosen, K. Boyer, G. Gibson, *et al.*. Measurement of energy penetration depth of subpicosecond laser energy into solid density matter. *Applied Physics Letters*, 59(5):534–536, 1991.

[149] J. Osterholz, F. Brandl, M. Cerchez, T. Fischer, D. Hemmers, B. Hidding, *et al.*. Extreme ultraviolet emission from dense plasmas generated with sub-10-fs laser pulses. *Physics of Plasmas*, 15(10), 2008.

[150] F. Harris. On the use of windows for harmonic analysis with the discrete Fourier transform. *Proceedings of the IEEE*, 66(1):51–83, 1978.

[151] R. B. Blackman, J. W. Tukey. The measurement of power spectra from the point of view of communication engineering - Part I. *Bell System Technical Journal*, 37:485–569, 1958.

[152] J. G. Moreau, E. D'Humières, R. Nuter, V. T. Tikhonchuk. Stimulated Raman scattering in the relativistic regime in near-critical plasmas. *Physical Review E - Statistical, Nonlinear, and Soft Matter Physics*, 95(1):1–9, 2017.

[153] S. C. Wilks, W. L. Kruer, E. A. Williams, P. Amendt, D. C. Eder. Stimulated Raman backscatter in ultraintense, short pulse laser-plasma interactions. *Physics of Plasmas*, 2(1):274–279, 1995.

[154] G. P. Schurtz, P. D. Nicolaï, M. Busquet. A nonlocal electron conduction model for multidimensional radiation hydrodynamics codes. *Physics of Plasmas*, 7(10):4238–4249, 2000.

[155] A. R. Bell, R. G. Evans, D. J. Nicholas. Electron Energy-Transport In Steep Temperature-Gradients In Laser-Produced Plasmas. *Physical Review Letters*, 46(4):243–246, 1981.

[156] J. R. Albritton, E. A. Williams, I. B. Bernstein, K. B. Swartz. Nonlocal Electron Heat-Transport By Not Quite Maxwell-Boltzmann Distributions. *Physical Review Letters*, 57(15):1887–1890, 1986.

[157] A. R. Bell. Non-Spitzer Heat-Flow In A Steadily Ablating Laser-Produced Plasma. *Physics Of Fluids*, 28(6):2007–2014, 1985.

[158] J. R. Albritton. Laser-Absorption and Heat-Transport By Non-Maxwell-Boltzmann Electron Distributions. *Physical Review Letters*, 50(26):2078–2081, 1983.

[159] G. Sarri, D. K. Singh, J. R. Davies, F. Fiuza, K. L. Lancaster, E. L. Clark, *et al.*. Observation of Postsoliton Expansion Following Laser Propagation

through an Underdense Plasma. *Physical Review Letters*, 105(17):175007, 2010.

[160] G. Sarri, S. Kar, L. Romagnani, S. V. Bulanov, C. A. Cecchetti, M. Galimberti, *et al.*. Observation of plasma density dependence of electromagnetic soliton excitation by an intense laser pulse. *Physics of Plasmas*, 18(8), 2011.

[161] L. M. R. Gartside, G. J. Tallents, A. K. Rossall, E. Wagenaars, D. S. Whittaker, M. Kozlová, *et al.*. Extreme ultraviolet interferometry of laser plasma material between the critical and ablation surfaces. *High Energy Density Physics*, 7(2):91–97, 2011.

[162] T. Kapin, J. Limpouch, R. Liska. Hydrodynamic simulations of laser interactions with low – density foams. *Czechoslovak Journal of Physics*, 56:493–499, 2006.

[163] S. Y. Gus'kov, V. B. Rozanov. Interaction of laser radiation with a porous medium and formation of a nonequilibrium plasma. *Quantum Electronics*, 27(8):696–701, 1997.

[164] S. Y. Gus'kov, A. Caruso, V. B. Rozanov, C. Strangio. Interaction of a high-power laser pulse with supercritical-density porous materials. *Quantum Electronics*, 30(3):191–206, 2000.

[165] A. Caruso, C. Strangio, S. Y. Gus'kov, V. B. Rozanov. Interaction experiments of laser light with low density supercritical foams at the AEEF ABC facility. *Laser and Particle Beams*, 18(1):25–34, 2000.

[166] J. Velechovsky, J. Limpouch, R. Liska, V. Tikhonchuk. Hydrodynamic modeling of laser interaction with micro-structured targets. *Plasma Physics and Controlled Fusion*, 58(9):095004, 2016.

[167] M. Cipriani, S. Gus'kov, R. D. Angelis, P. Andreoli, F. Consoli, G. Cristofari, *et al.*. Powerful laser pulse absorption in partly homogenized foam plasma. *Journal of Instrumentation*, 11(03):C03062–C03062, 2016.

[168] T. Iwawaki, H. Habara, S. Baton, K. Morita, J. Fuchs, S. Chen, *et al.*. Collimated fast electron beam generation in critical density plasma. *Physics of Plasmas*, 21(11), 2014.

[169] Y. T. Li, Z. M. Sheng, Y. Y. Ma, Z. Jin, J. Zhang, Z. L. Chen, *et al.*. Demonstration of bulk acceleration of ions in ultraintense laser interactions with low-density foams. *Physical Review E - Statistical, Nonlinear, and Soft Matter Physics*, 72(6), 2005.

[170] D. Faith, C. J. Horsfield, W. Nazarov. Characterization of pore size of trimethylol propane triacrylate (TMPTA) polymer foam by pulsed sputter coating and SEM analysis. *Journal of Materials Science*, 41(13):3973–3977, 2006.

[171] S. Y. Gus'kov, J. Limpouch, P. Nicolaï, V. T. Tikhonchuk. Laser-supported ionization wave in under-dense gases and foams. *Physics of Plasmas*, 18(10), 2011.

[172] S. Kahaly, S. K. Yadav, W. M. Wang, S. Sengupta, Z. M. Sheng, A. Das, *et al.*. Near-complete absorption of intense, ultrashort laser light by sub-?? gratings. *Physical Review Letters*, 101(14):3–6, 2008.

[173] J. T. Mendonça, R. Bingham. Photon acceleration as a scattering process. *Plasma Physics and Controlled Fusion*, 57(4):044011, 2015.

[174] C. D. Murphy, R. Trines, J. Vieira, A. J. W. Reitsma, R. Bingham, J. L. Collier, *et al.*. Evidence of photon acceleration by laser wake fields. *Physics of Plasmas*, 13(3), 2006.

[175] N. M. Naumova, S. V. Bulanov, T. Z. Esirkepov, D. Farina, K. Nishihara, F. Pegoraro, *et al.*. Formation of Electromagnetic Postsolitons in Plasmas. *Physical Review Letters*, 87(18):185004, 2001.

[176] B. Zhu, Y.-C. Wu, K.-G. Dong, W. Hong, J. Teng, W.-M. Zhou, *et al.*. Observation of a strong correlation between electromagnetic soliton formation and relativistic self-focusing for ultra-short laser pulses propagating through an under-dense plasma. *Physics of Plasmas*, 19(10):102304, 2012.

[177] V. A. Kozlov, A. G. Litvak, V. Suvorov. Envelope solitons of relativistic strong electromagnetic waves. *Journal of Experimental and Theoretical Physics*, 49(January):75–80, 1979.

[178] Y. Liu, O. Klimo, T. Z. Esirkepov, S. V. Bulanov, Y. Gu, S. Weber, *et al.*. Evolution of laser induced electromagnetic postsolitons in multi-species plasma. *Physics of Plasmas*, 22(11):112302, 2015.

[179] D. Farina, S. V. Bulanov. Relativistic electromagnetic solitons in the electron-ion plasma. *Physical Review Letters*, 86(23):5289–5292, 2001.

[180] D. Farina, M. Lontano, S. Bulanov. Relativistic solitons in magnetized plasmas. *Physical Review E - Statistical Physics, Plasmas, Fluids, and Related Interdisciplinary Topics*, 62(3 B):4146–4151, 2000.

[181] T. Z. Esirkepov, F. F. Kamenets, S. V. Bulanov, N. M. Naumova. Low-frequency relativistic electromagnetic solitons in collisionless plasmas. *Journal of Experimental and Theoretical Physics Letters*, 68(1):36–41, 1998.

[182] T. Kurki-Suonio, P. J. Morrison, T. Tajima. Self-focusing of an optical beam in a plasma. *Physical Review A*, 40(6):3230–3239, 1989.

[183] J. I. Gersten, N. Tzoar. Propagation of localized electromagnetic pulses in plasmas. *Physical Review Letters*, 35(14):934–937, 1975.

[184] N. L. Tsintsadze, D. D. Tskhakaya. On the theory of electrosound waves in a plasma. *Sov. Phys. - JETP (Engl. Transl.);(United States)*, 487(February 1977):252–255, 1978.

[185] P. K. Kaw, A. Sen, T. Katsouleas. Nonlinear 1D laser pulse solitons in a plasma. *Physical Review Letters*, 68(21):3172–3175, 1992.

[186] T. Esirkepov, K. Nishihara, S. V. Bulanov, F. Pegoraro. Three-Dimensional Relativistic Electromagnetic Subcycle Solitons. *Physical Review Letters*, 89(27):275002, 2002.

[187] G. Sánchez-Arriaga, E. Lefebvre. Two-dimensional s-polarized solitary waves in relativistic plasmas. I. the fluid plasma model. *Physical Review E - Statistical, Nonlinear, and Soft Matter Physics*, 84(3), 2011.

[188] G. Sánchez-Arriaga, E. Lefebvre. Two-dimensional s-polarized solitary waves in plasmas. II. Stability, collisions, electromagnetic bursts, and post-soliton evolution. *Physical Review E - Statistical, Nonlinear, and Soft Matter Physics*, 84(3), 2011.

[189] G. Sánchez-Arriaga, E. Siminos, V. Saxena, I. Kourakis. Relativistic breather-type solitary waves with linear polarization in cold plasmas. *Physical Review E - Statistical, Nonlinear, and Soft Matter Physics*, 91(3), 2015.

[190] Y. Sentoku, T. Z. Esirkepov, K. Mima, K. Nishihara, F. Califano, F. Pegoraro, *et al.*. Bursts of Superreflected Laser Light from Inhomogeneous Plasmas due to the Generation of Relativistic Solitary Waves. *Physical Review Letters*, 83(17):3434–3437, 1999.

[191] L. Romagnani, A. Bigongiari, S. Kar, S. V. Bulanov, C. A. Cecchetti, T. Z. Esirkepov, *et al.*. Observation of magnetized soliton remnants in the wake

of intense laser pulse propagation through plasmas. *Physical Review Letters*, 105(17):1–4, 2010.

[192] S. V. Bulanov, T. Z. Esirkepov, N. M. Naumova, F. Pegoraro, V. A. Vshivkov. Solitonlike Electromagnetic Waves behind a Superintense Laser Pulse in a Plasma. *Physical Review Letters*, 82(17):3440–3443, 1999.

[193] C. V. Bulanov, T. Z. Esirkepov, F. F. Kamenets, N. M. Naumova. Electromagnetic Soliton Formation During Interaction Of Relativistically Strong Laser-Pulses With Plasmas. *Plasma Physics Reports*, 21(7):550–561, 1995.

[194] Y. T. Lee, R. M. More. An electron conductivity model for dense plasmas. *Phys. Fluids*, 27(5):1273–1286, 1984.

[195] A. P. L. Robinson, D. J. Strozzi, J. R. Davies, L. Gremillet, J. J. Honrubia, T. Johzaki, *et al.*. Theory of fast electron transport for fast ignition. *Nuclear Fusion*, 54:054003, 2014.

[196] E. S. Weibel. Spontaneously growing transverse waves in a plasma due to an anisotropic velocity distribution. *Physical Review Letters*, 2(3):83–84, 1959.

[197] B. D. Fried. Mechanism for Instability of Transverse Plasma Waves. *Physics of Fluids*, 2(3):337, 1959.

[198] K. Molvig. Filamnetation instability of a relativistic electron beam. *Physical Review Letters*, 35(22):1504–1507, 1975.

[199] J. F. Benage. Review of electrical resistivity measurements of dense aluminum and comparison to theory. *Physics of Plasmas*, 7(2000):2040, 2000.